DEPARTMENT OF TRANSPORTATION

# Continuous Moisture Measurement during Pavement Foundation Construction

**Soheil Nazarian, Principal Investigator**
Center for Transportation Infrastructure Systems
The University of Texas at El Paso

**OCTOBER 2023**

Final Report NRRA202307

NRRA National Road Research Alliance

To request this document in an alternative format, such as braille or large print, call 651-366-4718 or 1-800-657-3774 (Greater Minnesota) or email your request to ADArequest.dot@state.mn.us. Please request at least one week in advance.

## Technical Report Documentation Page

| 1. Report No. | 2. | 3. Recipients Accession No. |
|---|---|---|
| NRRA202307 | | |

| 4. Title and Subtitle | 5. Report Date |
|---|---|
| Continuous Moisture Measurement during Pavement Foundation Construction | September 2023 |
| | 6. |

| 7. Author(s) | 8. Performing Organization Report No. |
|---|---|
| Mark Baker, Isaac E. Zuniga, Sebastian Morales, Soheil Nazarian | |

| 9. Performing Organization Name and Address | 10. Project/Task/Work Unit No. |
|---|---|
| The University of Texas at El Paso<br>Center for Transportation Infrastructure Systems<br>Engineering Building M-105, 500 W University<br>El Paso, Texas 79968 | 11. Contract (C) or Grant (G) No.<br>(c) 1045186 |

| 12. Sponsoring Organization Name and Address | 13. Type of Report and Period Covered |
|---|---|
| Minnesota Department of Transportation<br>Office of Research & Innovation<br>395 John Ireland Boulevard, MS 330<br>St. Paul, Minnesota 55155-1899 | Final Report, Feb 21 – Aug 23 |
| | 14. Sponsoring Agency Code |

15. Supplementary Notes

http://mdl.mndot.gov/

16. Abstract (Limit: 250 words)

The variations in electromagnetic and electric properties with the moisture content of several geomaterials were assessed in this report to demonstrate their viability in estimating the moisture content of compacted geomaterials. A prototype device was also designed and fabricated to estimate the moisture content of compacted geomaterials by measuring the complex resistivity (amplitude and phase shift between the voltage and current) of geomaterials over numerous frequencies. Two fine-grained soils, two sandy soils, and two coarse-grained geomaterials were selected as a baseline for laboratory measurements. These soils were compacted and tested to measure their dielectric constants, traditional resistivities, and their complex resistivities using the developed prototype. The dielectric constants were less sensitive and more uncertain to the moisture content variations than the resistivity values. The traditional and complex resistivity measurements showed promise in the laboratory. The same soils' seismic moduli, unconfined compressive strengths, and lightweight deflectometer moduli were also established. For field implementation, a rolling four-electrode equatorial array was created and tested within the laboratory and MnROAD facility. Field polarization and deviation from expected voltages and currents occurred frequently. These results suggested that resistivity or complex-resistivity measurements with rolling four-electrode arrays may need significant improvement for controlling moisture content.

| 17. Document Analysis/Descriptors | 18. Availability Statement |
|---|---|
| Moisture content, Electrical resistivity, Density, Modulus, Foundations, Construction, Dielectric properties, Measurement, Compressive strength | No restrictions. Document available from: National Technical Information Services, Alexandria, Virginia 22312 |

| 19. Security Class (this report) | 20. Security Class (this page) | 21. No. of Pages | 22. Price |
|---|---|---|---|
| Unclassified | Unclassified | 105 | |

# Continuous Moisture Measurement during Pavement Foundation Construction

# FINAL REPORT

*Prepared by:*

Mark Baker[1], DSc.
Isaac E. Zuniga[2], MS
Sebastian Morales[2]
Soheil Nazarian[2], Ph.D., PE

[1]Private Consultant
[2]The University of Texas at El Paso

# October 2023

*Published by:*

Minnesota Department of Transportation
Office of Research & Innovation
395 John Ireland Boulevard, MS 330
St. Paul, Minnesota 55155-1899

# Acknowledgments

The authors would like to thank the National Road Research Alliance (NRRA) for funding this project. Appreciations are extended to the NRRA Technical Advisory Panel (TAP) for the technical feedback it provided. TAP members include Terry Beaudry, Raul Velasquez, Eddie Johnson, John Siekmeier, and Eyoab Zegeye Teshale from MnDOT, Todd Mansell from Caterpillar, and Deepak Maskey from Caltrans. A word of gratitude is also conveyed to Jobe Materials, GCC Materials, and the MnROAD facility staff for providing the necessary geomaterials and field assistance.

# Table of Contents

# List of Figures

# List of Tables

# List of Abbreviations

B-F – Back to Front

CL – Low Plasticity Clay

CR – Complex Resistivity

DC – Dielectric Constant

F-B – Front to Back

GW – Well-Graded Gravel

Hz – Hertz

ICMV – Intelligent Compaction Measurement Value

kohm-cm – kilo-ohm x centimeter

LWD – Lightweight Deflectometer

MDD – Maximum Dry Density

OMC – Optimum Moisture Content

R – Resistivity

RAP – Recycled Asphalt Pavement

RCA – Recycled Concrete Aggregate

REA – Rolling Equatorial Array

SM – Seismic Modulus

SM – Silty Sand

SP – Poorly Graded Sand

TR – Traditional Resistivity

UCS – Unconfined Compressive Strength

WA – Wenner Array

μA – microAmps

Φ – Complex Resistivity (prototype) Phase

# Executive Summary

## Background

Accurate and timely moisture measurement of earthwork during compaction of foundation layers is crucial to proper construction and long-term durability of pavement structures. Since the traditional methods for measuring moisture are point specific, expensive, and/or time-consuming, it is desirable to explore new devices that can provide the full coverage of the spatial variation of moisture.

In a series of publications (e.g., Tatsuoka and Correia, 2018), Tatsuoka, Correia, and their colleagues showed the importance of controlling the moisture content and degree of saturation during the construction of unbound pavement layers. Failing to estimate the moisture content accurately and promptly during construction may negatively impact the proper quality control/quality assurance (QC/QA) of compacted geomaterials (Roberson and Siekmeier, 2002; Nazarian et al., 2014). Although numerous methods and techniques have been proposed to measure moisture content, none of them have been able to deliver real-time, continuous moisture measurements that would aid engineers in delivering more durable pavement structures.

Several techniques for determining the moisture content of geomaterials have been proposed throughout the years. These techniques, which can be classified based on their approaches and measuring principles, are normally divided into direct and indirect categories (Svensson, 1997). The direct method consists of extracting a soil sample from the desired location to be investigated and weighing it before and after drying in an oven at a maximum temperature of 105°C (220°F). This is the gold standard for measuring the moisture content. However, it is neither nondestructive, continuous, nor real-time. Indirect methods are based on the use of a radiation source or a probe in the soil for the measurement of moisture contents. Aside from the nuclear density gauge (NDG) that is currently used extensively, some examples of these methods (see Table 1) consist of time-domain reflectometry, ground penetrating radar (GPR), electromagnetic/dielectric measurements, soil resistivity/conductivity, etc. None of these methods measure the water content directly. They each measure a parameter that is correlated with the water content in the soil. Some of these methods only provide spot measurements and some require probe insertion and are typically nondestructive since the soil is only disturbed during installation (Evett et al., 2008).

## Summary of Tasks

The research team has documented the current state of knowledge concerning field moisture measurement during pavement foundation construction. The team has also provided critical information about the state of the art and the state of practice related to the most effective moisture measurement devices suitable for improving compaction near structures such as retaining walls and bridge abutments. Finally, a prototype device based on the concept of complex resistivity capable of continuously measuring moisture during pavement foundation construction has been developed and tested. Even though the study demonstrated the feasibility of the complex and traditional resistivity

methods in estimating in situ moisture contents, further hardware and software development is necessary to implement the concept in the day-to-day operation of highway agencies.

## Conclusions and Recommendations

The proposed technology is based on the measurement of complex resistivity (CR) of geomaterials as a function of frequency, electric current, and measurement geometry to characterize moisture content and degree of saturation. Conceptually, complex resistivity measures ionic conduction and polarization along adsorbed water at grain boundaries, ionic conduction through free pore fluid, and polarization at the air-water interface. The proposed CR at intermediate frequencies is hypothesized to yield simpler field procedures, distinguish saturated and unsaturated cases with an enhanced polarization signal with partial saturation from charges blocked from the movement at air-water interfaces, and minimize the need to measure soil and water resistivity before field deployment.

The primary conclusion from this study has been that complex-resistivity measurements with a rolling four-electrode array, with any given geometry, need significant improvement for the control of moisture content for the following four reasons:

1. The apparent sensitivity of the CR measurement to electrode pressures on different soil types is difficult to predict or compensate for.
2. An incompatible tradeoff between a large electrode contact area and short array spacing is necessary to measure shallow, less dense specimens without deforming the specimen.
3. The CR measurements become sensitive to larger heterogeneity scales with a larger electrode spacing.

As used in these experiments, the equatorial array will likely be moderately sensitive to heterogeneity. Picturing a rolling Wenner array, the four electrodes can be rolling parallel or perpendicular to the array alignment. With the parallel alignment, three electrodes would follow the leading electrode, and only the leading electrode would sample a new heterogeneity and show the least variability. The perpendicular alignment would have all four electrodes sampling heterogeneity independently and offer the most variability. The equatorial array would be intermediate to these two cases. Although electrode spacing is considered to be a controlling factor for the depth of investigation of heterogeneous layers, it also appears necessary to consider the scaling law between electrode spacing and the size of heterogeneity for subsequent work. The advantages of noncontact electromagnetic measurements (EM) can be summarized in the following manner:

1. Noncontact EM offers a preferred avenue for making moving resistivity measurements.
2. It is easier to couple energy and make measurements in highly resistive drier soils or engineered materials, such as used in recycled asphalt materials, non-hydrophilic materials like carbonates, and large aggregate hydrophilic materials.
3. The coil area can control the volume averaged, while the spacing between sending and receiving coils controls the depth of investigation.

# Chapter 1: Introduction

## 1.1 Objective

For successful construction and the long-term durability of pavement constructions, the moisture content of earthwork must be measured accurately and promptly during the compacting of foundation layers. The goal of this research was to develop and demonstrate a prototype/breadboard of a device that can continually measure moisture throughout the construction of a pavement foundation and evaluate existing devices that can read moisture in a laboratory and field environment.

The developed device is based on characterizing moisture content by measuring a geomaterials' complex resistivity (CR) as a function of frequency, electric field strength, and measurement geometry. In complex resistivity measurements, the distortion (phase shift) between the voltage and current is recorded in addition to the resistivity amplitude over a wide frequency range. The resistivity is given by the in-phase amplitude, while the dielectric constant is given by the amplitude with a 90° phase shift.

Complex resistivity measurements can be caused by both the extrinsic properties of charge transfer between metal electrodes to pore water and the intrinsic properties of ionic conduction in the geomaterial. Ionic conduction across free pore water, polarization at the air-water interface, and polarization along adsorbed water at grain boundaries are the targets to be measured by complex resistivity. Void content, moisture content, and pore size distribution control the in-phase and out-of-phase currents. In most cases, dissolved solids or mineral surface charges have an ionic effect that suppresses water permittivity, which causes bias in materials with a high fines content. Water connection across the pore space and saturation levels dominate low-frequency resistivity measurements, with water volume coming in second. If sufficient observations are taken to differentiate between residual moisture on particles, saturation fluctuations, and void changes in compaction, low-frequency resistivity may likely be employed with little calibration, which requires measuring:

1. Material resistivity before watering
2. The resistivity of the water added
3. Pre-and post-compaction resistivity

With an improved polarization signal with partial saturation, CR at intermediate frequencies should identify saturated and unsaturated situations from charges restricted from movement at air-water interfaces, reducing the requirement to evaluate soil resistivity before and after watering.

## 1.2 Organization

Chapter 2 will document the current state of knowledge concerning field moisture measurement during pavement foundation construction and case studies demonstrating cost savings resulting from more effective moisture measurements. Chapter 3 will provide the different laboratory procedures and an explanation of each laboratory measurement. Chapter 4 will present the different measuring devices with correlations to the moisture content in the laboratory setting on compacted specimens. Chapter 5

will provide the field evaluation including the original procedure and revised laboratory testing. Lastly, Chapter 6 will discuss the conclusion made from the study and recommendations.

# Chapter 2: Current Moisture Measurement Methods

A foundation layer for durable pavements should have the following attributes (White et al., 2021):

1. Provide uniform support
2. Be balanced in terms of flexibility and stiffness
3. Provide adequate drainage
4. Not be affected by permanent plastic deformation
5. Utilize sustainable practices and materials

Moisture content is an essential property of geomaterials that must be monitored during and after the construction of unbound pavement layers. Improper quality control and quality assurance (QC/QA) of compacted geomaterials may result in an inability to estimate the moisture content correctly and rapidly during construction. During the life of a pavement, excessive volume of water in the unbound layers of the pavement structure may contribute to the development of early distress and lead to the structural or functional collapse of the pavement. Water-related damage can result in one or more of the following types of deterioration:

- weakening of the subgrade, base, and subbase;
- differential swelling in expansive subgrade soils; frost heave;
- weakening of the subgrade, base, and subbase during frost melt; and
- movement of fine particles into the base or subbase coarse materials, resulting in a decrease in hydraulic conductivity (Liang et al., 2016).

During the 1980s, several scholars researched the problem of monitoring the water content of pavement constructions, which sparked an upsurge in interest in this field. Svensson (1997), as part of the Strategic Highway Research Program (SHRP), examined how fluctuations in moisture content affected pavement structures. Since then, several methods and procedures for measuring the soil moisture content have been presented. Traditional moisture measurement methods, such as physical sampling or installing sensors such as time domain reflectometry (TDR) probes, give only spot measurements, making them impracticable for large-scale implementation.

An ideal section of pavement should be laid on a consistent pavement base that extends beyond the driving lane. To achieve consistent pavement construction, it should be constructed upon a uniform embankment. The cross-section of an idealized pavement is seen in Figure 1. It must offer appropriate drainage and be sufficiently compact to withstand various vehicular loads. The subgrade should be properly compacted first. A review of the literature on the various measuring apparatuses is provided next.

## 2.1 Measuring Methods

Several methods for soil moisture measurement have been developed throughout the years. Based on the technique and measurement principles used, the various methodologies may be divided into direct and indirect categories (Svensson, 1997). The direct approach (i.e., the gravimetric method) entails collecting a soil sample from the site under investigation. The soil sample is weighed before and after drying at 105°C (220°F). This approach is regarded as the "gold standard" for determining the moisture content of substances.

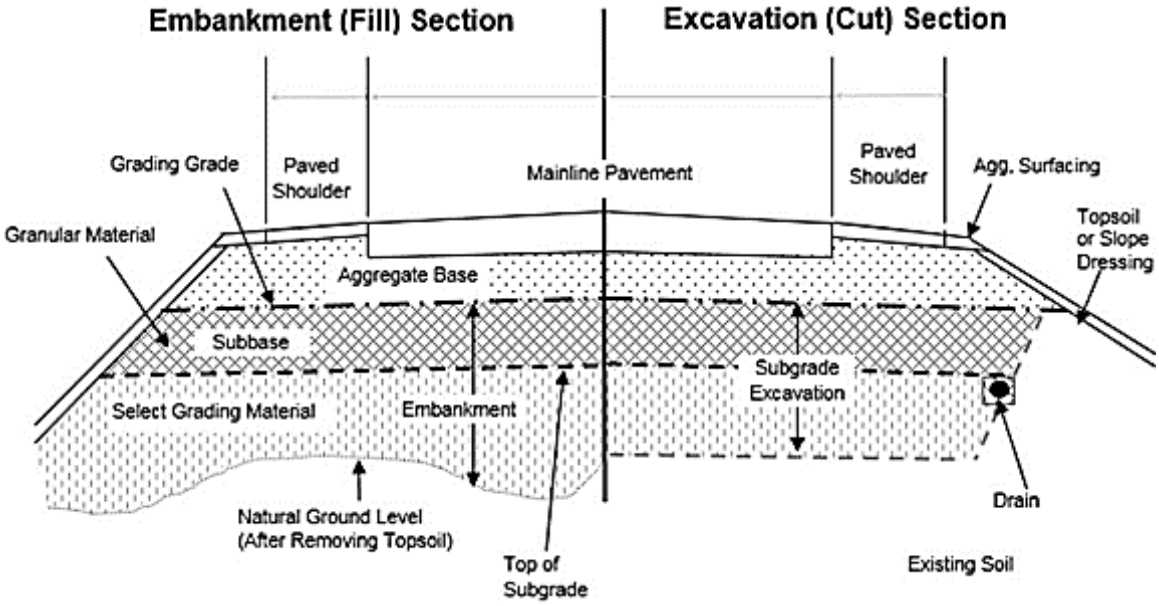


**Figure 1: An Ideal Pavement Section (from http://www.dot.state.mn.us/materials/pvmtdesign/manual.html)**

In indirect approaches, a radiation source or a probe put in or on the geomaterial is used to measure a parameter significantly related to the moisture content. Since the soil is only disturbed during installation, the primary benefits of these techniques are that they are more rapid and often nondestructive (Evett et al., 2008).

None of these techniques directly measures the soil water content, but all measure a characteristic highly linked with the soil moisture content. Some of the techniques that monitor moisture content only offer point readings, not spatially continuous observations. Examples of these approaches and their principles are presented in Table 1.

ASTM D6938-17a outlines the standard test techniques for in-situ density and soil water content measurement with nuclear methods. The nuclear density gauge (NDG, Figure 2) measures the density and estimates the water content of compacted geomaterials in various ways (Viyanant et al., 2004). The gauge is calibrated to measure soil or aggregate moisture mass per unit volume. The volumetric water content may be calculated by dividing the volume of water by the total volume. The nuclear gauge also employs direct transmission and backscatter to determine density and water content. Thermalizing or slowing fast neutrons that impact hydrogen atoms in the soil, the neutron moisture measurement

calculates the water mass per volume. The neutron source and thermal neutron detector are surface-based and can record and convert the slow neutron count rate to estimate the volumetric water content. Thermal neutron capture may also affect the thermal neutron count rate, with iron (Fe) being the most prevalent modifier. Alternative methods are suggested for measuring the moisture content of the base and subgrade (Sebesta et al., 2013).

**Table 1: Indirect Moisture Content Tests**

| Method | Measurement Principle | Explanation |
|---|---|---|
| Nuclear Density Gauge (NDG) | Back-scattered or transmitted gamma-ray count-rate | A source of high energy emits gamma rays (Co60) that interact with the geomaterial. A gamma detector counts the returning gamma rays with energies linked to Compton Scattering, which is directly connected to electron density and material density. |
| Nuclear Moisture Gauge | Thermalized neutron count-rate | A neutron source emits high-energy neutrons, while a neutron detector measures neutrons whose energy has been thermalized by repeated collisions with hydrogen nuclei in water. Neutron capture by some elements affects count rates subsequently. |
| Nuclear Magnetic Resonance (NMR) | Detection of the weak magnetic moment | After placing a combination of soil and water in the NMR analyzer and inducing a radio frequency, a voltage is supplied to the surrounding coil. This voltage is proportional to the amount of water in the sample and corresponds to the number of atoms that have absorbed energy (Svensson, 1997). When a radio frequency is induced, an atom absorbs a certain amount of energy to reposition itself inside the magnetic field. |
| Capacitance meters | Oscillating circuit to measure changes in frequency | A capacitor consists of two insulated electrodes, with the soil contributing the most to the dielectric constant. Equipment and soil compose the measurement circuit. The probe detects and measures the frequency change dominated by the water content of the soil. (Svensson, 1997). |
| Ground Penetrating Radar (GPR) | Short pulses of electromagnetic through the soil | In addition to its other applications, GPR may be used to assess the soil's water content. Changes in permittivity may also be connected to variations in transmission time and amplitude of the reflected pulse (dielectric constant). After getting the changes in permittivity, it is possible to compute the soil's water content (Svensson, 1997). |
| Thermal Sensors | Heat conductivity or heat capacity of the soil | A heat pulse is generated, and the subsequent increase or decrease in soil temperature is monitored over time. Since soil is a weak heat conductor compared to water, the heat or heat transfer quantity is proportional to the volumetric water content (Evett et al., 2008). |

**Table 2 (cont.): Indirect Moisture Content Tests**

| Method | Measurement Principle | Explanation |
|---|---|---|
| Conductivity Sensors | Electrical conductivity of a porous medium in contact with the soil | Granular matrix sensors and gypsum blocks include conductivity sensors. Instead of assessing water content by volume, these sensors evaluate soil water tension (Evett et al., 2008). Current measures the conductivity and quantity of water between electrodes by injecting an alternating voltage between two electrodes in a porous medium, facilitating the exchange of soil moisture. |
| | Voltage measured at two electrodes from current injected at two other electrodes | A low-frequency alternating current is injected between two electrodes, while a voltage is monitored between two electrodes with no current flow. The shape of the electrodes transforms the observed voltage/current ratio to apparent resistivity, while the distance between the electrodes regulates the measurement volume. |
| | Eddy currents, induced by an alternating magnetic field, increase with conductivity | A magnetic field created by one coil over the ground is measured at a second coil. This secondary field reacts to geometry, magnetic susceptibility of the soil, and eddy currents created in a conductive soil, which are principally governed by soil moisture. The eddy current is related to the frequency and conductivity of the soil. |
| Resistance measurements | The resistance between two electrodes | The electrical resistance of the soil, which fluctuates depending on its moisture content, is used to quantify its moisture content. As the moisture content of the soil rises, its electrical resistance lowers, and conductance rises. Resistance may range from several kΩ when wet to several MΩ when dry (Sad, 2007). |
| Tensiometer measurements | Measurement of a pressure differential in the soil | A porous membrane forms the contact between the water-filled pressure sensor and the soil as the significant component of the tensiometer. The negative pressure inside the tube may be measured using a vacuum gauge to determine water tension (Evett, 2008). However, if the relationship between matric potential and soil water content is understood, the water content may be determined (Svensson, 1997). |

Time Domain Reflectometry (TDR, Figure 3) is widely used to determine water content and electrical conductivity (Jones et al., 2002). TDR transmits an electromagnetic pulse over a coaxial wire to the probe and detects its reflection. Time to reflection is proportional to cable length, early reflection amplitude is governed by permittivity (dielectric constant), and late reflection features are governed by

electrical conductivity. The reflection amplitude is determined chiefly by the dielectric constant of the soil around the probe; the dielectric constant is 1 for air, 2-9 for ordinary dry soil particles, and about 81 for water. Since changes in the TDR-measured dielectric constant are strongly related to changes in the water content of soils, it is relatively easy to determine the soil moisture content for silicate soils (Yu and Yu, 2009). Soils with carbonates, gypsum, and clays have a higher dry permittivity and require local calibration for mineral variations.

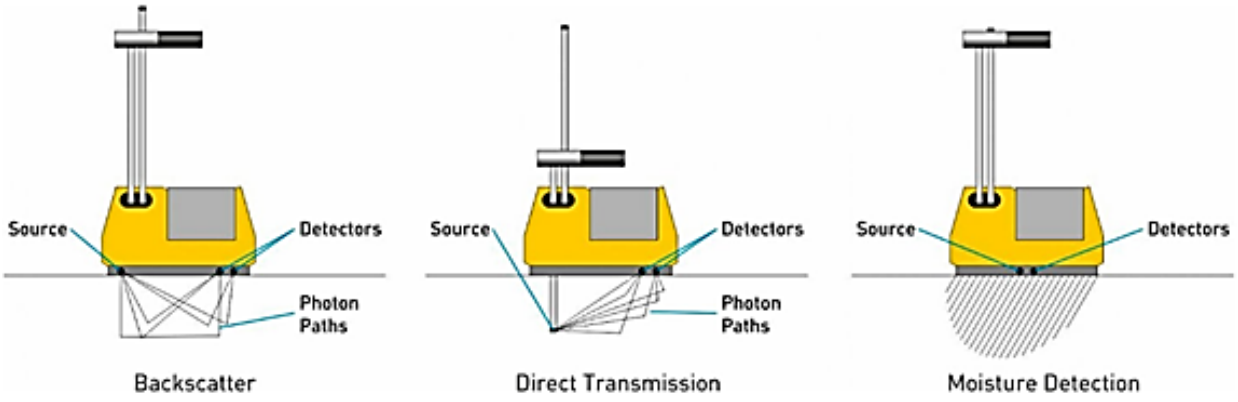


**Figure 2: Positioning of a Nuclear Gauge for Three Different Methods (UTEST, 2016)**

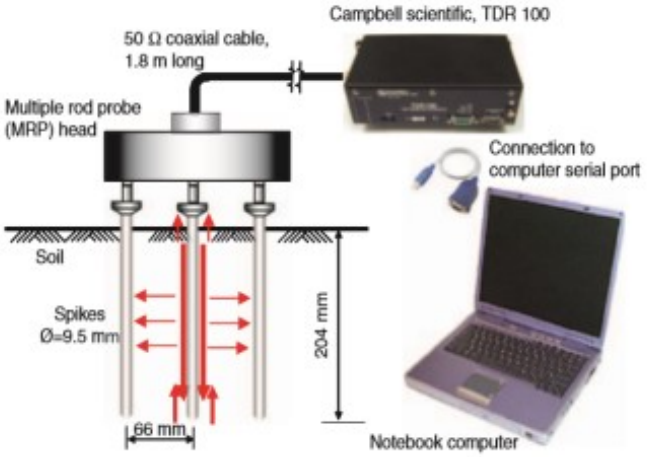


**Figure 3: Typical TDR System (Yu and Yu, 2009)**

Sotelo (2012) evaluated five non-nuclear devices, including a Purdue Time Domain Reflectometer (TDR), Soil Density Gauge (SDG200), Decagon 10HS Moisture Content Sensor (10 HS), Speedy Moisture Tester (SMT), and a DOT600 Roadbed Water Content Meter, to determine their accuracy in measuring moisture content and dry density. Sotelo prepared several small-scale specimens within the laboratory to simulate the construction of five soils ranging from poorly graded gravel to clay (CH). The TDR and SMT were the most accurate devices in measuring moisture content. The other three devices were accurate, with only specific soil samples. The most accurate device in measuring dry density was the TDR, except for a CH material; however, the SDG accurately measured the density of the CH soil but not the remaining soils.

## 2.2 Evaluation of Technologies Determining Moisture Content over Time

Bogena et al. (2007) examined an $ECH_2O$ probe (model EC-5, low-capacitance sensor by Decagon Devices Inc.) utilizing laboratory and field tests. Using TDR and EC-5 sensors, they also compared permittivity and soil water content data. They put four EC-5 sensors and two TDR probes permanently attached to a data recorder in the field. The TDR measurements were conducted using Campbell Scientific TDR100 cable tester equipment, and a sensor reading-permittivity (SRP) model was utilized to determine the EC-5 sensor's recorded permittivity. Using an equation given by Robinson et al., the researchers calculated the soil moisture content (2003). Figure 4 shows the TDR-measured soil water content and the mean values and standard deviations of all EC-5 sensors throughout seven months. The findings indicated that the data from the EC-5 sensor should be modified using the temperature and conductivity adjustment algorithms.

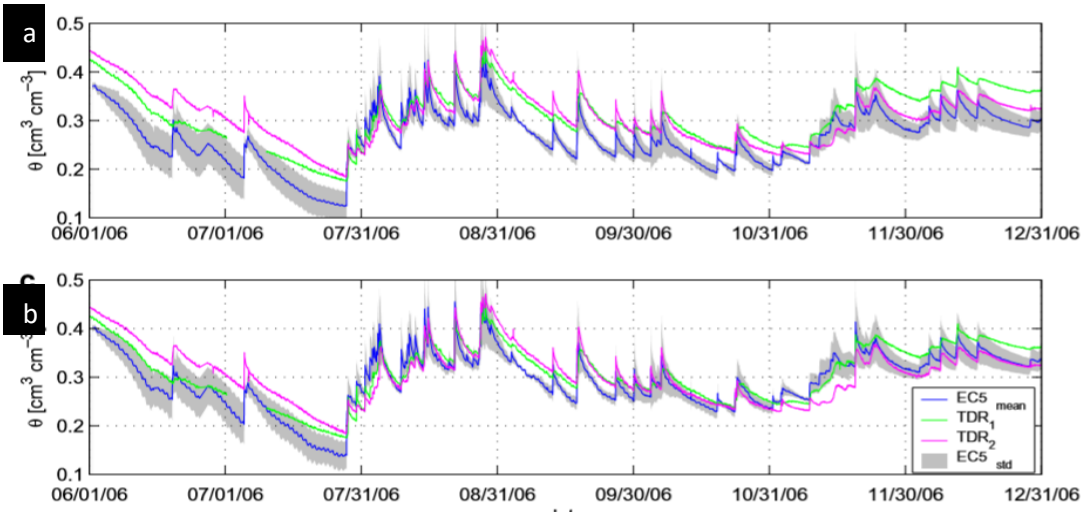


**Figure 4: Measured VWC (a) TDR and EC-5 Sensors (b) TDR and Corrected EC-5 Measurements (Bogena et al., 2007)**

Mittelbach et al. (2011) examined a distinct capacitance probe (10HS) for measuring volumetric water content (VWC) in the laboratory and the field. The 10HS VWC readings were compared to the matching gravimetric and TDR data (TRIME-EZ and TRIME-IT, IMKO GmbH, Germany). Using gravimetric sample measurements as a reference, the goal of the laboratory tests was to detect the difference in VWC between the 10HS and the TRIME sensors. Figure 5a displays the laboratory VWC measurements. Two calibration functions are presented for the 10HS sensor (Decagon Version 2.0 and best lab fit). According to the findings, TDR values were closer to the standard VWC. The calibration feature of Decagon Version 2.0 produced inaccurate results, particularly over 30-40% moisture content. The finest lab fit enhanced the reading, hence increasing its reliability. Figure 5b depicts the measurement accuracy of sensor reading, illustrating the variation within the 10HS sensor type (blue) and the DV/dVMC of the 10HS sensor (green). The sensor sensitivity for DV/dVWC (mV/Vol.%) decreased significantly as VWC

increased. The decrease in sensitivity may be linked to the concept of capacitance sensors, wherein the capacitor charges more slowly at high VWC.

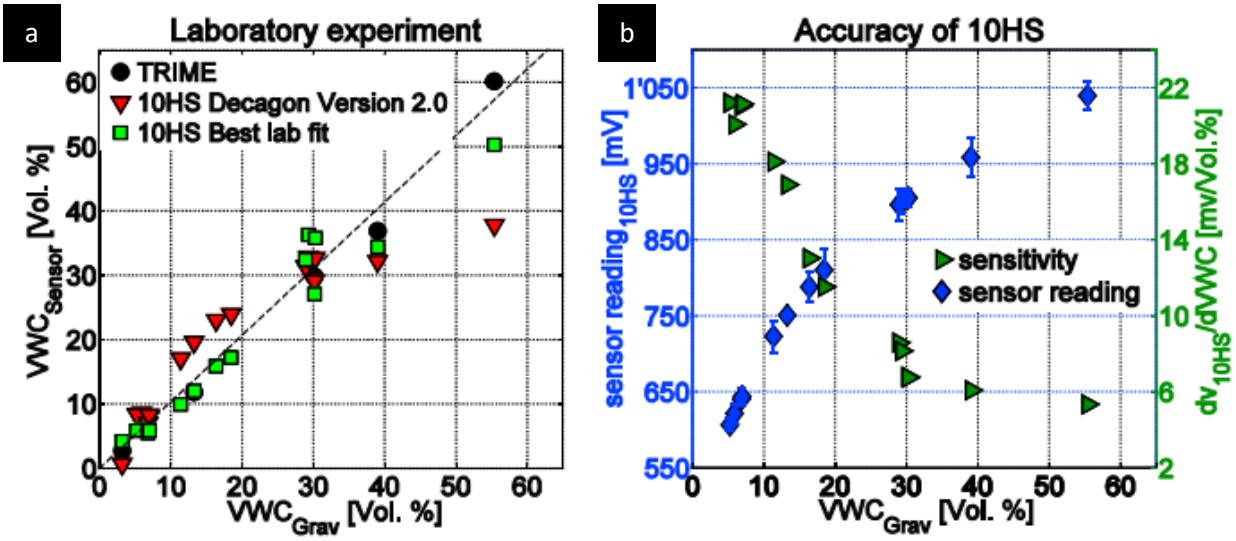


**Figure 5: (a) Laboratory Measurements Results with TRIME (TDR) and 10HS (capacitance) Sensors as a Function of VWC of the Gravimetric Samples (b) Accuracy of 10HS Sensors (Mittelbach et al., 2011)**

The 10HS sensors were evaluated for the field measurements at the Swiss locations of Oensigen (OEN) and Payerne (PAY). For 13 months, the soil moisture content was monitored at both sites using 10HS and TRIME IT/EZ. Figure 6 depicts precipitation, air temperature, and absolute soil moisture. Absolute soil moisture is the soil moisture integrated across the measured soil column in millimeters. Except for the past two months, using the best field fit considerably improved the calculated absolute soil moisture content, mirroring TDR readings. The researchers determined that the optimal configuration for accurate soil moisture networks comprised parallel capacitance and TDR measurements with the correct calibration of 10HS sensors. They concluded that the differences between the various 10HS sensors were minimal. In addition, they emphasized that the 10HS sensor requires site-specific calibration functions and is optimal for low VWC concentrations.

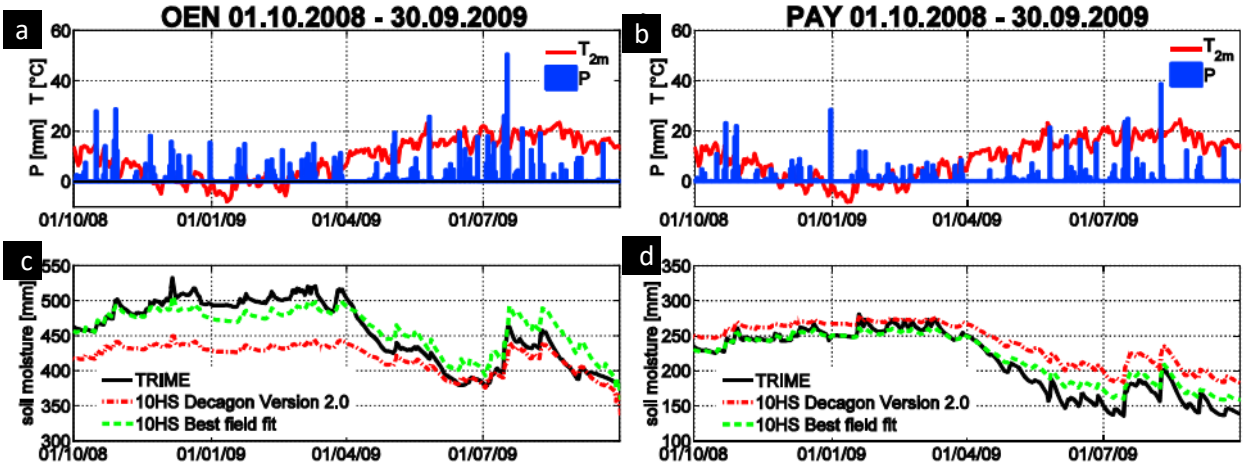


**Figure 6: Precipitation and Temperature Measurements of (a) OEN and (b) PAY. Absolute Soil Moisture of (c) OEN and (d) PAY (Mittelbach et al., 2011)**

Hansen and Nieber (2013) examined the accuracy of the DOT600 (moisture content), WP4C dew point potentiometer (matric suction), the Button Heat Pulse Sensor (BHPS) (temperature rise vs. moisture content), and an exudation pressure test device in predicting the moisture contents of three subgrade soils typically used in Minnesota roadway construction projects. They indicated significant variations in the performance and accuracy of each instrument. The DOT600 showed a strong correlation between output period and volumetric water content while overestimating moisture content compared to traditional methods. The WP4C was not effective for the tested soil types at suctions below 250 kPa. The BHPS displayed a promising correlation between temperature rise and moisture content but depends on soil calibration. The exudation pressure device's relationship with optimum moisture content was inconclusive.

In a study, Singh (2017) evaluated the field performance of eight electromagnetic (EM) sensors (TDR315, CS655, HydraProbe2, 5ET, EC5, CS616, Field Connect, and AquaCheck). Specific aims of the research included evaluating EM sensors for VWC and comparing factory calibration to bespoke calibration procedures for VWC. In addition to the factory default calibrations for the EM sensors, the Topp calibration equation (Topp et al., 1980) was evaluated for the TDR315, HydraProbe2, and EC5 sensors. Following Bell et al., the field-calibrated neutron moisture meter (NMM) was adopted as the standard for VWC (1987).

The variance over time between sensor-reported and reference VWC found in this investigation is shown in Figure 7 for single-sensor probes and Figure 8 for multi-sensor probes. Using either the factory calibrations or the included alternative calibrations, these charts indicated that all tested sensors followed the overall trend. However, they all overestimated VWC in comparison to the standard. Using Topp's calibration equation instead of the factory calibration enhanced the performance of TDR315 but not HydraProbe2 or EC5.

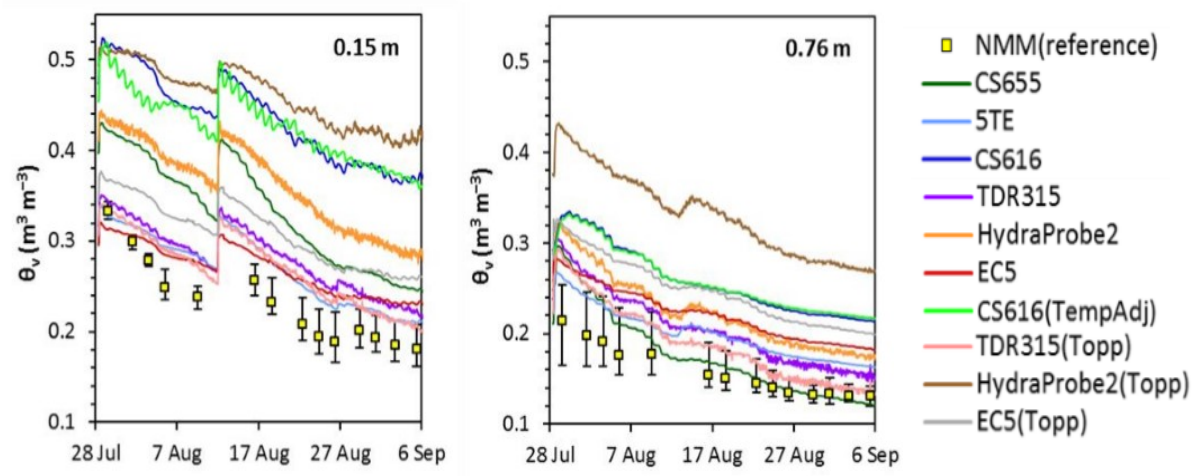


**Figure 7: Measurements of VWC at Two Distinct Depths with Single-Sensor Probes as compared with the field-calibrated NMM (Singh, 2017)**

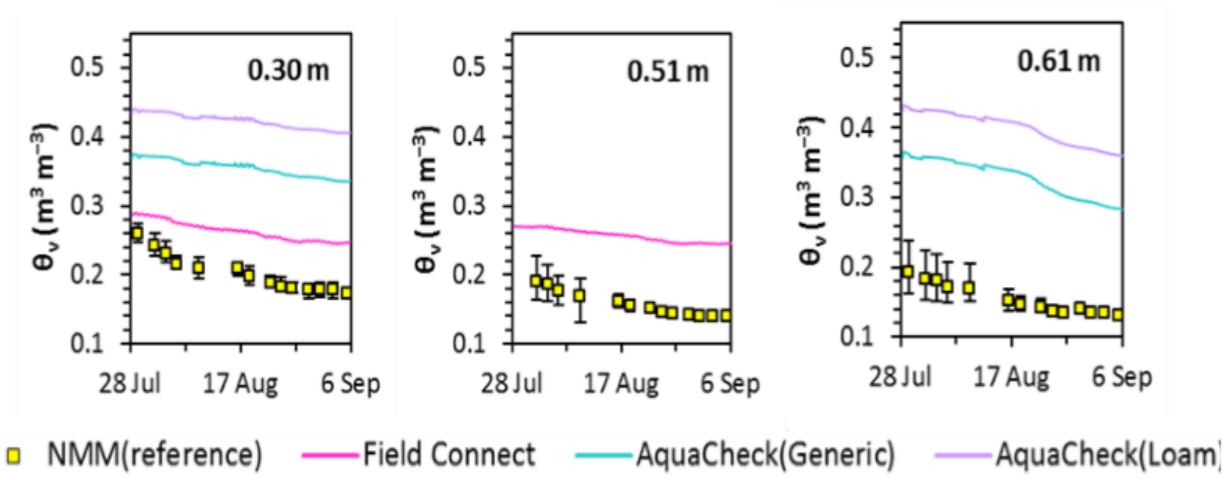


**Figure 8: Measurements of VWC at Three Distinct Depths using Multi-Sensor Probes as compared with Field-Calibrated NMM (Singh, 2017)**

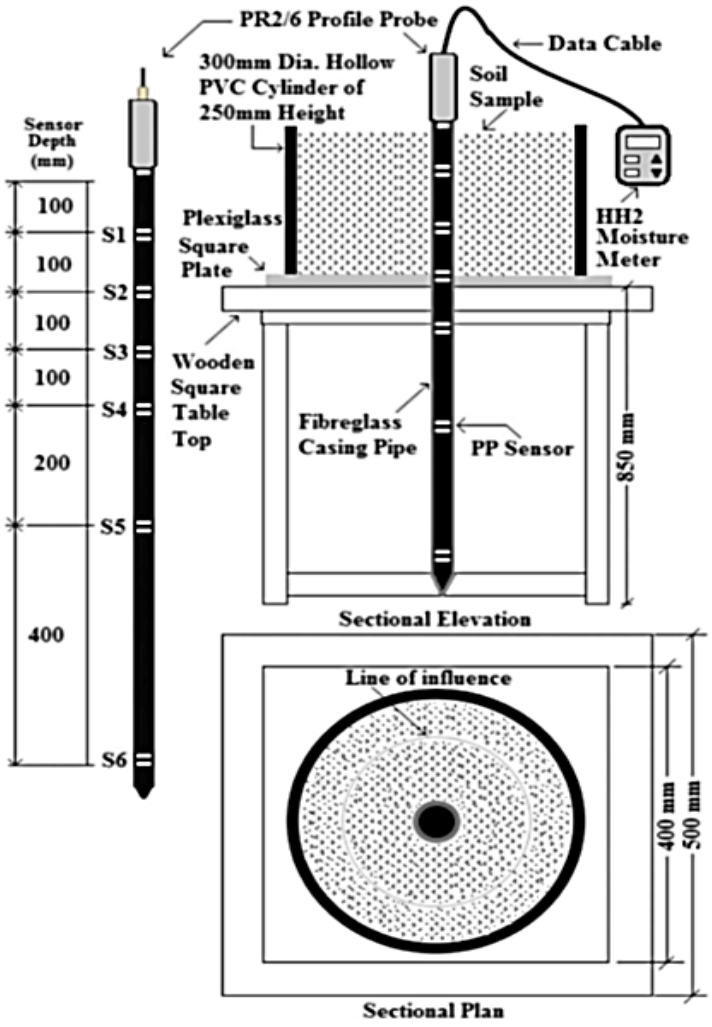


**Figure 9: Laboratory Setup for Calibration of PP Sensors (Shaikh et al., 2018)**

Shaikh et al. (2018) devised a simple laboratory setup to analyze all six profile probe (PP) sensors for a specific soil type and compaction condition concurrently. Based on TDR and the capacitance technique, PP measurements were conducted on six soils planned for use in a multilayer cover system (MLCS). Figure 9 depicts the experimental setup used to evaluate the performance of the PP. This assessment was accomplished by comparing the measured and calculated (theoretical) VWC; recalibration was undertaken if the comparison was inadequate. The first findings revealed a discrepancy between the measured and calculated VWC for each of the six soil types.

Consequently, various calibration constants were utilized to recalculate the recorded VWC from the known voltage values and the square root of the dielectric constant; the recalculated measurements yielded satisfactory findings, as shown in Figure 10.

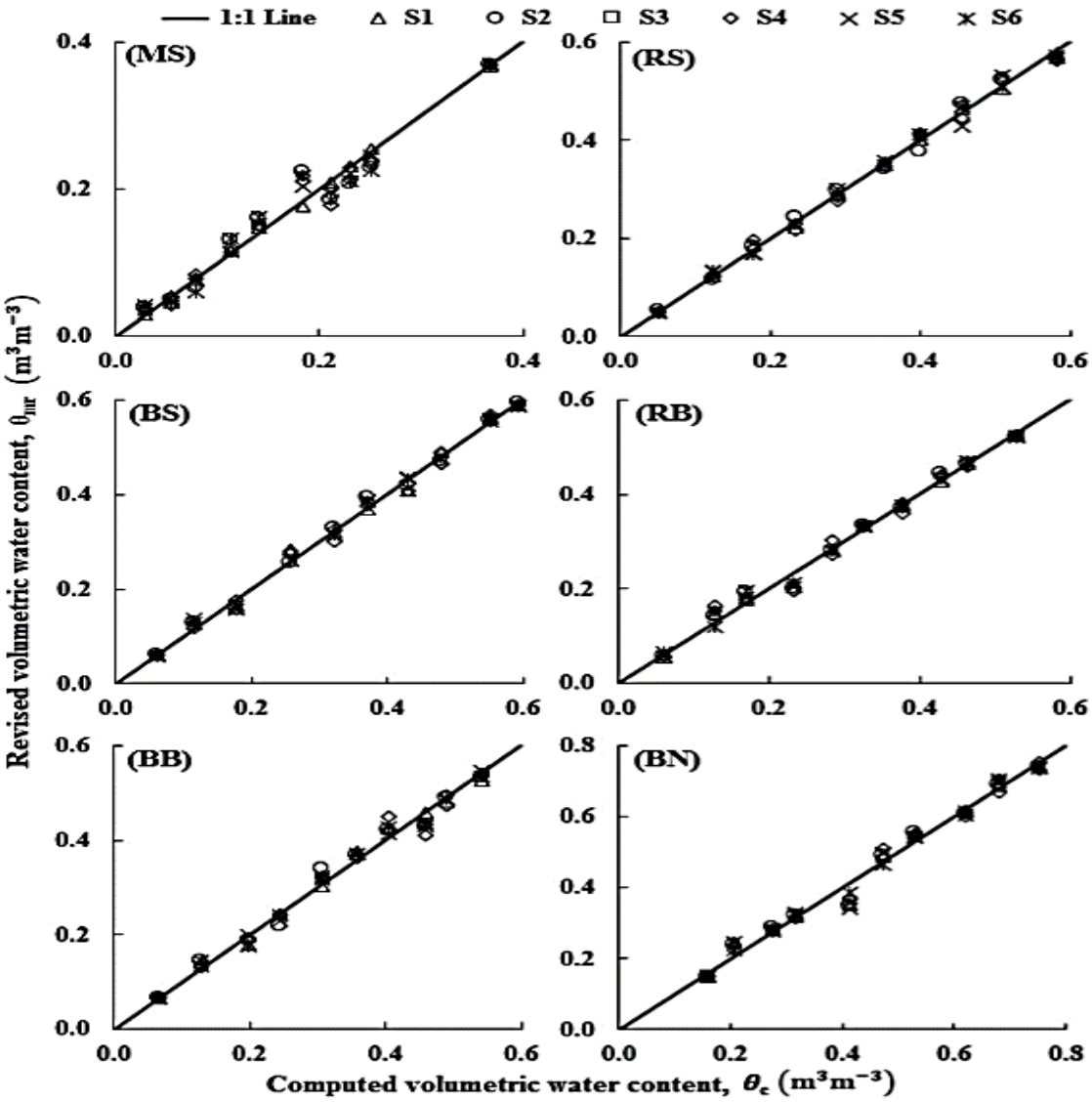


**Figure 10: Comparison between Measured (using PP) and Computed VWC (Shaikh et al., 2018)**

Figure 11 provides a more straightforward illustration of comparing sensor data before and after calibration for two soils, RS (medium plastic red soil) and RB, with the same compaction condition (mixed soil with bentonite). Without calibration functions, various sensors provided different VWCs for the same VWC at a particular compaction stage; however, after completing sensor- and soil-specific calibrations, the calculated and measured VWCs matched well, and all sensors reported comparable results. Before deploying the PP for field monitoring programs, they urged using their suggested laboratory process for accurate VWC (from 6% to 1% using calibration functions). They determined that soil water content may be continually monitored using a GPR system with many channels.

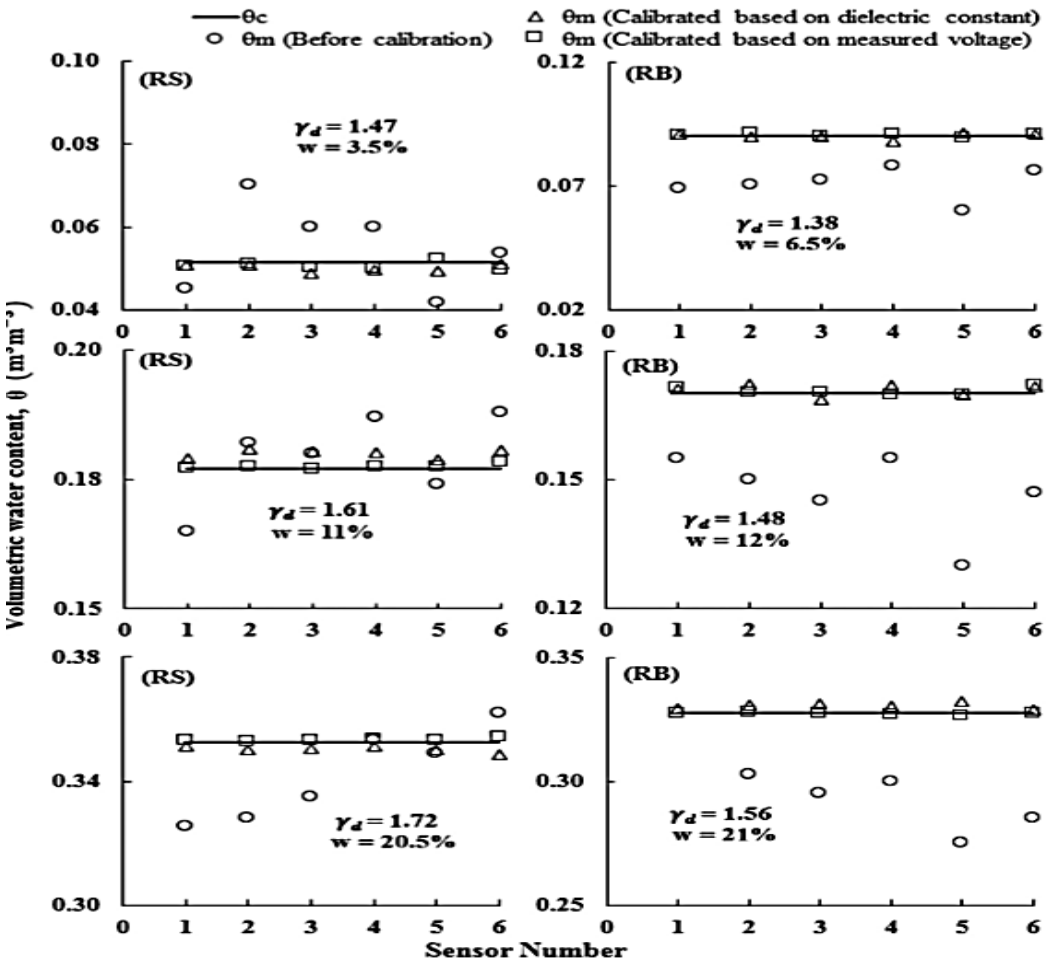


**Figure 11: PP Measurements Before and After Calibration at Three Various Compaction States in RS and RB (Shaikh et al., 2018)**

## 2.3 Using GPR for Continuous Moisture Content Measurements Over Large Distances

The GPR operates by emitting brief pulses of electromagnetic energy from an antenna into the road structure, which is then reflected to a receiving antenna (Figure 12). The transmission duration and amplitude of the reflected pulse may be correlated with the position and dielectric discontinuities of the material (Maser and Scullion, 1992; Svensson, 1997). Because of their direct link, the moisture content may also be determined by monitoring the changes in permittivity (dielectric constant). Typically, the equipment is installed on a van for highway studies so that data collection may be conducted at speeds similar to traffic flow (Figure 13). Air-coupled or ground-coupled operations are suited for GPR antennas. The antennas are positioned around 250 mm above the surface for air-coupled mode operating at highway speeds. For a stronger signal, ground-coupled antennas lie on the ground's surface.

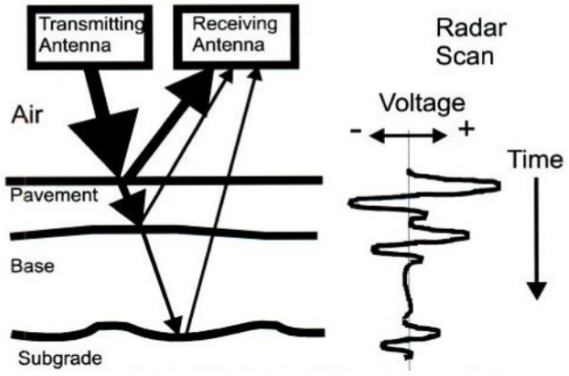


**Figure 12: Transmission and Reflections from Interfaces in a Pavement Section (Morey et al., 1998)**

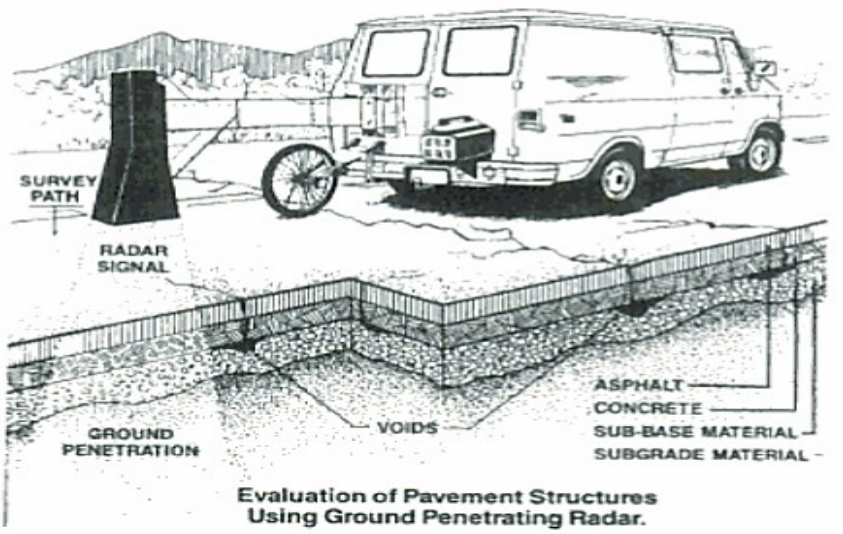


**Figure 13: Illustrated Example of Van-mounted GPR System (Morey et al., 1998)**

For many decades, the application of GPR for continuous measurements of soil moisture content on the various strata of a pavement system has been researched. Using a van-mounted horn antenna setup, Maser and Scullion (1992) could effectively derive a moisture profile from radar data. Emilsson et al. (2002) showed that multichannel GPR may be used to measure moisture content in roadbeds continually. As seen in Figure 14a, their study was based on a standard midway technique using an antenna configuration. The antenna spacing in the array ranged from 0.15 m to 4 m for three separate antenna arrays operating at 250, 500, and 800 MHz. The findings in this paper were derived from 500 MHz data. Figure 14b shows an image of the 500 MHz antenna array. They gathered data at speeds between 20 and 40 kilometers per hour and determined the volumetric soil water content at the location. Figure 15 shows the outcomes.

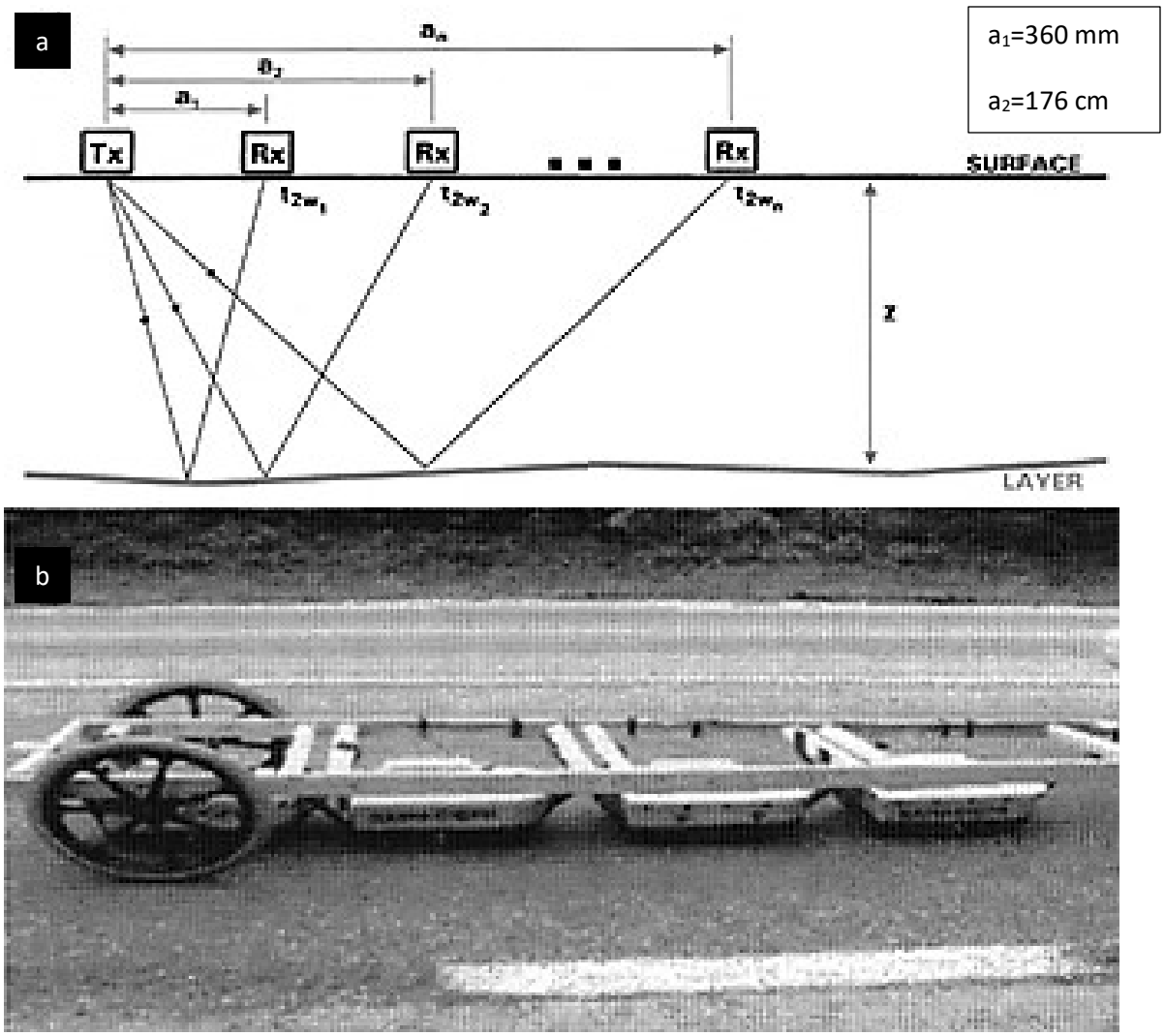


**Figure 14: (a) Antenna Setup for Velocity Determination, (b) 500MHz Antenna Array (Emilsson et al., 2002)**

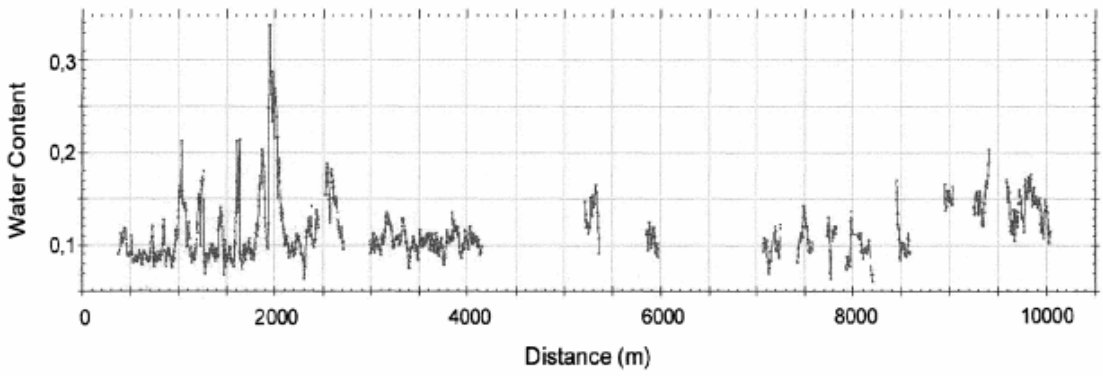


**Figure 15: Calculated Soil Moisture Content (Emilsson et al., 2002)**

Gerhards et al. (2008) proposed a novel method using a multichannel GPR that enabled simultaneous assessment of the depth of a reflector and the average volumetric water content above the reflector

with significantly increased operating effort compared to conventional measurement. They used a Mal GeoScience, Sweden-manufactured GPR multichannel device MC4 with a 250-MHz antenna setup. For a straightforward assessment, they employed two trip durations (t2 and t3) from differing antenna separations using a common midpoint (CMP) reflector (Figure 16).

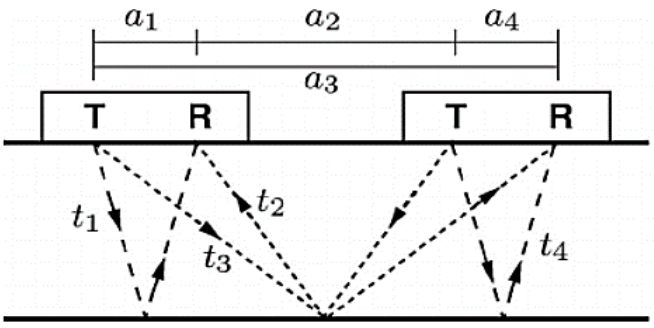


**Figure 16: Antenna Setup for Multichannel Measurement (Gerhards et al., 2008)**

Because four rays and three antenna separations are available for each measurement site, the two-point assessment uses only some available information. To determine the reflector depth and average water content, a multipoint assessment with varying numbers of channels was conducted (Figure 17). The gray dashed line represents the multipoint assessment of Channels 1 and 2, whereas the black dashed line represents the multipoint evaluation of all channels. They found that the use of GPR exhibited in their work allowed for the simultaneous measurement of reflector depth and average water content and had a high potential for characterizing subsurface structure.

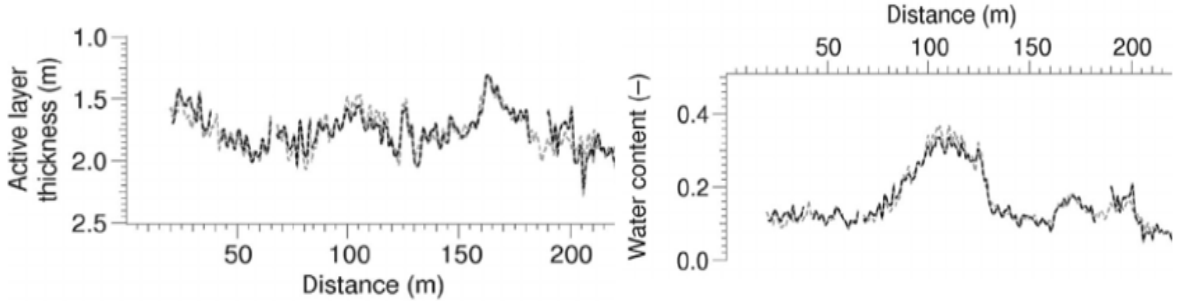


**Figure 17: Calculated Reflector Depth and Average Water Content using Different Channels (Gerhards et al., 2008)**

Wollschlager et al. (2010) used multichannel GPR at a permafrost location to deduce spatial differences in thaw depth and average volumetric water content of the active layer. Their measurements were conducted per a modified version of the method used by Gerhards et al. (2008). Their multichannel GPR system allowed them to collect data from nine “channels” of transmitter-receiver combinations. Using the CMP technique while moving along the radargram, they could accurately estimate relative dielectric permittivity, reflector depth, and average soil moisture content at each position. In addition, they created an inverse evaluation process to improve precision.

The research (Wollschlager et al., 2010) indicated that the multichannel GPR approach covers the scales between standard point measurements and space-based remote sensing. Measurements were undertaken on an area of roughly 85 m by 60 m with surface and soil textural qualities ranging from medium- to coarse- to fine-textured soils, as well as the bed of a gravel road. Figure 18 depicts the topographically corrected reflected depth, relative dielectric permittivity, and average volumetric soil moisture content of the unfrozen active layer obtained from the multichannel analysis. Figure 19 depicts contour plots showing the thickness of the thawed layer, the average moisture content, and the total soil moisture content of the active layer. It is possible to compute the total soil moisture content of the active layer by multiplying the observed thaw depth by the average soil moisture content. This is a crucial parameter for permafrost studies since it offers direct information on the amount of water held in the active layer.

Muller (2017) showed an automated method using multi-offset ground penetrating radar (GPR) to forecast moisture content continually and layer depth for unbound granular pavements (UBG) at traffic speeds. The initial application of his techniques centered on the investigation of layer depth and moisture content at large project-level scales to assess layer depth as part of pavement rehabilitation investigations and determine the severity of suspected pavement damage caused by excessive moisture in the multilayer structure. Reeves (2010) used a second-generation 3D Noise-Modulated (NM-GPR) instrument for moisture content measurements (Figure 20). This apparatus may gather a sequence of nearby partly overlapping multi-offset measurements with ground coupling.

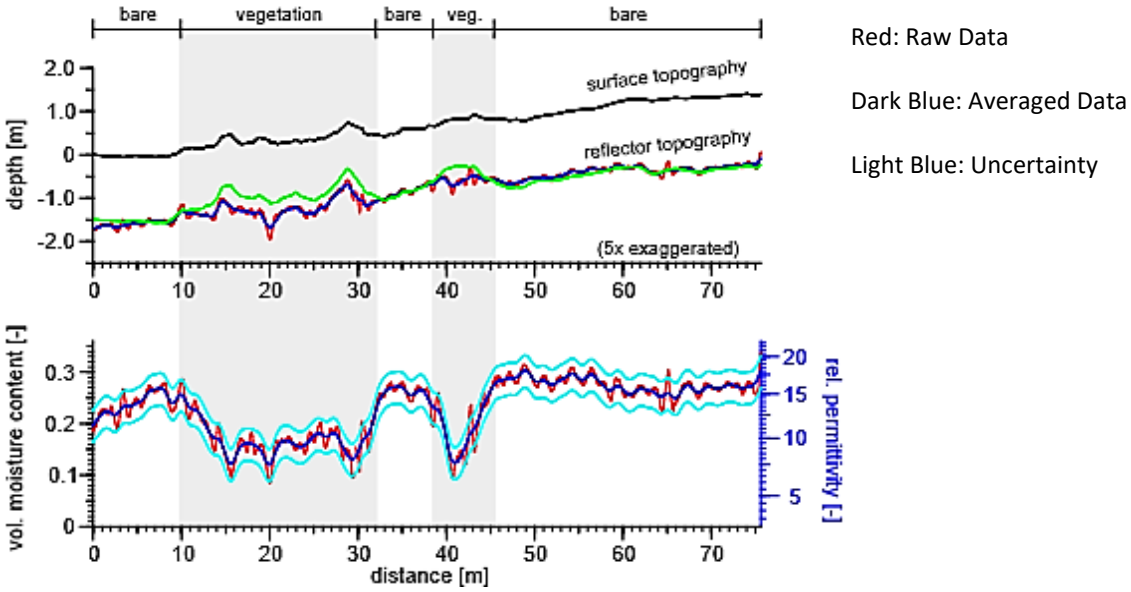


**Figure 18: Surface Topography, Reflector Depth, Relative Dielectric Permittivity, and Average Volumetric** Soil **Moisture Content (Wollschläger et al,. 2010)**

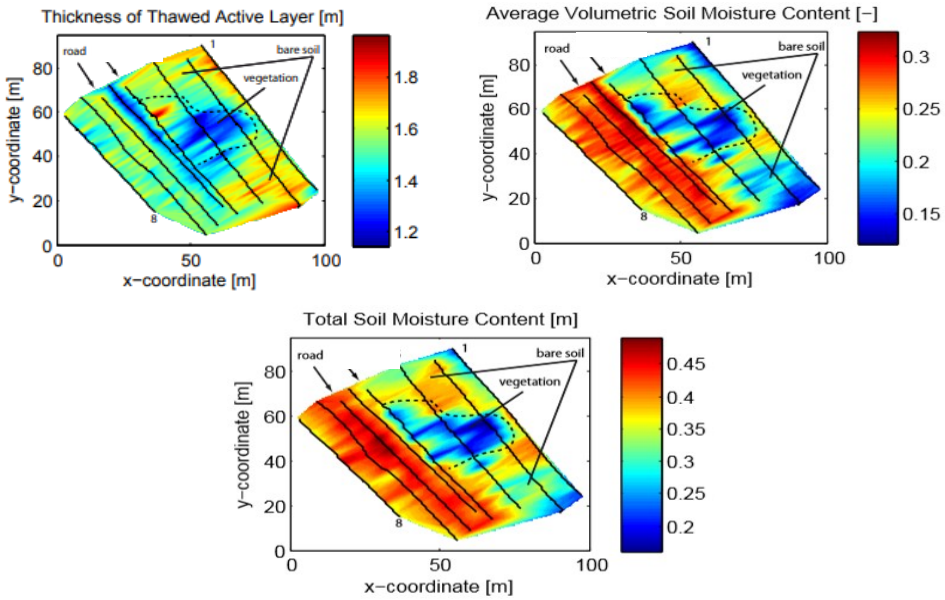


**Figure 19: Thickness of Thawed Active Layer, Average Soil Moisture Content, and Total Soil Moisture for the Thawed Active Layer (Wollschläger et al,. 2010)**


**Figure 20: Second Generation NM-GPR System Incorporating a Traffic-Speed 3D Ground-Coupled Antenna Array (Muller, 2017)**

In conjunction with the NM-GPR, a Traffic Speed Deflectometer (TSD) was used to establish the road surface's deflection profile. The TSD is a transportable device that employs Doppler vibrometers and complementing sensors to detect the velocity of the deflecting surface at predetermined offsets in front of the load's rear tire (Ferne et al., 2009; Baltzer et al., 2010; Kelley & Moffat, 2011). While moving down the road, the equipment was designed to collect four nearby wide-angle reflections and refraction (WARR) collects in a quasi-continuous manner. To calibrate the petrophysical relations for UBG pavement materials and create field moisture forecasts, a modified free-space (MFS) permittivity characterization technique was devised. A ray-path modeling-semblance (RM-S1) approach was also used to optimally match all near-transmitter receivers over the breadth of the array.

In June 2015, during the first Site Visit, NM-GPR readings were acquired. The next day, TDR and impulse GPR measurements were taken, and the site bitumen was sealed two days later. The May 2016 Site Visit 2 included the collection of NM-GPR, impulse GPR, and TDR data, as well as several physical samples throughout the length of the site. During Site Visit 2, eight samples (S1 to S8) were dug to estimate the pavement layers' built depth and collect material to measure the location's moisture content. S1 to S4 were taken at 100 mm intervals inside the pavement, and a subgrade sample was also obtained. The other four samples (S4 to S8) were collected from the second half of the site, and the subgrade and individual strata were sampled.

Figure 21 compares the measured response on one of the 32 NM-GPR channels during the first and second site visits with the impulse measurement acquired during the second site visit. Also highlighted are the approximate locations of sample sites S1 through S8.

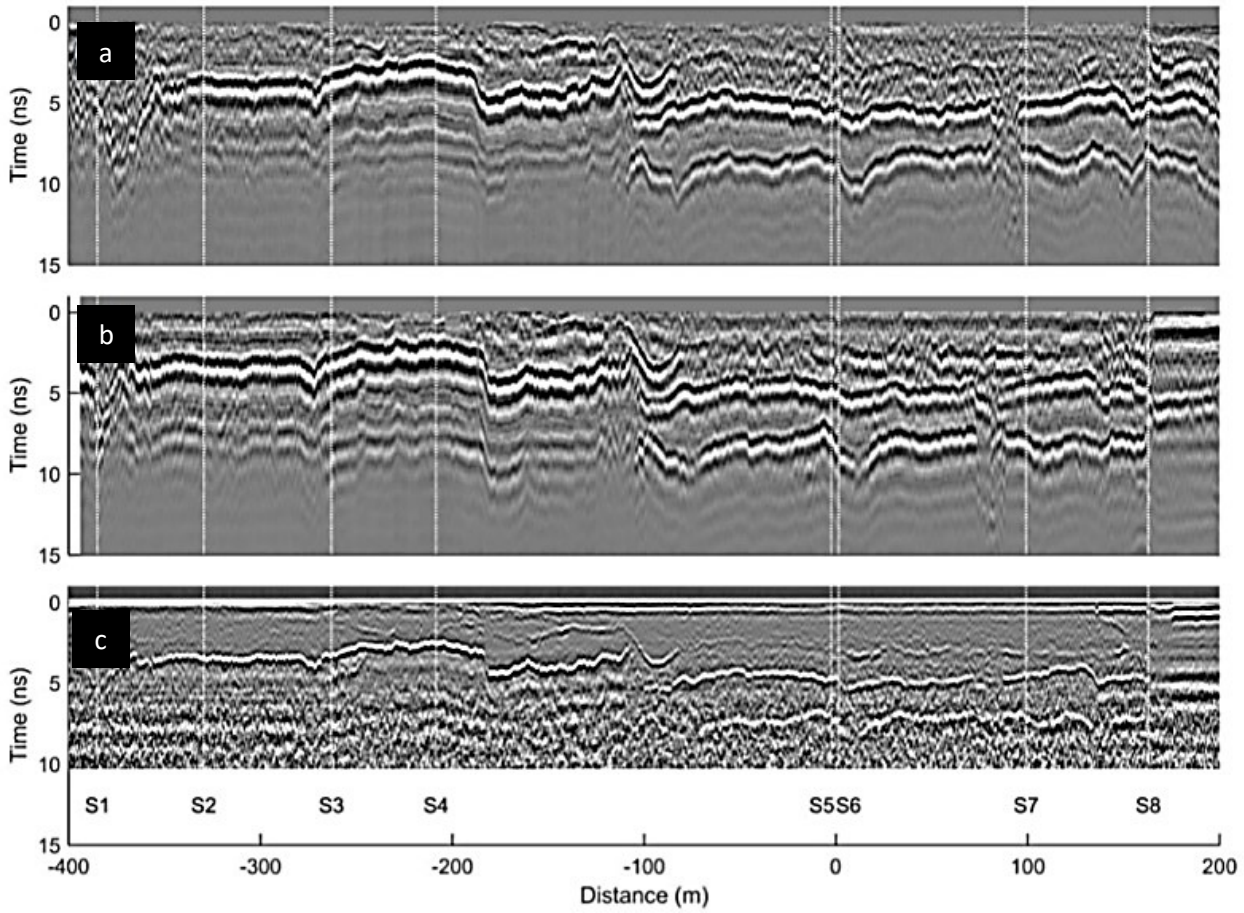


**Figure 21: GPR Scans along the Test Site of (a) Site Visit 1 Using NM-GPR, (b) Site Visit 2 using NM-GPR and (c) Impulse GPR (Muller, 2017)**

Figure 22 is a screenshot of the RM-S1 analysis for the measured multi-offset response (Figure 22a), the optimized ray-path model determined for the tested location (Figure 22b), and an image of the calculated layer depth, dipping angle, relative permittivity, and predicted volumetric moisture content (Figure 22c) (Figure 22c). Figure 22d depicts volumetric content projections for previously examined

areas along the route. The RM-S method was designed to make processing multi-offset GPR data constantly gathered along a road using 3D GPR equipment more uncomplicated and efficient.

Figure 23 displays the relevant volumetric moisture contents computed using the previously estimated petrophysical relation. The researchers determined a strong connection between the volumetric moisture content predictions of the RM-S1 model and the actual sample findings. Other studies found that TDR and common-offset GPR had a similar tendency to RM-S, although with persistently lower permittivity values. It is crucial to note that using alternative sensor configurations (common midpoint, multiple arrays, standard offset) increases the capability to identify layer interfaces and estimate layer depths. The greater the precision of the depth forecasts, the greater the precision of the permittivity estimate.

Muller found from this investigation that the predictions of this method corresponded well with actual measurements of layer depth and moisture content of pavement layers. Compared to embedded TDR sensors and common-offset GPR measurements of subsurface reflectors, permittivity predictions followed similar temporal patterns with somewhat lower values. Even though data could be gathered at traffic speeds, layers had to be recognized and monitored, most likely based on spot assessments at intervals along the road, as one of the study's limitations. In addition, it was emphasized that this method could only be used for the subgrade, which was usually the lowest coherent interface. Therefore, integrated TDR or other sensors would still be necessary for subgrade moisture monitoring.

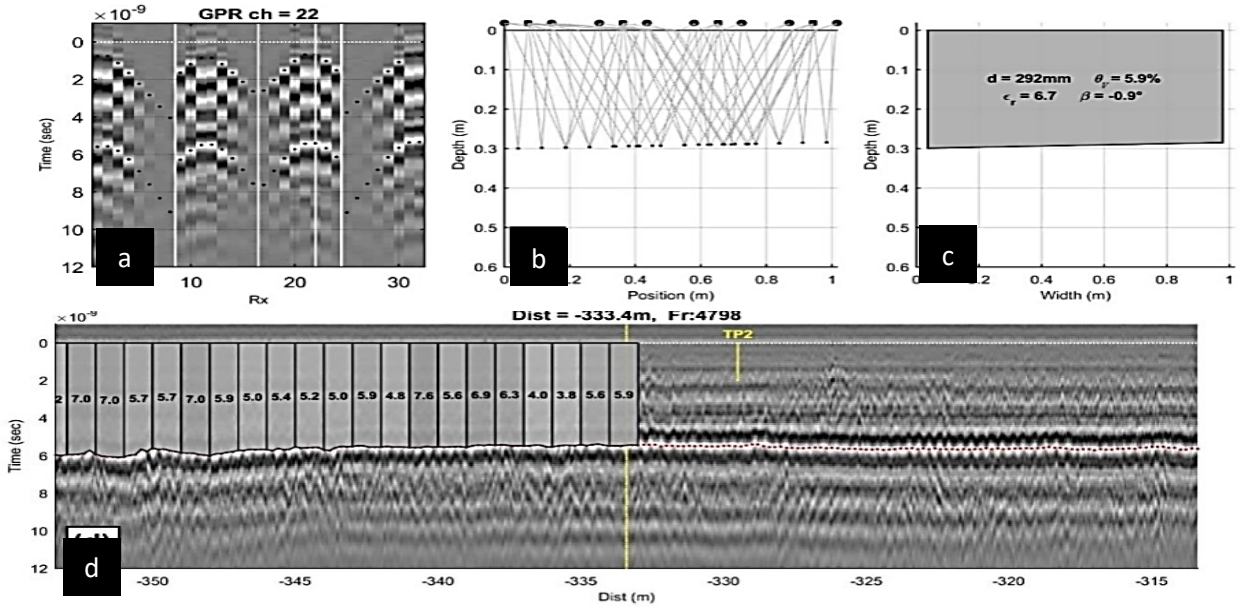


**Figure 22: Multi-Offset Analysis using the RM-S1 Approach Showing (a) Measured WARR Response with Airwave and Optimized Ray-Path Travel Time Predictions Overlaid (black dots); (b) Calculated Ray-Path Geometries; (c) Calculated Layer Depth (d), Volumetric Moisture Content (Muller, 2017)**

## 2.4 Other Moisture Measurements

White (2019) researched to optimize pavement laying costs by utilizing material compaction energy and moisture content to enhance the quality by

1. Achieving the minimal critical engineering parameter values throughout the site
2. Limiting variability of critical engineering parameter values over the entire site
3. Restricting spatial areas of non-compliance
4. Control moisture contents to ensure post-placement volumetric stability

The propriety “validated intelligent compaction” (VIC) technology was employed to help the construction process and quality evaluation. They highlighted the variation in QC/QA testing procedures for detecting the water content (Figure 24). Zero shows the optimum moisture content with -4% and +2% limits shown by the orange dashed lines. This demonstrated that 79% of all measurements did not adhere to the stated moisture control limits. Quality evaluation criteria were devised utilizing intelligent compaction to highlight regions of noncompliance (Figure 25a). Moisture was measured based on its connection to the density of the material, as illustrated in Figure 25b. Water was added or withdrawn until obtaining the appropriate density.

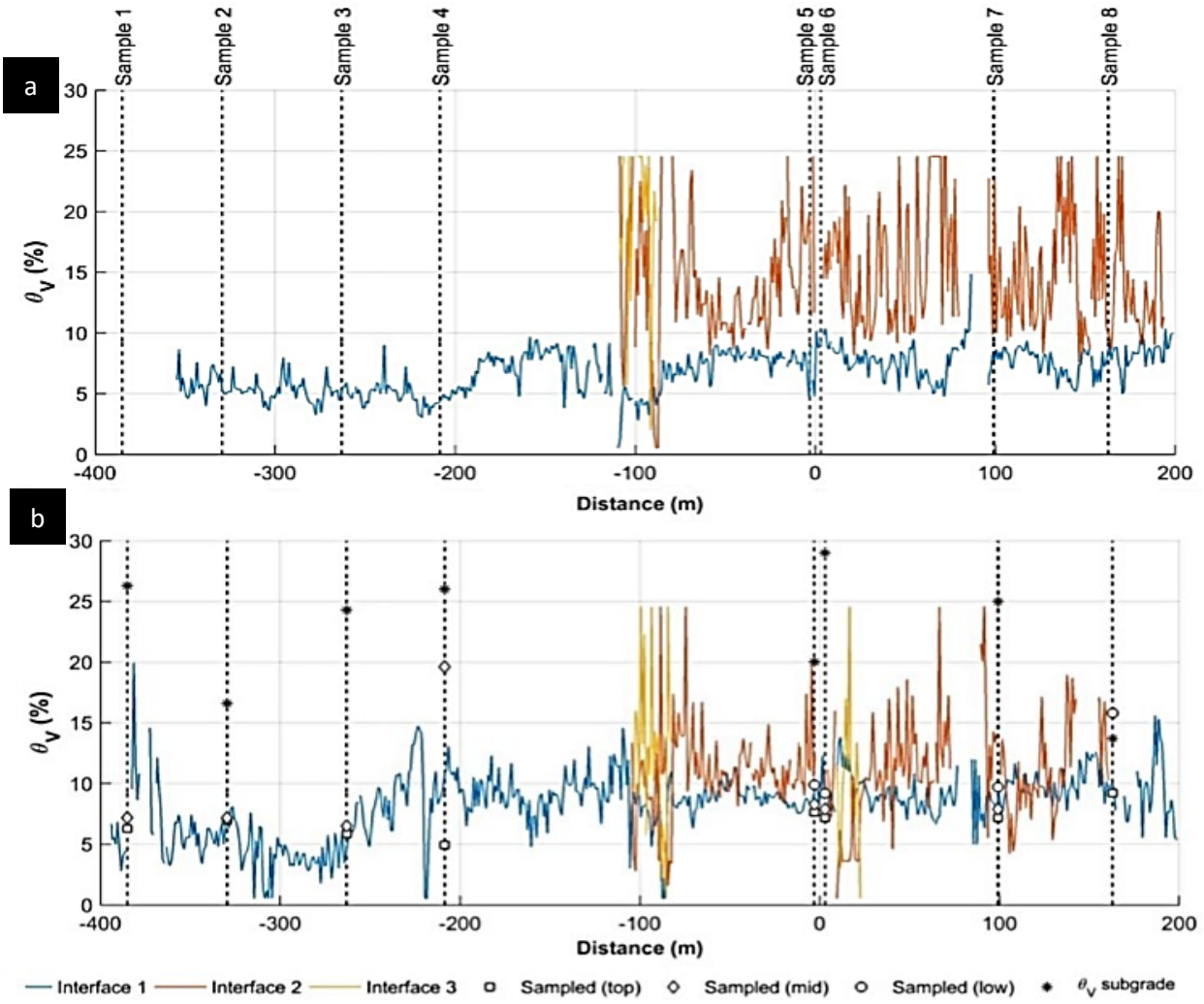


**Figure 23: Volumetric Moisture Content Predictions from Permittivity Results during (a) Site Visit 1 and (b) Site Visit 2 (Muller, 2017)**

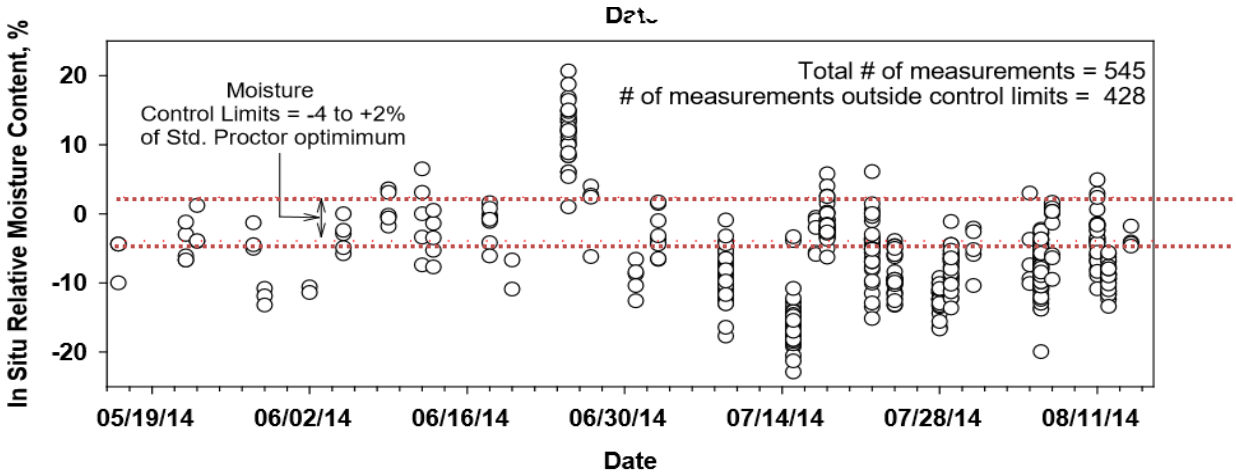


**Figure 24: Moisture Content Measurement Variability (White, 2019)**

| Quality Assessment Criteria | Requirement Meet? | Action Requirement |
|---|---|---|
| (1) 90% of IC-MVs ≥ 0.80*IC-TV | **NO. 79%** | Recompact areas of low IC-MV and remap area. |
| (2) Standard deviation of the IC-MV ≤ 0.35*IC-TV | YES. 18.9 <20.1 | None required |
| (3) ICM-MV proof mapping area has no contiguous, isolated areas that larger than 80ft² | **NO. one isolated area as noted** | Reduce moisture content by scarifying and drying. Will be re-compacted and IC-MV map generated. |
| (4) w% ≥ the hydro-collapse values | YES | None required |

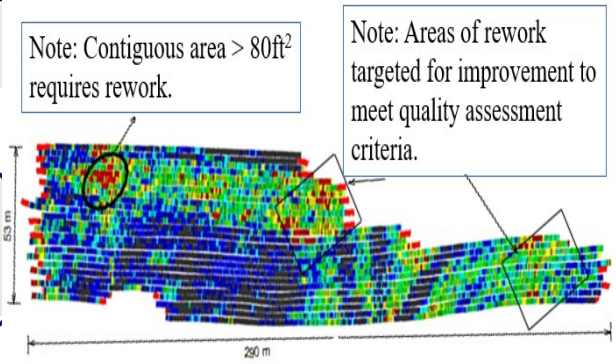


**Figure 25: (a) Quality Assessment Criteria, (b) Intelligent Compaction Map (White, 2019)**

Genc et al. (2019) recommended estimating the frost depth and the number of freeze-thaw cycles under a specific highway using continuous meteorological and soil data. Their effort was to produce a method to prevent the occurrence of frost-induced heaving, depressions, fissures, potholes, and unpleasant travel. This work used soil moisture, matric suction, and temperature factors for computational modeling analysis. The chosen test area was instrumented with various soil moisture, matric potential, and temperature sensors implanted in five boreholes at depths ranging from 0 to 8 meters (Figure 26).

Several alternatives were tested to determine the best practical sensor for measuring the soil's moisture content. After an exhaustive study of commercially available devices, they opted to employ the GS1 sensor by Meter Environment. Due to its calibration technique and precision, the Decagon Devices MPS-6 sensor was chosen to detect the soil's matric potential. The selected test area had a weather station for measuring air temperatures. The sensors and weather stations used for this experiment are shown in Figure 27. After installation and data collection, a remote connection was established with the data logger, and the stored information was retrieved. Ultimately, continuous moisture content, matric potential, and temperature measurements were acquired. Figure 28 illustrates an example of the obtained data for continuous moisture measurements for sensors set at a depth of 1 foot in the five boreholes in this area.

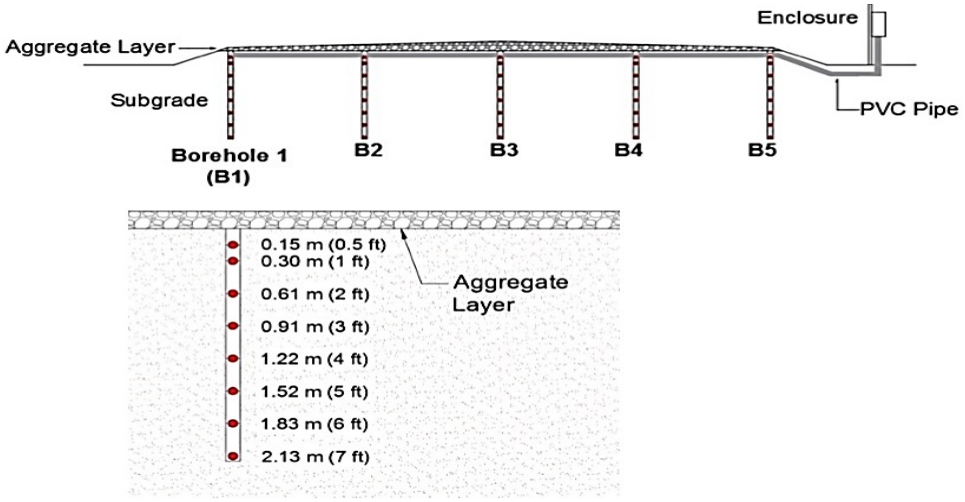


**Figure 26: Cross-Sectional View of Roadway and One Borehole (Genc et al., 2019)**

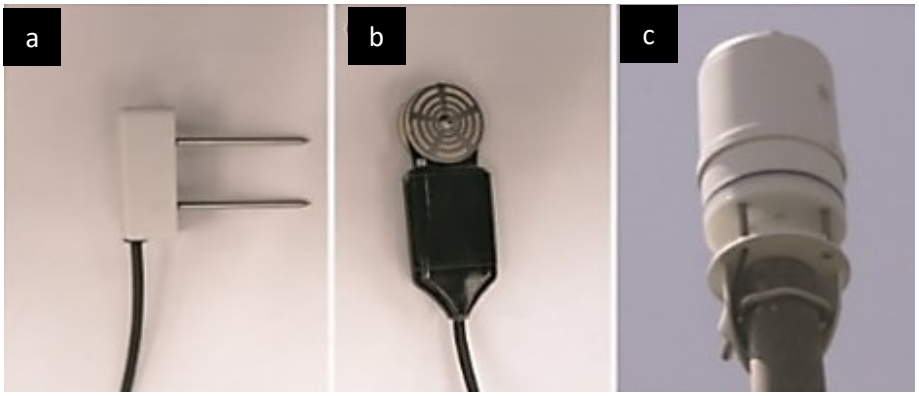


**Figure 27: (a) GS1 (b) MPS-6 (c) Weather Station (Genc et al., 2019)**

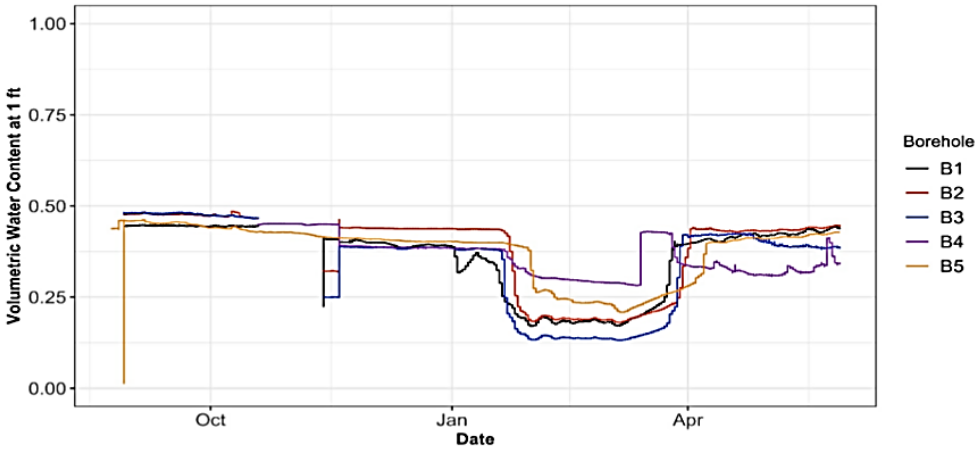


**Figure 28: Continuous Moisture Measurement (Genc et al., 2019)**

Campbell (2019) described advances altering how soil moisture is assessed. This study's primary purpose was to install a moisture and temperature system to provide the required data for a model to estimate

road weight constraints. Three sensors positioned at distances of 6 inches, 18 inches, and 30 inches were used to measure the relative humidity. In addition, a comprehensive weather station was installed at the site for temperature observations. Fourteen days of continuous moisture measurements at 6 inches were generated for various regions (Figure 29).

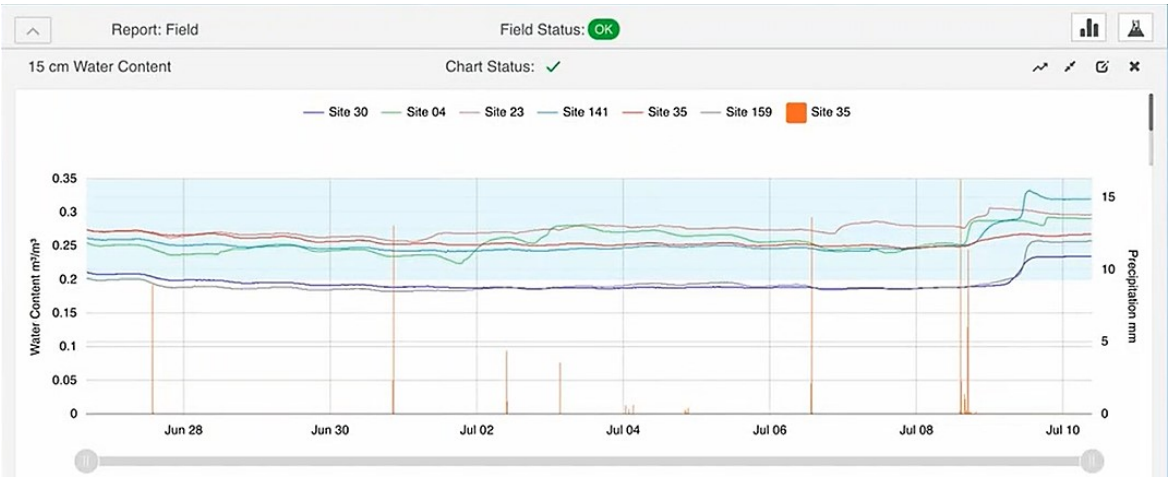


**Figure 29: Example of a Continuous Moisture Measurement (Campbell, 2019)**

Grabe and Mahutka (2005) established via modeling and field measurements that the regional variation of soil stiffness and pavement roughness displayed the same statistical properties. In addition to the number of vehicle passes and their load characteristics, they discovered that the geographical variation influenced the pavement's uniformity in soil stiffness. They determined that the variation in the foundation layers' stiffness affected the pavement's durability.

Brand et al. (2013) performed a historical review of research about the effects of nonuniform foundations on the performance of pavements, particularly rigid pavements. They determined that "certain nonuniform support of concrete slabs may cause much larger tensile stresses than uniform support, especially when varied loading locations and curling circumstances, soft support along the pavement edge, and preexisting fractures are considered." Several case studies illustrating the effect of nonuniform pavement foundations were also presented.

White et al. (2016) did a comprehensive analysis of the uniformity of earthwork in Iowa and the efficacy of their current requirements in delivering a consistent end product. One of their results was that the variable moisture content contributed significantly to the lack of homogeneity of the foundation layer of the pavement. They suggested the following three approaches to enhance uniformity:

1. Enhance the current moisture and moisture-density specifications
2. Develop Alternative DCP/LWD-based (strength/stiffness-based) QC/QA specifications
3. Incorporate intelligent compaction (IC) measurements into QC/QA specifications

Quoting from a comprehensive study performed by White et al. (2021), the following key challenges in terms of uniformity of foundation in general and moisture content in particular:

1. Substantial spatial variability (nonuniformity) exists in newly constructed pavement foundations for the range of materials tested

The overlying aggregate base layer will be nonuniform if the subgrade layer is nonuniform

1. Limited geotechnical testing (covering less than 1% of a given work area) is used to accept the engineering support values of pavement foundations, resulting in low reliability
2. Limited technology is available to help earthwork and paving contractors improve the field control of pavement foundation layers during construction
3. Most methods for quality inspection testing do not qualify as direct mechanistic measurements

# Chapter 3: Laboratory Methodology

## 3.1 Testing Program

The experimental plan consisted of traditional and large-scale laboratory testing. The flowchart of testing and analysis of each geomaterial is shown in Figure 30. As soon as the geomaterial arrived in the laboratory, it was processed, dried, and subjected to index tests such as particle size distribution (sieve analysis, ASTM 6913), Atterberg limits (ASTM D4318), and specific gravity (ASTM C127/128). These index results were used to classify the geomaterial according to the Unified Soil Classification System (USCS, ASTM D2487).

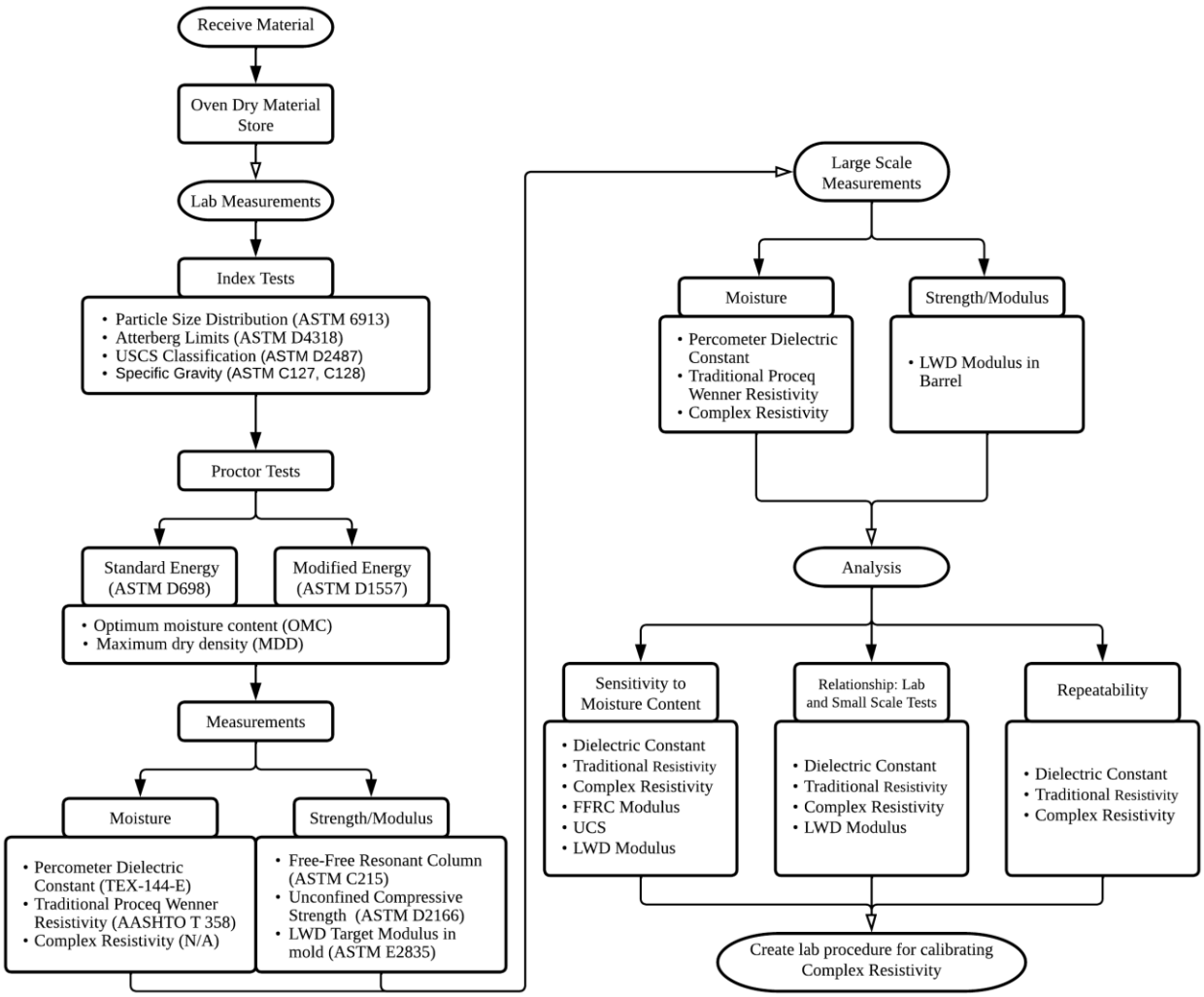


**Figure 30: Testing Flowchart**

The next step consisted of the Proctor tests to obtain the optimum moisture content (OMC) and the material's maximum dry density (MDD). The specimens prepared for this step and the subsequent laboratory testing were prepared in different sizes and with different compaction efforts depending on the texture of the geomaterial. The fine-grained soils and sandy materials were compacted per the

Standard Proctor energy (ASTM D698). The coarse-grained materials were compacted as per the Modified Proctor energy (ASTM D1557). The specimens were prepared at longer lengths than those prescribed in the standard while maintaining the compaction energy to ensure rigorous strength and modulus test results. The fine-grained specimens were compacted in molds of 4 in. diameter by 8 in. height, and the coarse-grained specimens were compacted in 6 in. in diameter and 8.5 in. length.

## 3.2 Material Selection

Six geomaterials were selected as a baseline for verification of the outcomes of this study, as shown in Table 2. Two fine-grained soils, both classified as CL, two sandy materials classified as SM and SP, and two coarse-grained materials classified as GW, were used in this study. These geomaterials provide a reasonable basis for materials with different characteristics in terms of their interaction with moisture, levels of suction, levels of moduli, and their use as compacted geomaterials.

**Table 3: Geomaterials Used**

| Soil Type | Classification | Source |
|---|---|---|
| **Fine-Grained** | CL-1 | Texas |
| | CL-2 | MnROAD |
| **Sandy** | SM | Texas |
| | SP | MnROAD |
| **Coarse-Grained** | GW-1 | Texas |
| | GW-2 | Texas |

## 3.3 Laboratory Measurements

As soon as the OMC and MDD were established, a series of five specimens were prepared at the following five nominal moisture contents: OMC, OMC±10%×OMC (or OMC±1% if the OMC is less than 10%), and OMC±20%×OMC (or OMC±2% if the OMC is less than 10%). These specimens were demolded and then subjected to a series of moisture content tests, namely Dielectric Constant using a Percometer (Tex-144-E, https://www.humboldtmfg.com /datasheets/Percometer.pdf), Traditional Resistivity using a Wenner probe (AASHTO T 358, https://www.screeningeagle.com/en/sales-flyers/SF-resipod), Complex Resistivity using the prototype being developed in this study.

Since all these tests are non-destructive and rapid, each specimen was subjected to the free-free resonant column (FFRC, ASTM C215) test to obtain the seismic modulus and then the unconfined compressive strength test (ASTM D2166).

A series of five specimens were prepared in a separate mold used in conjunction with the newly suggested method for estimating the target modulus of LWD to obtain the lab LWD modulus.

### 3.3.1 Dielectric Constant (DC)

A Percometer, shown in Figure 31, measured each specimen's dielectric constant (DC). The percometer emits a frequency of 40-50 MHz into the soil and then records the capacitance change between the probe and soil from the change in water content and ion polarization on grain surfaces. Five

measurements on top of the specimens and five on the bottom were conducted and averaged to obtain the representative DC of each specimen. Four measurements followed around the sample's top and bottom surface areas, and the fifth was recorded in the middle of the surface.

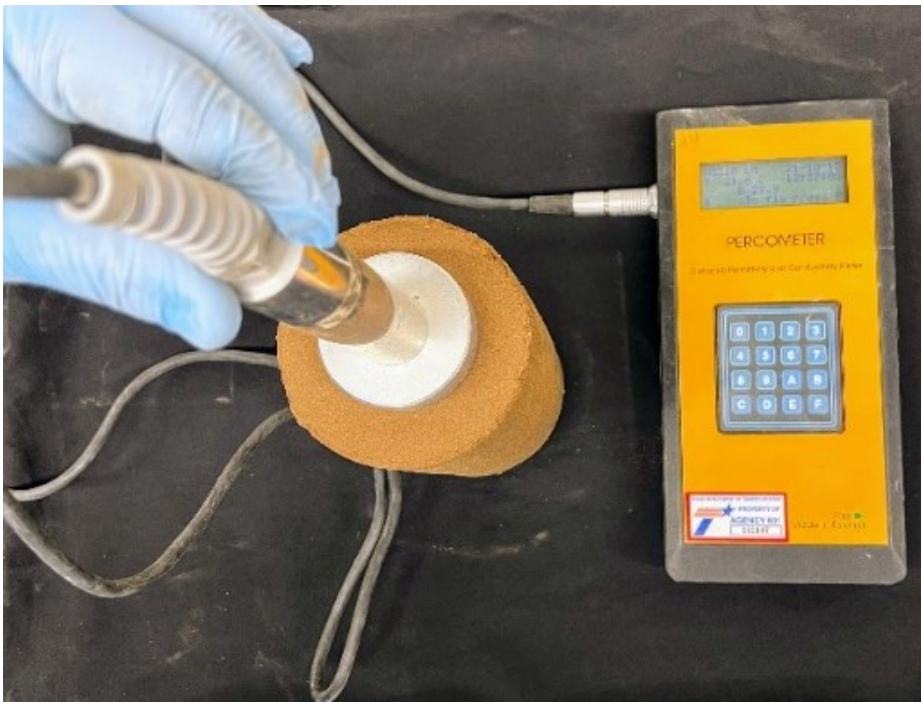


**Figure 31: Percometer used for Measuring Dielectric Constant**

### 3.3.2 Traditional Resistivity (TR)

A Wenner probe developed for measuring concrete resistivity, as shown in Figure 32a, was used to measure each specimen's resistivity. The probe operates at a frequency of 40 Hz, a current of 10 µ-amps to 50 µ-amps to compute the resistivity in kohm-cm. Current is injected into the soil from the two outer electrodes, while the two inner electrodes measure the passing current. Five measurements were taken at 60-degree intervals around the diameter of the specimen. The representative resistivity was the average of the five readings. The TR meter was saturated on low-resistivity soils as the instrument used its highest current setting and had voltages below its measurement threshold. A customized device with the same frequency and currents but a larger voltage measurement range was developed (Figure 32b). After proper calibration, the two devices provided almost identical readings.

The Wenner array functions on the expectation that current is being injected into a homogenous half-space (a large plane such as the ground). The voltage through the half-space is expected to decrease with distance; however, with the dimensions of the laboratory specimens, using a fixed probe spacing impacts the resistivity measurements. By using a finite-difference model, Cartesian coordinates, and a 50-mm node spacing, the geometric adjustment factors were determined to be 2.74 for the 4-in. diameter specimens and 1.82 for the 6-in. diameter specimens. The obtained resistivity values are divided by these correction factors.


**Figure 32: (a) Traditional Wenner Array (b) Laboratory-Created Array**

### 3.3.3 Seismic Modulus (SM)

After the two moisture tests, the seismic modulus of the specimen was found using the free-free resonant column testing (per ASTM C215), as shown in Figure 33. An impulse is imparted to the specimen with a small hammer equipped with a load cell. The vibration of the signal within the specimen is measured with an accelerometer. Those two signals are transformed into the frequency domain to measure the resonant frequency of the specimen. The resonant frequency of the specimen is determined from those measurements that can be readily converted to a seismic modulus. Nine measurements on each surface (top/bottom) were averaged to obtain the representative seismic modulus.

**Figure 33: Free-Free Resonant Column Testing for Seismic Modulus**

### 3.3.4 Unconfined Compressive Strength (UCS)

Figure 34 demonstrates a clay specimen being tested using a Sigma 1 Automated Load Test System at a strain rate of 1% per minute. After the UCS tests were determined, each specimen's moisture content was obtained via oven drying.


**Figure 34: Unconfined Compressive Strength Testing**

### 3.3.5 Lightweight Deflectometer Modulus (LWD)

The lightweight deflectometer modulus of each soil was obtained by preparing another set of specimens in a 6-in. by 8.5-in. mold provided by the LWD manufacturer, as shown in Figure 35. The diameter of the LWD plate measured 6 in. (150 mm), and the load applied was nominally 800 lbs. (3535 N). The average LWD deflections were obtained from three consecutive drops after three conditioning LWD drops. The average deflections were then converted to moduli.

## 3.4 Complex Resistivity (CR)

Complex Resistivity (CR) is a measurement of electrical impedance as a complex number that uses the same four-electrode geometries as the TR measurement in Section 3.3.2. Two outer electrodes inject current, and the inner electrodes measure voltage difference. Resistivity is a complex number that can be calculated by dividing voltage and current. The CR measurement is more stringent than TR in the following four areas:

1. The CR equipment allows measurement at up to ten frequencies ranging from 60 Hz to 40 kHz.
2. The CR equipment injects current at up to ten amperage levels ranging from 1 µA to 1 A. These current levels are fixed, not auto-ranged, as in the TR equipment.

3. The magnitude and phase of the injected current and the voltage are directly measured to monitor possible electrode/material interaction complications.
4. The frequency dependence of electrode and saturation polarization becomes an approximation to a diffusion equation model[1] rather than the simpler Poisson's equation[1].

**Figure 35: Lightweight Deflectometer Testing**

Figure 36 shows the two complex resistivity prototypes. Figure 36a was the first laboratory prototype (version 6 electronics), and Figure 36b (version 8 electronics) was used in the last 6 months of testing. Both functioned similarly, measuring numerous frequencies and currents with square or sine waves. The Version 6 device operated at too high of a current range to function on the coarse/dry bases. Version 8 had an improved analog-to-digital (A/D) convertor, a better dynamic range at lower currents on the voltage channels for the dry/coarse bases, and improved ruggedness/reliability while making access and maintenance easier.

[1] Diffusion equation ($\nabla^2 V=K\ \delta V/\delta t$) where V is voltage, K represents a spatial function of resistivity and polarization and t is the time.
[2] Poisson's equation ($\nabla^2 V=f$) where V is voltage and f represents a spatial function of resistivity.

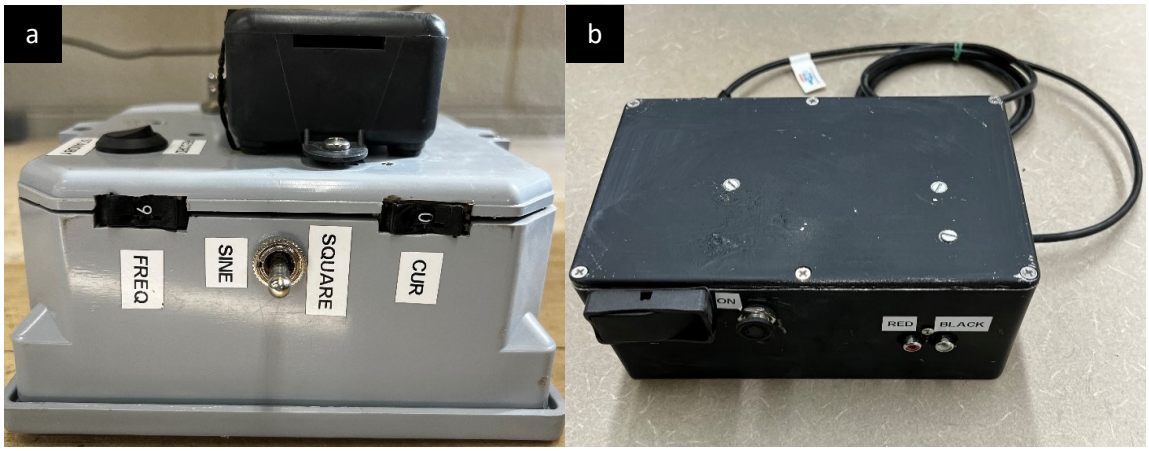


**Figure 36: Complex Resistivity Prototypes and Arrays**

Two arrays were made to meet laboratory compaction standards. The cradle array was used to test Proctor specimens by allowing them to sit on four solder-coated brass electrodes, as shown in Figures 37a and 37b. With a larger electrode contact area and uniform support across the specimen surface, the more delicate and wet specimens performed better compared to the earlier design of the four-probe electrode in Figure 37c. The larger distributed electrodes required a separate geometric correction factor calculated by finite difference modeling. The two Wenner arrays (Figures 37c and 37d) were used to test large-scale specimens. The three arrays function the same. The measurements are taken with a phase-sensitive detector that multiplies the voltage and current signals measured by an in-phase sine-wave and a 90° delay sine-wave. Hardware multiplication using the in-phase or 90° delay square waves produces a real-time Fourier transform of the measured signal (real and imaginary). The imaginary value measures polarization, while the real value measures resistivity. This measurement rejects nonlinear distortion and noise more strongly than the simpler TR circuitry, which combines them into one resistivity value. The 10 frequencies and currents are provided in Table 3. The data collection procedure follows the following steps:

1. The specimen is set on top of the brass electrodes, and the power button is switched on
2. The desired frequency is selected (starting frequency was set to 3)
3. The record and square wave are turned on
4. Run through all currents, 0-9, then finish with 0 (typically .5 to 1 sec. between changes)
5. Turn the square wave off, then the record switch,
6. Change frequency and repeat from step 3

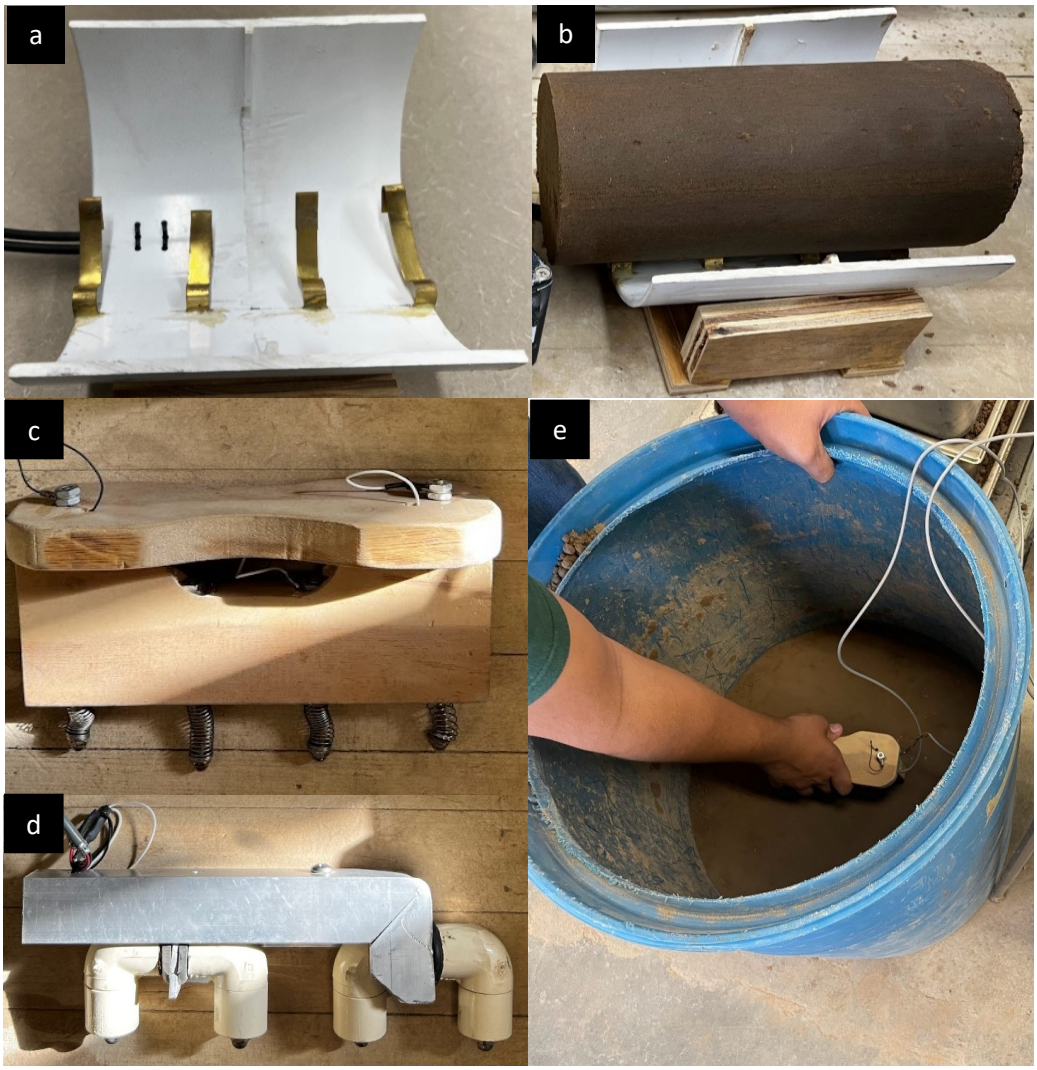


**Figure 37: (a-b) Cradle Array and (c-d) Wenner Arrays**

**Table 4: Frequencies and Currents**

| Switch | Current (µA) | Frequency (Hz) |
|---|---|---|
| 0 | 12 | 33900 |
| 1 | 25 | 5.5 |
| 2 | 61 | 13.3 |
| 3 | 100 | 62.9 |
| 4 | 156 | 125 |
| 5 | 228 | 630 |
| 6 | 364 | 1600 |
| 7 | 515 | 5820 |
| 8 | 870 | 12200 |
| 9 | 1,300 | 18300 |

## 3.5 Large-Scale Measurements

The large-scale tests were carried out in the laboratory by preparing 18-in. diameter by 24-in. height specimens constructed within a 35-gallon barrel, as shown in Figure 38. Five specimens at the five target moisture contents (OMC, OMC±10%×OMC or OMC±1% if the OMC is less than 10%, and OMC±20%×OMC or OMC±2% if the OMC is less than 10%) were compacted and measured.

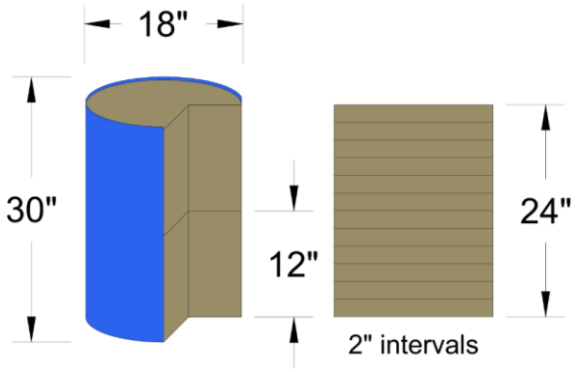


**Figure 38: Schematic Diagram of Large-Scale Test Specimen Set-up**

A concrete mixer (Figure 39) was used to prepare the materials to the desired moisture content. An adequate amount of dry geomaterial necessary to achieve the desired density for the volume of a 2-in. lift was placed in the mixer, and a precise amount of water was added to the soil with a water sprayer to ensure accurate moisture content. The moist material was then transferred into the container and compacted to the desired density with a concrete stamper. This process was repeated until a height of 12 in. was achieved. At that height, the moisture content measurements (with the Percometer, traditional resistivity probe, and the complex resistivity probe) and LWD measurements were obtained at three separate locations. Each specimen was then built up to its final height of 24 in. using 2-in. lifts and tested using the three moisture probes and LWD. Soil samples were extracted at every 4 in. height to obtain oven-dry moisture contents.

The laboratory measurements were taken at the sixth layer (12-inch height) and the 12th layer (24-inch height). Five readings of the dielectric constant, pictured in Figure 40a, are recorded and averaged—one reading in the middle and four between the barrel's center and perimeter. The traditional resistivity was measured next. Five readings were recorded in the middle of the barrel and averaged, as shown in Figure 40b. Based on numerical analysis, a correction factor was not necessary for the barrels. Next, the complex resistivity was recorded in the middle of the barrel, with a Wenner array pictured in Figure 40c. Lastly, the LWD modulus, Figure 40d, was recorded. The average of measurements at three different positions was reported as the corresponding LWD modulus.


**Figure 39: (a) Mixer and (b) Concrete Stamper with Barrel Used to Prepare Large Scale Specimens**


**Figure 40: Large Scale Measurements (a) DC (b) TR (c) CR (d) LWD**

# Chapter 4: Results of Laboratory Measurements

This section discusses the results from three diverse geomaterials in detail. The raw data from all tests on the six geomaterials are represented in the appendix. Presented in Table 4 is a summary of the soil parameters of the six materials tested, including their Atterberg limits and gradations.

**Table 5: Summary of Index Properties**

| Soil | | Atterberg Limits | | Constituents, % (dry sieve) | | | Compaction Parameters | | Properties at OMC[1] | | | |
|---|---|---|---|---|---|---|---|---|---|---|---|---|
| Type | Classification | LL | PI | Gravel | Sand | Fines | OMC[1] (%) | MDD[2] (pcf) | DC[3] | R[4] (Kohm-cm) | SM[5] (ksi) | UCS[6] (psi) |
| Fine-Grained | CL-1 | 33 | 13 | 0.0 | 27.6 | 72.4 | 14.1 | 109.2 | 26.5 | 0.7 | 8.7 | 9.8 |
| | CL-2 | 27 | 8 | 3.0 | 38.6 | 58.4 | 14.4 | 118.9 | 13.5 | 1.2 | 7.0 | 11.9 |
| Sandy | SM | No PI | | 0.0 | 83.2 | 16.8 | 9.5 | 118.0 | 14.2 | 2.1 | 6.6 | 5.5 |
| | SP | 20 | 2 | 17.7 | 79.9 | 9.1 | 9.8 | 130.6 | 21.0 | 3.0 | 32.4 | 22.8 |
| Coarse-Grained | GW-1 | 16 | 2 | 60.1 | 39.9 | 0.0 | 4.7 | 148.3 | 16.5 | 3.2 | 16.7 | 3.0 |
| | GW-2 | 18 | 3 | 52.9 | 43.1 | 4.0 | 5.3 | 149.6 | 13.1 | 10.6 | 16.5 | 3.3 |

[1]Optimum Moisture Content, [2]Maximum Dry Density, [3]Dielectric Constant, [4]Traditional Resistivity, [5]Seismic modulus, [6]Unconfined Compressive Strength

Figure 41 demonstrates the moisture density curves of the CL-1, SM, and GW-1 geomaterials. The CL-1 and SM soils were tested at more moisture contents than the five target moisture contents to understand better the testing scheme and anticipated trends of the dielectric constant, traditional resistivity, and complex resistivity. The GW-1 was tested only at the five nominal moisture contents.

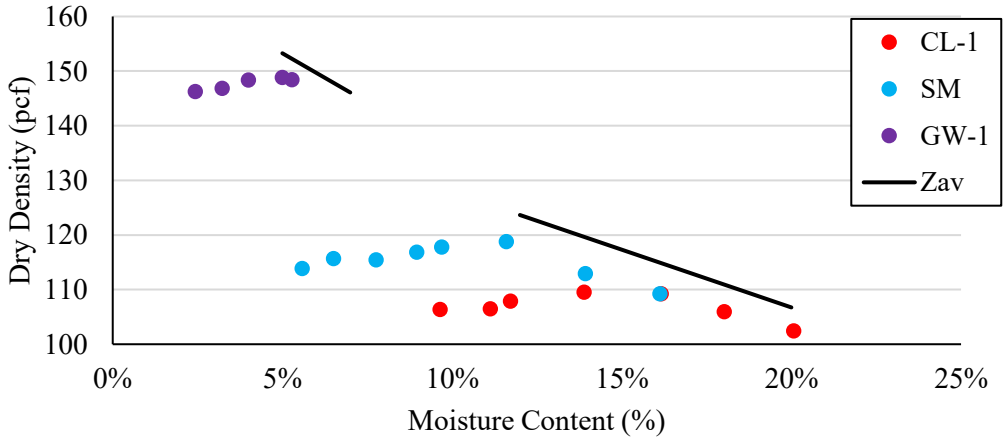


**Figure 41: Moisture-Density Curve of CL-1, SM, and GW-1**

## 4.1 Dielectric Constant

Presented in Figure 42 are the variations of the dielectric constants of the three geomaterials with moisture content. The error bar for each data point corresponds to the ±1 standard deviation bound to demonstrate the consistency of the test method at different moisture contents. A conclusive pattern cannot be observed for the SM and CL-1 materials. The GW-1 material was the most susceptible to moisture increases as its dielectric constants increased with moisture. Due to the high variability, the dielectric constant data for the large-scale specimens are presented in the appendix.

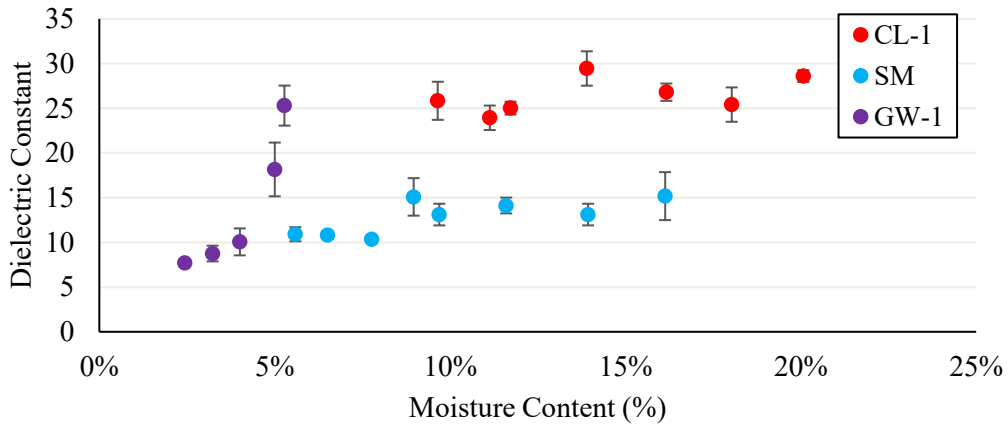


**Figure 42: Dielectric Constant Data of CL-1, SM, and GW-1**

## 4.2 Traditional Resistivity

### 4.2.1 Proctor Specimens

Figure 43 shows the variations of the resistivity measurements with moisture content for the three materials. A consistent pattern is observed among the three materials but over different ranges. The resistivity change with moisture content is large at lower moisture contents and becomes nearly insensitive as the moisture content exceeds OMC. This variability is higher for the GW material. The moisture-resistivity curve shape and higher variability for the larger aggregate are consistent with the expected volumetric decrease in double-layer conduction as the surface area decreases with grain size increase.

Using the degree of saturation instead of moisture content is desirable. Since the determination of the degree of saturation requires an accurate measurement of the specific gravity of the materials, it was deemed impractical for this study. Instead, an alternative normalization process proposed in the NCHRP 10-84 was pursued. The ordinate (y-axis) parameters were normalized by dividing a given parameter at a given moisture content by the corresponding value at OMC. The abscissa (x-axis) was normalized using Equation 1.

$$Normalized\ Moisture\ Content = \frac{Actual\ Moisture\ Content - OMC}{OMC} \quad (1)$$

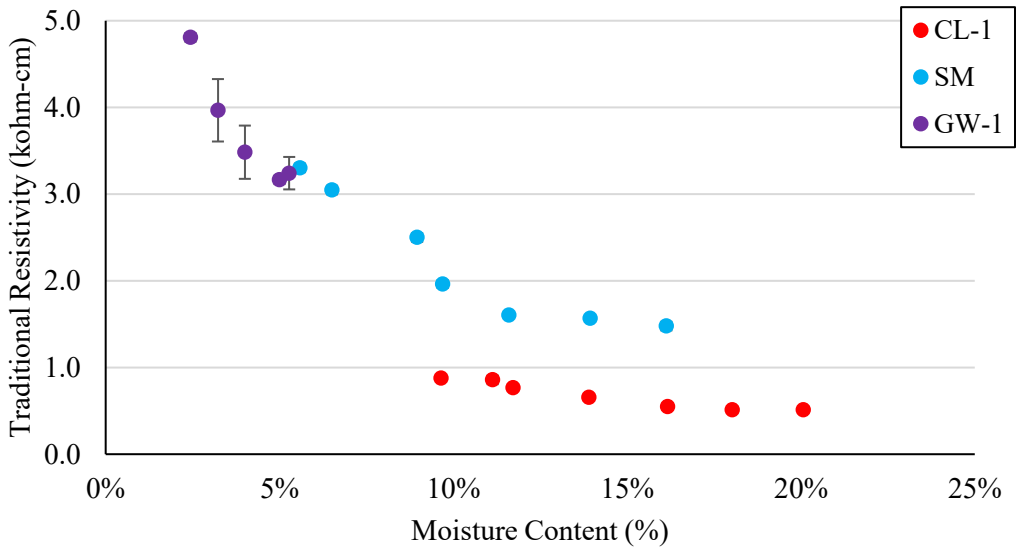


**Figure 43: Traditional Resistivity Data of CL-1, SM, and GW-1**

Figure 44 shows the variations of the normalized traditional resistivity of the geomaterials with normalized moisture content. The vertical line passing through zero indicates the optimum moisture content. The specimens with negative normalized moisture contents are dry of OMC, and the positive ones are wet of OMC. The solid line indicates the trend that all soils follow with some anticipated dispersion. For specimens prepared dry of OMC, a rather steep decrease in the normalized resistivity with an increase in the normalized moisture content is observed. However, for the specimens prepared wet of OMC, the normalized resistivity is less sensitive to the change in the moisture content. This trend makes sense since the electrical properties of the water dominate the response at moisture contents wet of OMC. The data dispersion among different soils indicates the need for thorough laboratory calibration of the resistivity-moisture content relationship before field implementation.

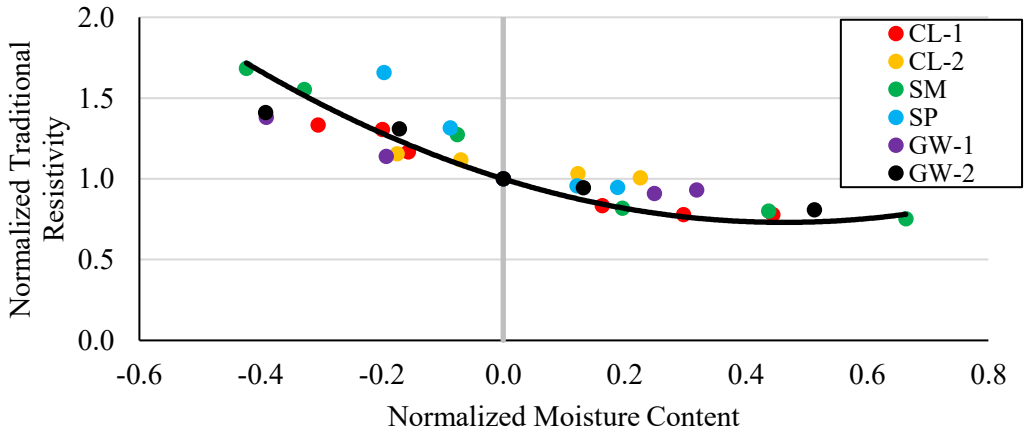

**Figure 44: Normalized Traditional Resistivity Data of all Geomaterials**

### 4.2.1 Impact of Specimen Size

Comparing the different sizes of the specimens was critical in understanding the impact of moisture on the different measurements. The results from the 4 in.-diameter and 6 in.-diameter specimens of the two clayey and two sandy geomaterials are compared in Figure 45. The results from the two gravelly materials are not included since it was impossible to prepare a homogenous 4-in. specimen from them. The resistivity measurements adjusted for the geometry for the 6 in.-diameter specimens are close to corresponding values from the 4 in.-diameter specimens. Some dispersion is noticed that may be contributed to the inevitable variation in moisture contents among specimens.

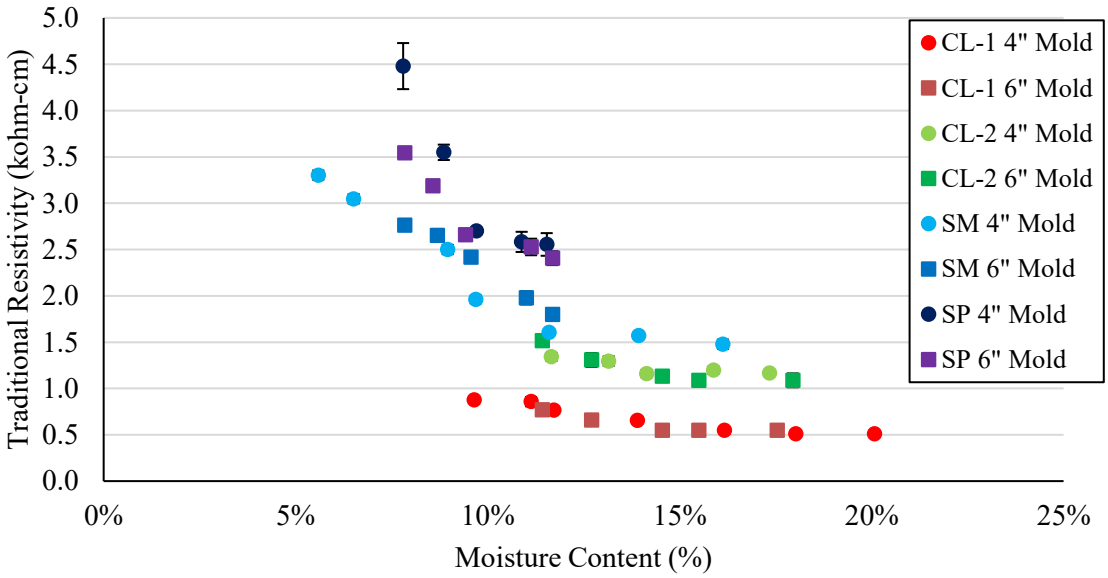


**Figure 45: Comparison of Resistivity Measurements from Different Specimen Sizes**

### 4.2.2 Large-Scale Specimens

The variations of the traditional resistivity with moisture content for the three geomaterials are summarized in Figure 46. The moisture measurements were repeated at five points to document the variability of the results. The measurements made at 12 in. and 24 in. heights yielded similar results. The measurements were also repeatable as judged by the lengths of the error bars representing ±1 standard deviation.

The normalized resistivity of the measurements conducted in the large-scale specimens with moisture content is presented in Figure 47. Due to the similarity of the results from the 12-in. and 24-in. heights, the averages of the two measurements are shown in the figure. The solid black curve is the trendline from the Proctor specimens' measurements. (Figure 44). That trendline represents the lab data quite well, indicating that the lab and large-scale specimen results follow the same trends as long as an appropriate calibration process is implemented.

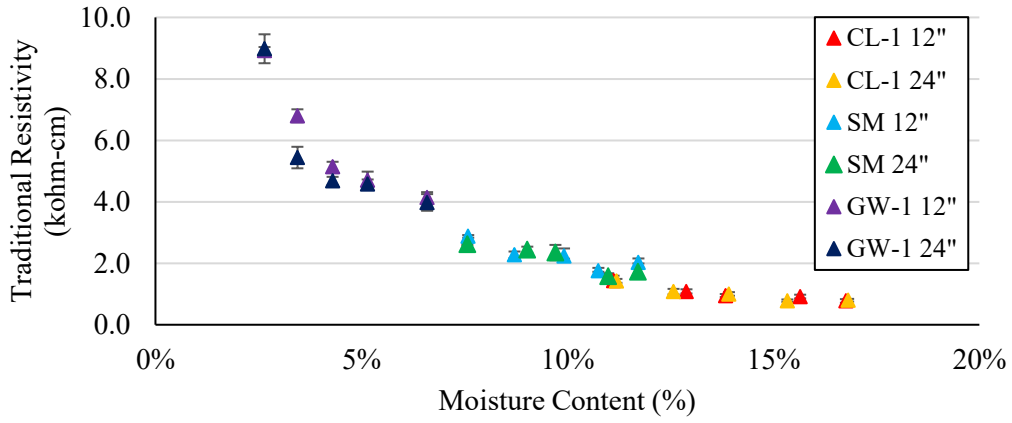


**Figure 46: Traditional Resistivity Data of CL-1, SM, and GW-1 in Large Scale Specimens**

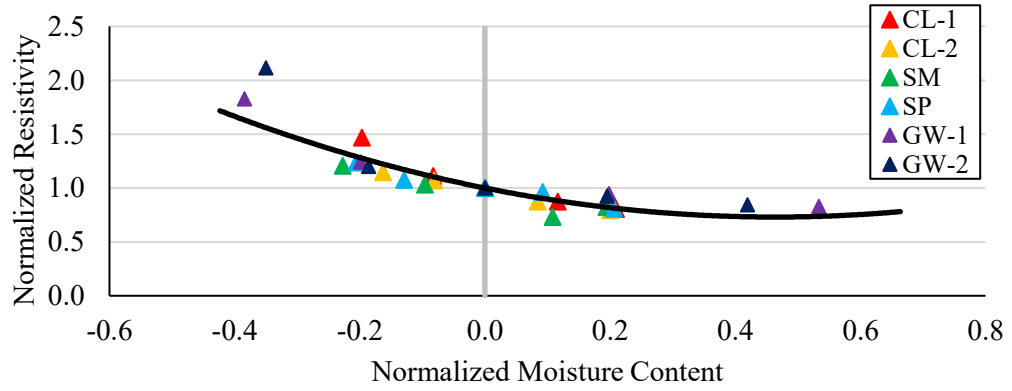


**Figure 47: Normalized Traditional Resistivity of Soils in Large-Scale Specimens**

To emphasize the importance of proper calibration, the measured resistivities for the six materials are shown in Figure 48. A systematic difference between the measurements made on the Proctor specimens and large-scale specimens can be observed that can be attributed to the differences in compaction method and energy, among several other factors that were not considered in the adjustment factors. Nevertheless, the rate of change in resistivity with moisture content is the same between the laboratory and field data.

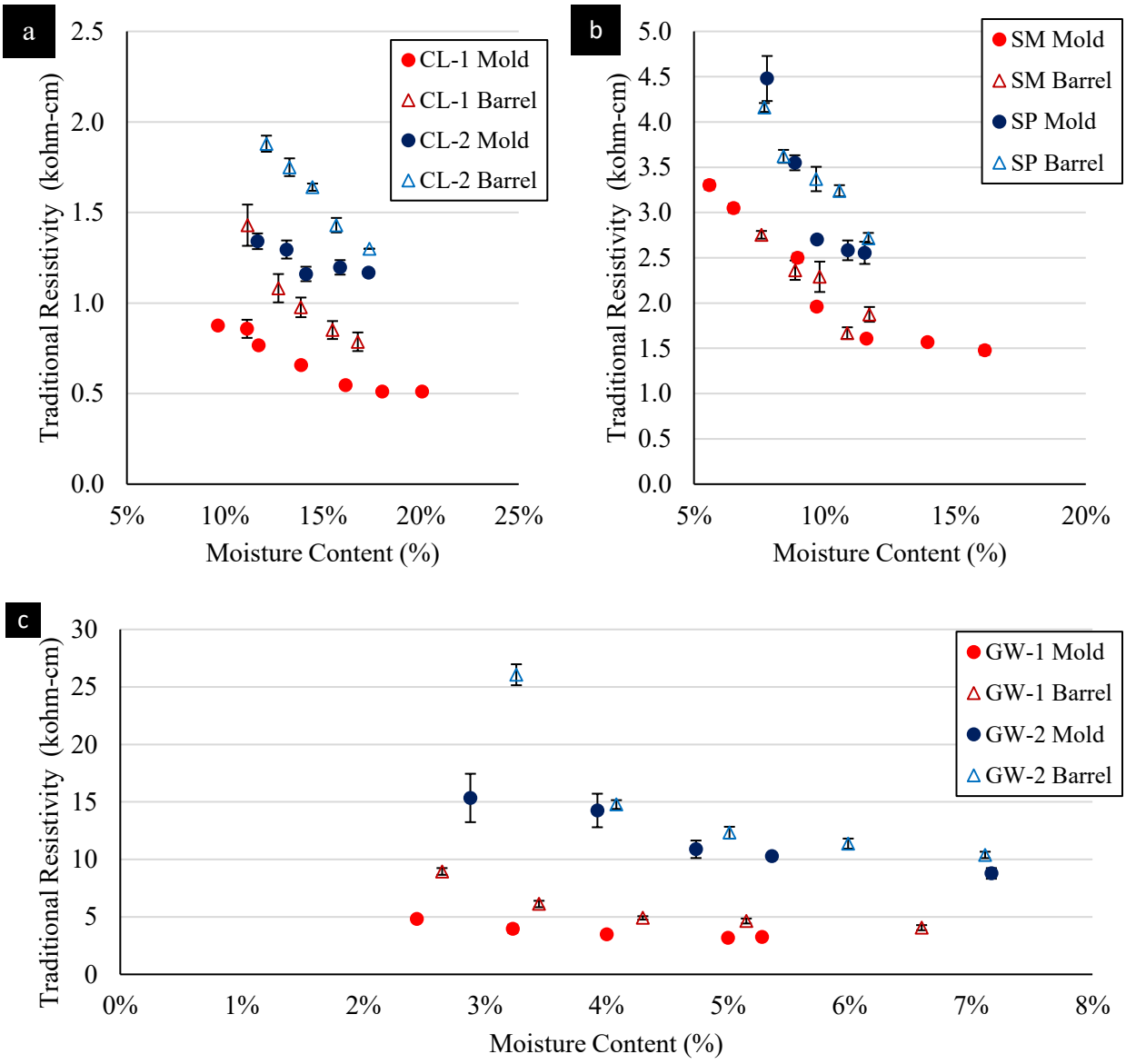


**Figure 48: Comparison of TR of Lab and Large-Scale Specimens (a) Clays (b) Sands (c) Gravels**

## 4.3 Complex Resistivity

Figure 49 displays CR readings for CL-2 specimens in the cradle at four different moisture contents, seven frequencies labeled on the abscissa, and ten current levels at each frequency. The error bars represent one standard deviation estimation based on at least ten measurements at each current and include an uncertainty when the measured current deviates from the design current. Lower frequencies and low currents show high variation and low precision where electrode interactions are significant. The upgraded version 8 electronics were used for these measurements. About 20 current and voltage measurements per frequency and multiple currents are saved. The averages and standard deviations of these currents and voltages are then read, computed, and estimated in post-processing software. This

step also calculates the ratio of the real and imaginary electrode voltages to the real and imaginary driving current. The software needs a calibration factor for resistivity magnitude and phase, followed by electrode geometry and sample shape calibration factors. The errors indicated for resistivity and phase are computed using randomized perturbations to observed voltages and currents due to the nonlinearity and dependencies in the computation. When fixed ideal resistors are connected to the cradle or array electrodes, this same measurement procedure provides calibration constants.

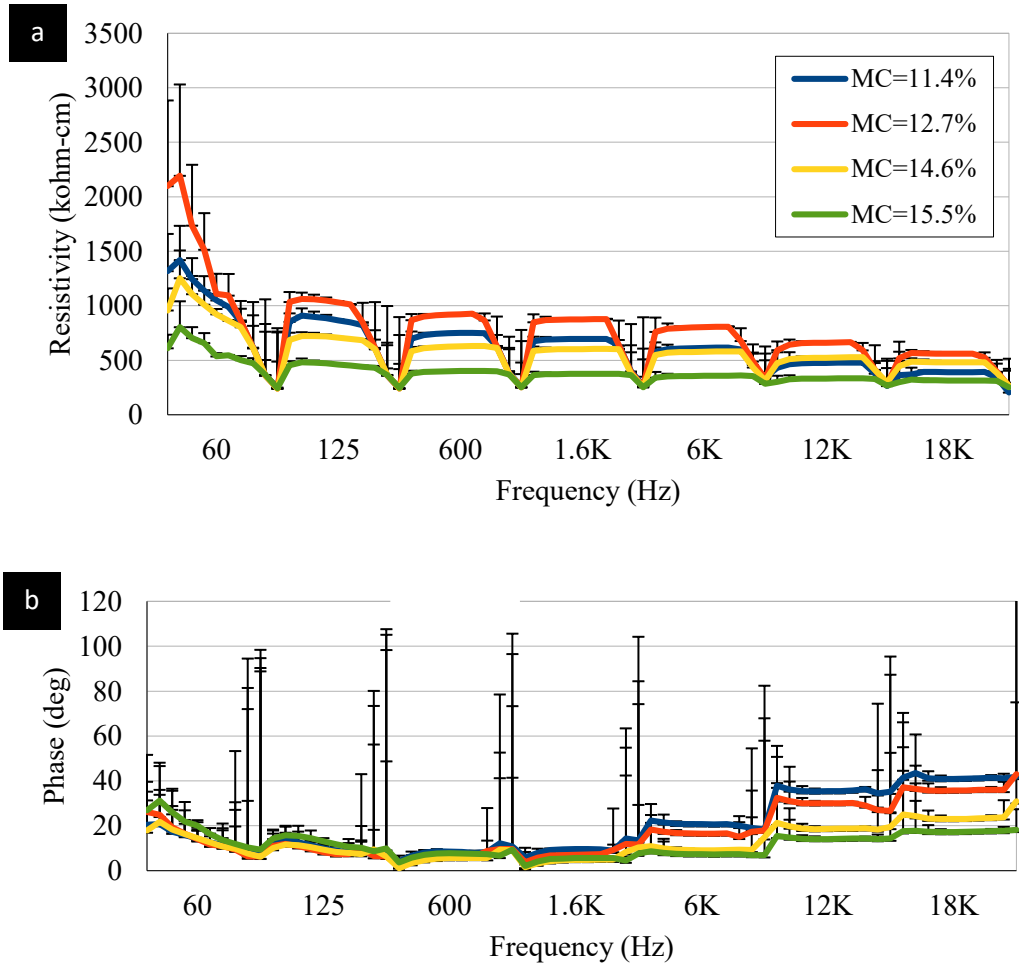


**Figure 49: Sample Measurement of CL-2 of (a) CR and (b) Phase at Several Moisture Contents**

The following four major features in the measurements are apparent in Figure 49:

1. Although electrode polarization dominates measurements at low frequencies (60, 120 Hz: TR measurement domain), they exhibit consistent moisture and current dependency patterns. This electrode polarization decreases (as manifested by higher current density) as a Wenner array with a reduced contact area is used.
2. Despite improvement in the measurement errors from version 6 to version 8 of the CR device; errors are still present in the first few currents of each of the higher frequency measurements.

3. The fraction of ions polarizing at the air-water interface, which rises as moisture content decreases, is measured by the phase change with moisture and frequency. At 600 Hz and above frequencies, resistivity and phase values exhibit consistent and substantial variations in moisture content. In general, the resistivity decreases with frequency as moisture content increases, reflecting that ions in the fluid move farther at lower frequencies while the potential water path increases. As the moisture content of the same sample varies, phase value should be able to distinguish saturation variations more accurately than resistivity. It needs to be clarified how resistivity/phase will alter when the texture changes during compaction.
4. The blue curve, corresponding to the lowest moisture content, which is expected to have the highest resistivity and highest phase change, deviates from that expected resistivity pattern. Based on published data on controlled samples, the phase shifts in this specimen are less than anticipated.

Comparing the full spectrum CR tests for samples of the GW-2 and CL-2, with high uncertainty values eliminated, in Figure 50 demonstrates how difficult it is to simplify the process. As a first attempt, a low-frequency CR estimate along with the associated uncertainty, and the slopes of normalized CR with frequency and current were utilized to summarize each resistivity and phase curve's characteristics. This comprehensive technique may be helpful in the laboratory or while making static diagnoses in the field; however, a more straightforward measurement and analysis are needed for field measurement in a continuous mode.

A composite plot of the CL-1, SM, and GW-1 measurements of resistivity and phase slope with frequency is shown in Figure 51 for comparison with the TR measurements in Section 4.2. Figure 52a shows the normalized complex resistivity and Figure 52b shows the normalized phase values. The CR measurements exhibit more variation, but the curve shapes are consistent with the moisture-resistivity relations previously discussed. Despite more variability in the CR measurements, there is a correlation between resistivity and phase slope within each material type at a particular moisture level, which is consistent with the expectation that gradation changes in compaction are as crucial as moisture level changes to the CR measurements.

## 4.4 Repeatability

Five replicate specimens were made at three different moisture contents per material using the CL-1, SM, and GW-1 geomaterials to assess the repeatability of the moisture tests. The three moisture contents comprised OMC, OMC±20%×OMC for the clay, and OMC±2% for the sand and gravel. Table 5 shows the variability of the dielectric and resistivity measurements. The dielectric constant measurements showed a coefficient of variation between 10% and 32%, with a typical variability of about 20%. The coefficients of variation of the measurements with the traditional resistivity were 8.5% or less for all the specimens tested. Given the level of variability of the dielectric measurements, further analysis was not carried out in this report. The results are, however, documented in Appendix A. The coefficients of variation of the complex resistivity and phase change are shown at the 600 Hz frequency. The typical variability of the complex resistivity was under 20% but could range to a maximum of 26%. The phase changes showed a slightly higher variability with a maximum coefficient of variation of 28%.

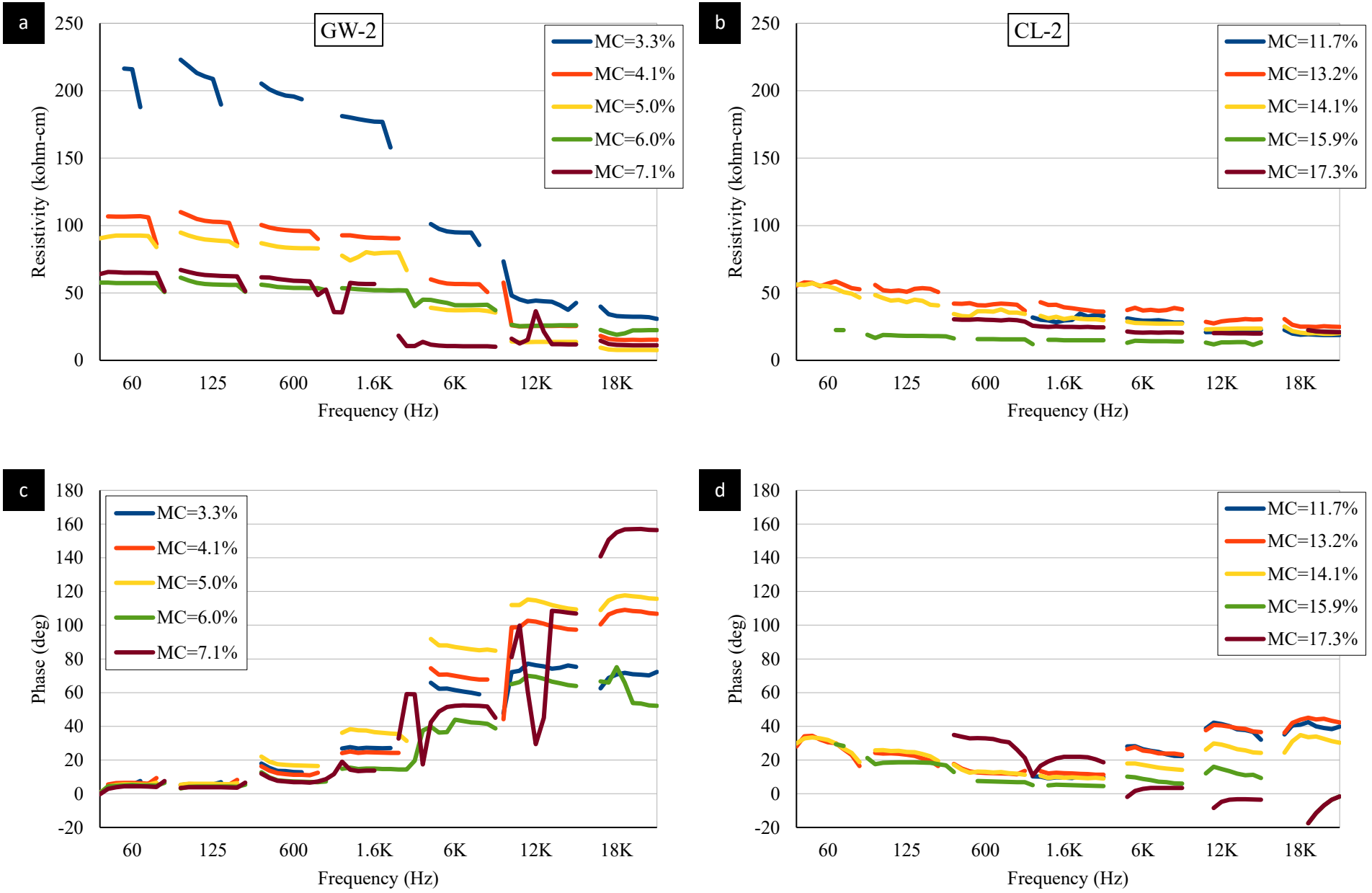


**Figure 50: Large Scale Full Spectrum Tests of GW-2 and CL-2 of CR and Phase at Several Moisture Contents (MCs)**

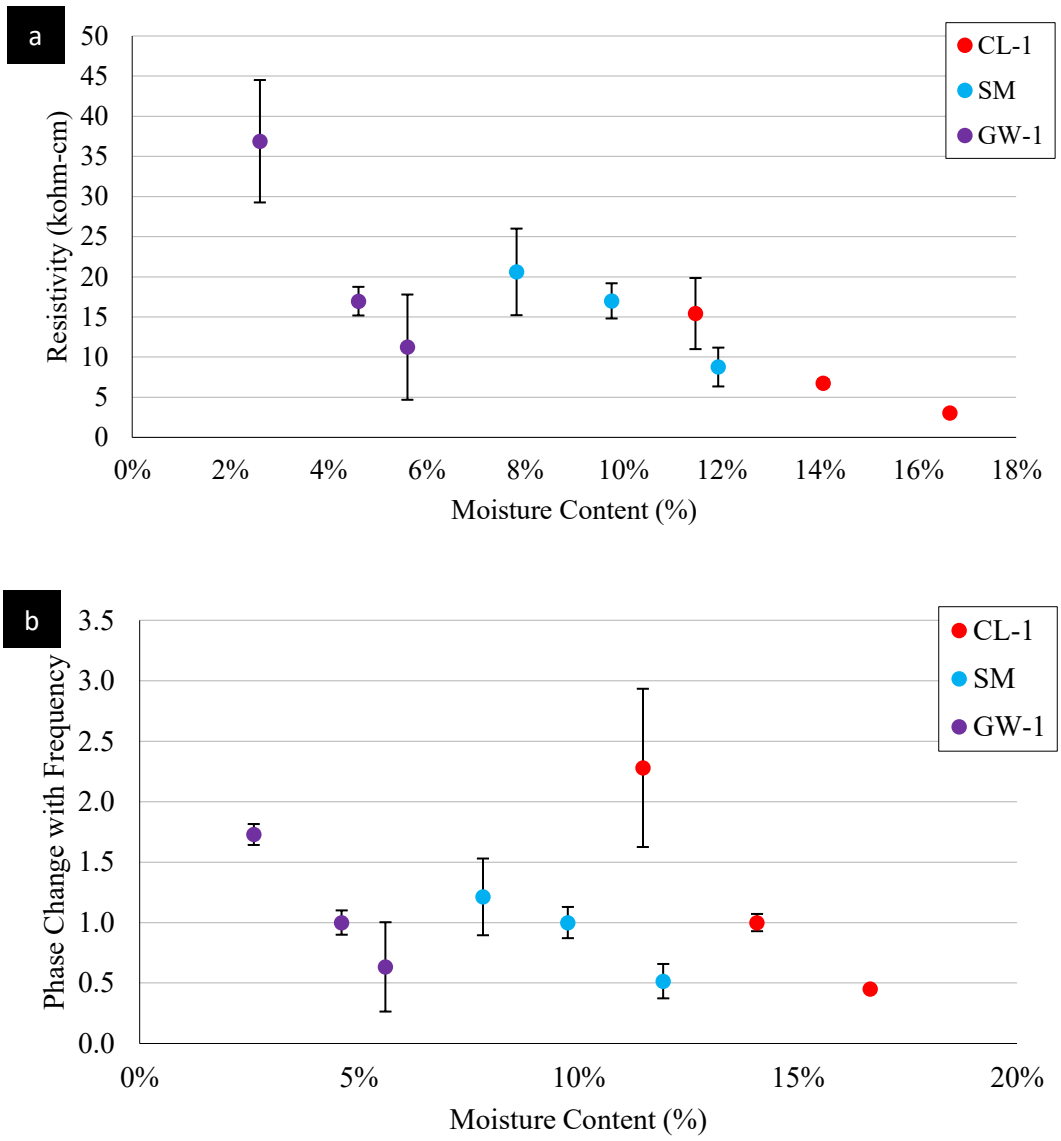


**Figure 51: CR Data of CL-1, SM, and GW-1 (a) Resistivity (b) Phase-Change**

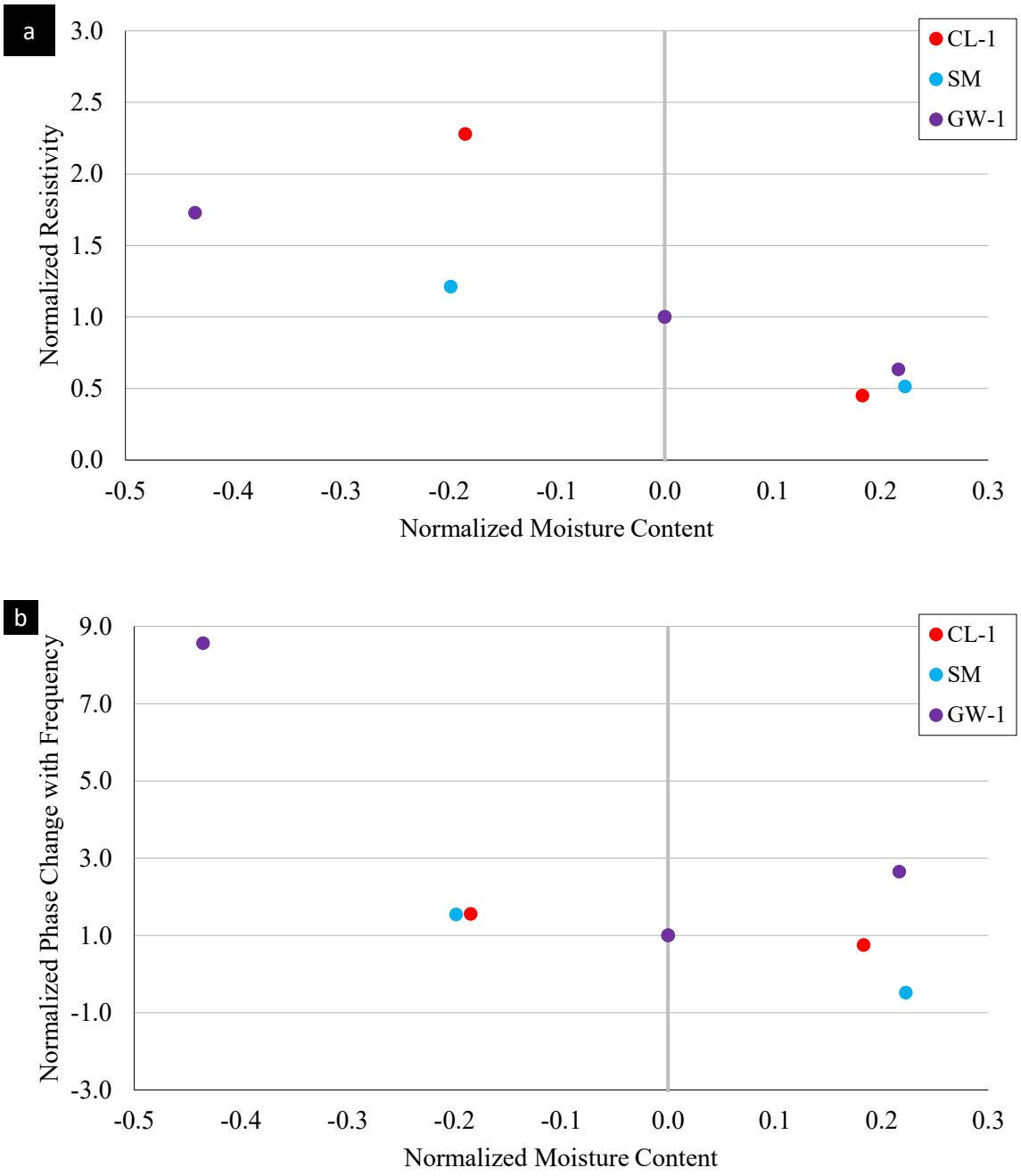


**Figure 52: Normalized CR Data of CL-1, SM, and GW-1 (a) Resistivity (b) Phase-Change**

**Table 6: Coefficient of Variation of Replicate Specimens**

| Measurement | Soil | Dry | | OMC | | Wet | |
|---|---|---|---|---|---|---|---|
| | | Average | Max | Average | Max | Average | Max |
| Dielectric Constant | CL-1 | 19.7 | 21.6 | 20.7 | 32.3 | 13.7 | 18.2 |
| | SM | 9.8 | 11.7 | 14.1 | 27.0 | 10.6 | 18.0 |
| | GW-1 | 13.4 | 22.0 | 26.0 | 32.1 | 20.4 | 28.0 |
| Traditional Resistivity | CL-1 | 3.2 | 4.9 | 4.7 | 7.0 | 3.7 | 5.0 |
| | SM | 2.4 | 4.3 | 4.2 | 7.7 | 5.0 | 6.0 |
| | GW-1 | 6.0 | 7.3 | 4.9 | 8.5 | 5.1 | 5.8 |
| Complex Resistivity | CL-1 | 17.8 | 20.5 | 13.9 | 15.5 | 15.5 | 15.8 |
| | SM | 15.9 | 16.3 | 11.4 | 11.9 | 7.8 | 8.6 |
| | GW-1 | 14.4 | 15.9 | 9.4 | 13.2 | 6.0 | 6.2 |
| Complex Phase Change | CL-1 | 8.6 | 11.9 | 12.0 | 13.4 | 22.0 | 25.7 |
| | SM | 14.2 | 16.9 | 13.3 | 14.8 | 17.0 | 18.7 |
| | GW-1 | 23.8 | 28.1 | 25.1 | 28.2 | 13.7 | 16.6 |

### 4.5 Seismic Modulus

The variations of the seismic modulus with moisture content for the fine-grained and sandy geomaterials are presented in Figure 53. There was difficulty obtaining the seismic moduli of the gravelly specimens due to the length-to-diameter ratios of the specimens. For all geomaterials demonstrated, the modulus decreases significantly with an increase in moisture content. The two CL soils exhibited significantly different moduli, despite demonstrating similar index properties and MDDs. This pattern demonstrates the importance of modulus measurements.

## 4.6 Unconfined Compressive Strength

The variations of the unconfined compressive strength with moisture content for each of the six geomaterials are demonstrated in Figure 54. Again, similar clays demonstrate different strengths, as was the case for the seismic modulus measurements.

## 4.7 Lightweight Deflectometer Moduli

The variations of the LWD modulus with moisture content for the six geomaterials using the special setup recommended for determining the target modulus are shown in Figure 55. The moduli of the sands tended to decrease as moisture increased. The height at which the large-scale specimens were tested played a factor in the measured moduli. The LWD moduli of both clays and the SP geomaterial followed similar patterns between the laboratory and large-scale specimens. The modulus of the SM had high variability at different heights. The modulus of the barrels for the gravels minimally changed or increased slightly.

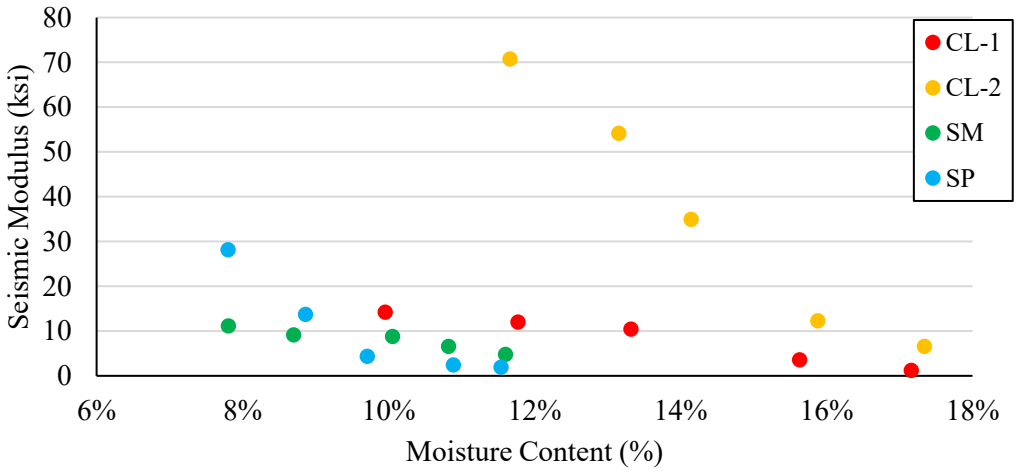


**Figure 53: Seismic Modulus Data of Geomaterials**

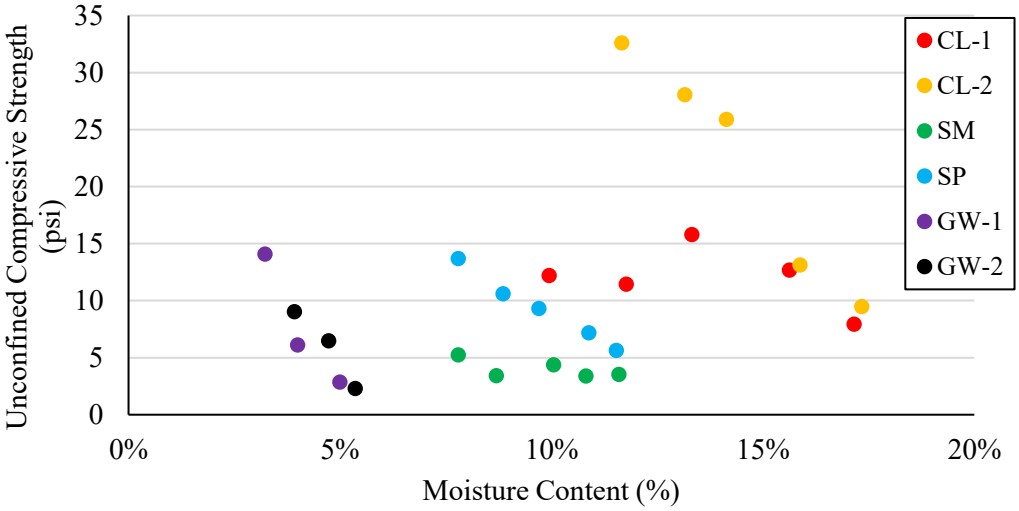


**Figure 54: Unconfined Compressive Strengths of Geomaterials**

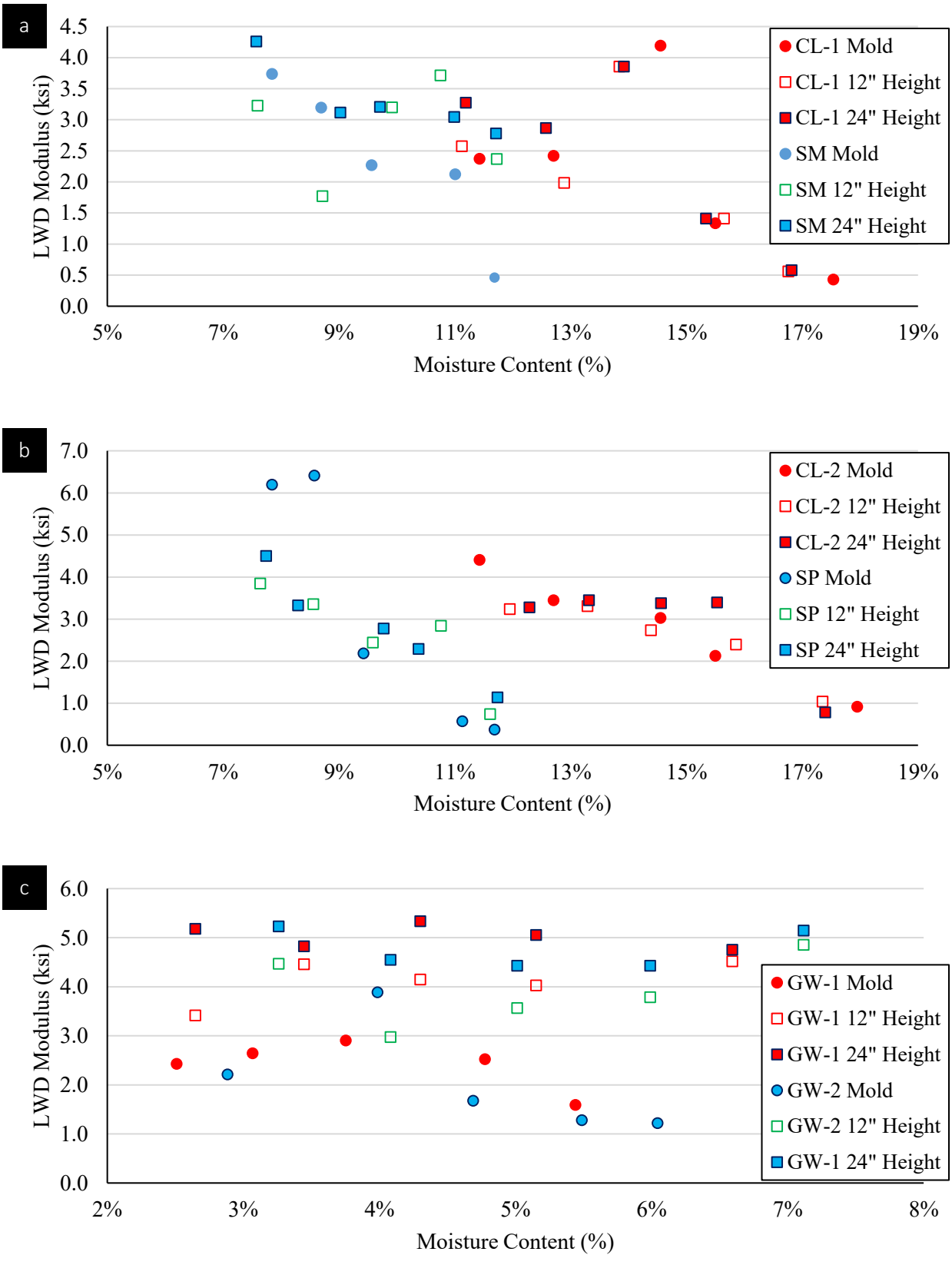


**Figure 55: Laboratory-Measured Lightweight Deflectometer Moduli of Geomaterials**

# Chapter 5: Field Evaluation

## 5.1 Demonstration Of Field Prototype

### 5.1.1 Prototype Devices

Two sets of tests were carried out on each specimen, using a Wenner Array (WA), Figure 56, and a rolling equatorial array (REA), Figure 57. The WA was used for the static complex resistivity measurements, and the REA was used for the rolling complex resistivity, as explained in the testing program section.

**Figure 56: Wenner Array Prototype**

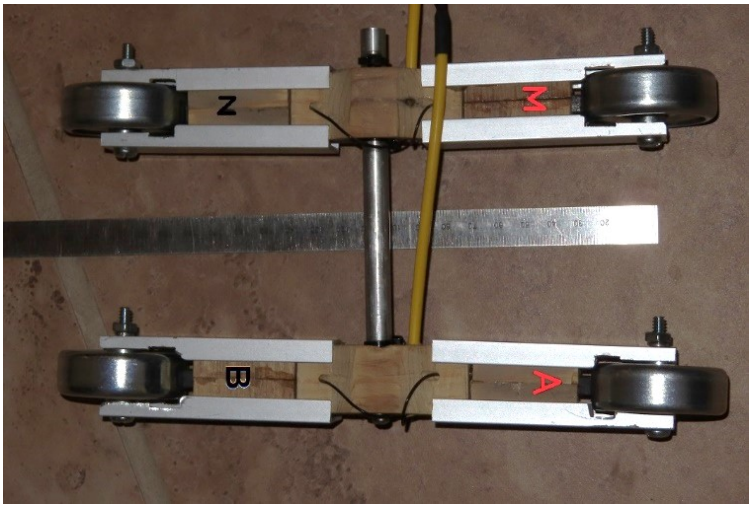


**Figure 57: First Rolling Array used during Initial Field Demonstration**

Testing was conducted at the MnROAD test track pavement facility in Otsego, Minnesota, in June 2022. Two cells, 2228 and 2229, consisted of a natural clay subgrade, sandy subbase, and gravely unbound base, each measuring 25 ft (7.6 m) wide by 225 ft (70 m) in length. The subbase and base contained recycled concrete aggregate (RCA) and recycled asphalt pavement (RAP), conforming to MnDOT standards. The subbase thickness was nominally 12 in. (300 mm) and the base 9.5 in. (240 mm) in both

cells. A moisture-wicking geotextile was placed between the subgrade and subbase of Cell 2229. This testing corresponded with the intelligent compaction analysis technical report, *Evaluation of Level 3-4 Intelligent Compaction Measurement Values (ICMV) for Soils Subgrade and Aggregate Subbase Compaction* (Chang et al., 2023). The same testing grid was used in the two studies.

The testing grid of Cells 2228 and 2229 followed the scheme of the ICMV mapping. For mapping, rectangular sublots around grid points defined by the geo-referenced spot test locations were established following the IC test layout. The grid pattern for the spot testing used four separate lanes, as shown in Figure 58, defined as A, B, C, and D. The spot tests were spaced approximately 6 ft (1.8 m) by 25 ft (7.6 m) apart. The static WA measurements were taken at the spot tests (shown in red), and the moving REA measurements were taken between Station 175 ft. and 200 ft. of Lines A and D.

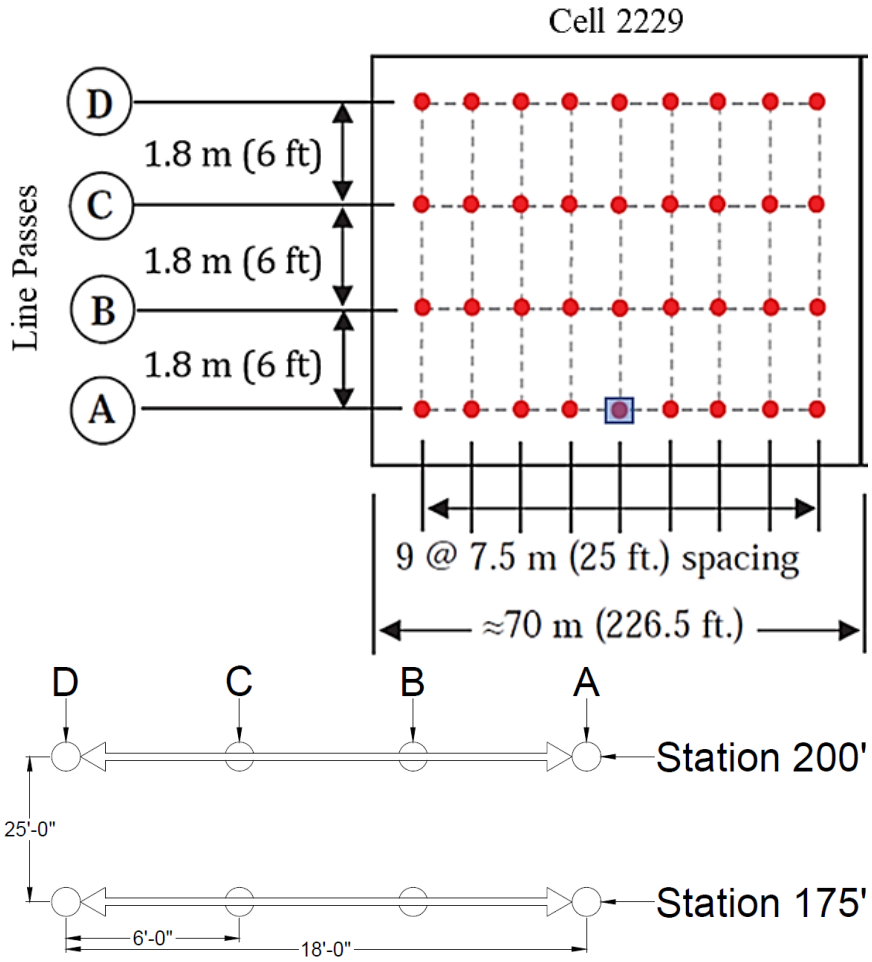


**Figure 58: Spot Test Layout of Cell 2229 and Rolling Array Layout between Station 175 and 200**

After the compaction of each layer was completed, the research team conducted the WA and REA measurements as described in the testing program. As shown in Figure 59, the WA was fitted with a PVC pipe and handle to help the research team conduct the measurements more conveniently. The REA (Figure 60) was also fitted with a handle to accelerate the measurements. Testing was conducted at a walking speed. The WA used the full range of frequencies from 125 Hz to 19.2 kHz and currents from 12

µA to 1300 µA, while the REA used frequencies of 630 Hz and 5.8 kHz and currents 160 µA and 510 µA. For analysis and results in this report, frequencies 630 Hz and 5.8 kHz were used. This setup allowed verification that complex resistivity with the WA was stable over a full range of currents, eliminating one possible contribution to uncertainty in the dynamic measurement.

Figure 61 shows the variation of total unit weight with moisture content for Cell 2229 from the nuclear density gauge. The poor correlation indicates significant variability in the compaction of the subbase.

Figure 62 shows the variations of the CR with moisture content and total unit weight in Cell 2229. The resistivities measured at 630 Hz are uniformly higher than those measured at 5.8 kHz, while the phase lags at 630 Hz are lower than those at 5.8 kHz measurements. All the CR measurements are generally independent of the moisture content and total unit weight. The only weak visual correlation is a lc ,r bound of the phase measurement at 5.8 kHz as a function of moisture content.


**Figure 59: Wenner Array Field Evaluation**


**Figure 60: Rolling Equatorial Array Field Evaluation**

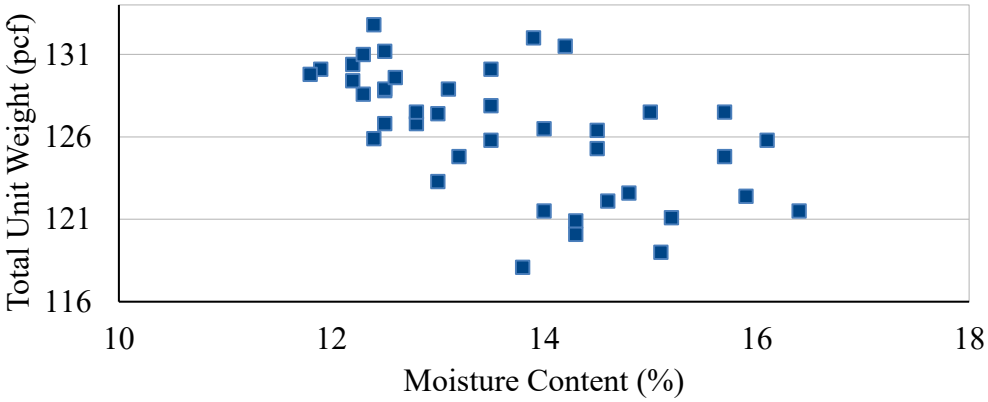


**Figure 61: Variation in Total Unit Weight with Moisture Content along Cell 2229**

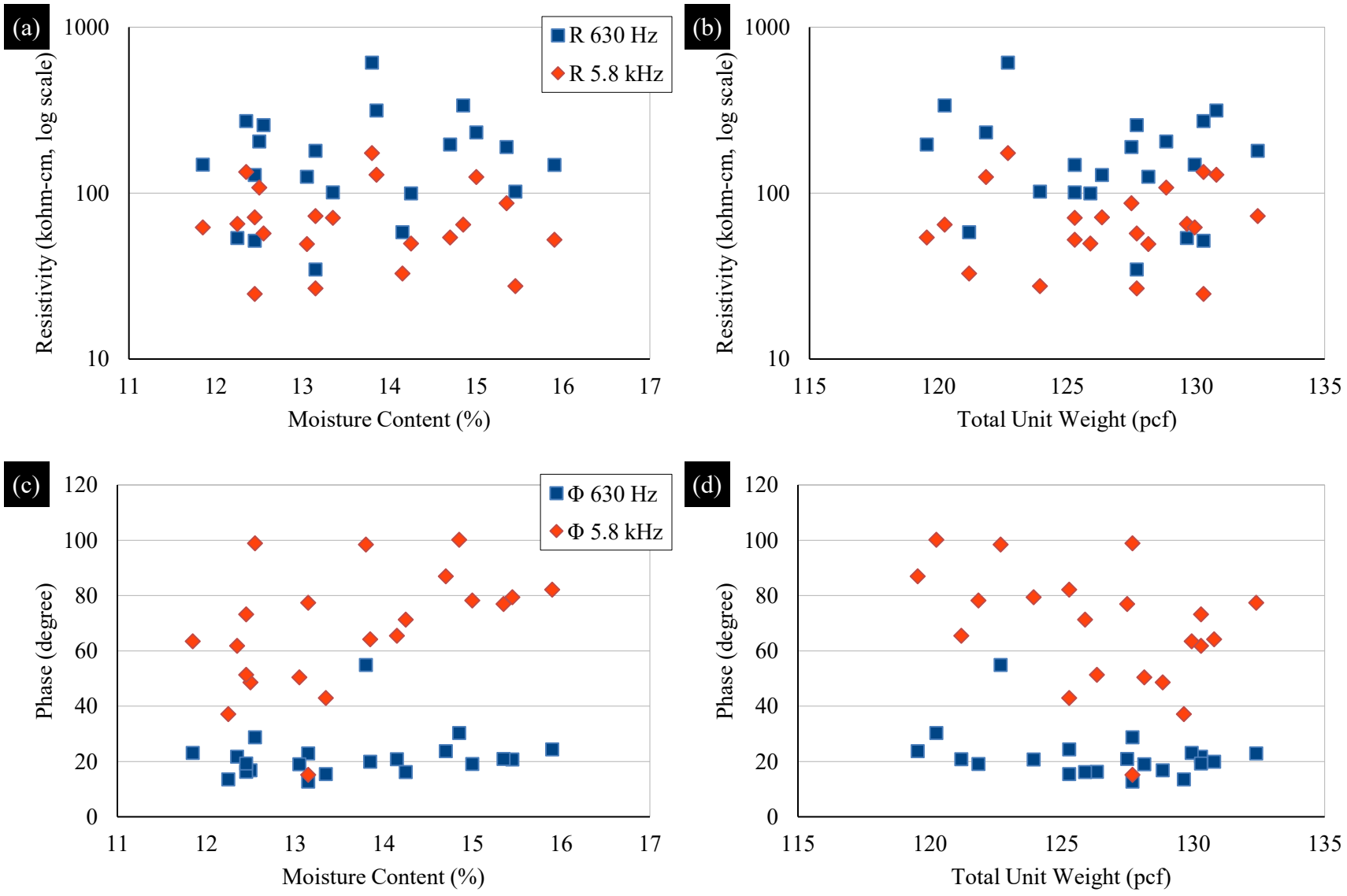


**Figure 62: Variations of (a, b) Resistivity and (c, d) Phase lag to Moisture Content and Total Unit Weight of Cell 2229**

Figure 63 again confirms the independence of the CR measurements to the moisture content and total unit weight. Averages of the four lines A-D do not improve the relations, indicating the variation is not a matter of high random noise level in the measurement of correlated variables.

Figure 64 shows the raw measured voltage from the current monitor channels (solid lines) and the designed injected current (dashed lines) between Lines A and D at 175 ft of the subgrade. The measurements were conducted at 6 samples/second, giving a spatial sampling on the order of 200-300 samples in 25 ft between Lines A and D. Measurements were made in two directions (from A to D and from D to A) for repeatability. The REA had far greater difficulty injecting current, both static at the start of a line and while moving. At each of the two operational frequencies, the array was rolled forwards and backward both at the low and high currents. For the low-frequency measurements, the low-current injection only approaches the design value on about 30% of the line and fails to reach the design value for the high-current measurements at all. The low-current injection attains the design value for the high-frequency measurements and shows a marginal regulation loss at the high-current injection.

Complex resistivities, estimated as the ratio of the measured electrode voltage and the measured current, are estimated using the measured current injection in Figure 64, even though the current is not well regulated. Subsequent profile resistivity calculations are retained as long as the current level exceeds 50 times the measurement precision (precision is erratic), and the voltage at receiving electrodes was below the instrumentation saturation level. The precision of frequency 5.8 kHz was about 10% for the current 510 μA and 20% for 160 μA of the Wenner. Without current regulation on the REA, it is not easily evaluated.

Figures 65 and 66 show the computed resistivities and phase lags from the Wenner and REA along two lateral lines of 175 ft and 200 ft measured from Line A to Line D. The time measurements were converted to distance with some approximations due to the variation in walking speed and the slight differences in the forward and backward directions. Only the low current (160 μA) measurements were used due to the greater unreliability of the high current setting.

Figures 65 and 66 show that the Wenner resistivities and phases are similar in value to the 5.8 kHz REA values. The 630 Hz REA resistivity values are much higher than the Wenner measurements and show highly variable phases. There is no reason to estimate differentials between the two frequencies given these results that differ from homogeneity in the lab-scale measurements. In general, there is no strong correlation in resistivity trends between Wenner and REA.

Figures 67 and 68 show the REA measurements connecting the end points of the profiles in Figures 65 and 66. The left-hand side of Figures 66 and 67 show the resistivity and phase measurements at the 160 μA current level, while the right-hand column shows only the 5.8 kHz measurement at 510 μA. The resistivity and phase values at 630 Hz are again much larger than those at 5.8 kHz and show similar degrees of non-repeatability.

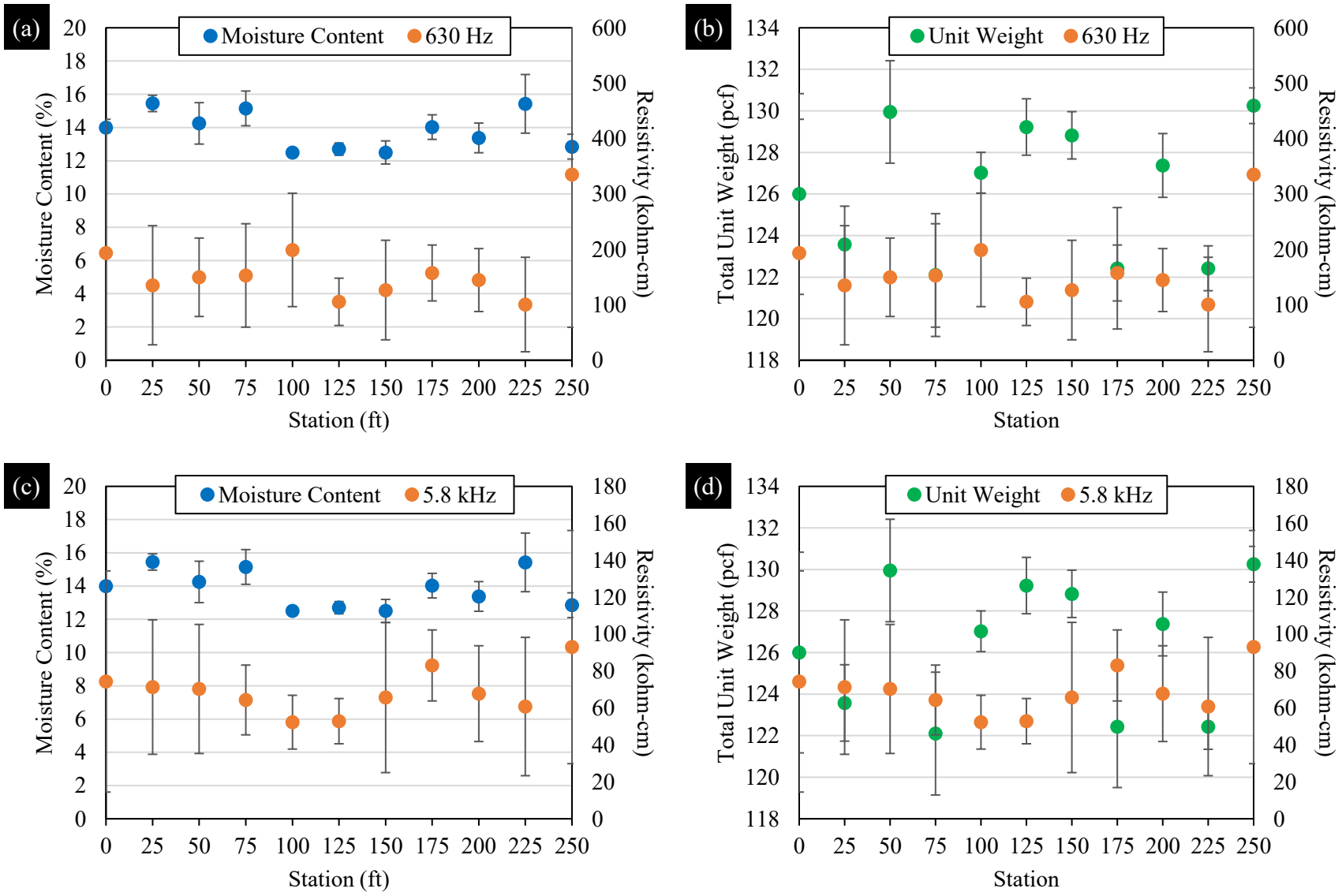


**Figure 63: Comparison of (a, c) Moisture Content and (b, d) Total Unit Weight with Wenner Array Resistivity Averaged Over Lines A-D**

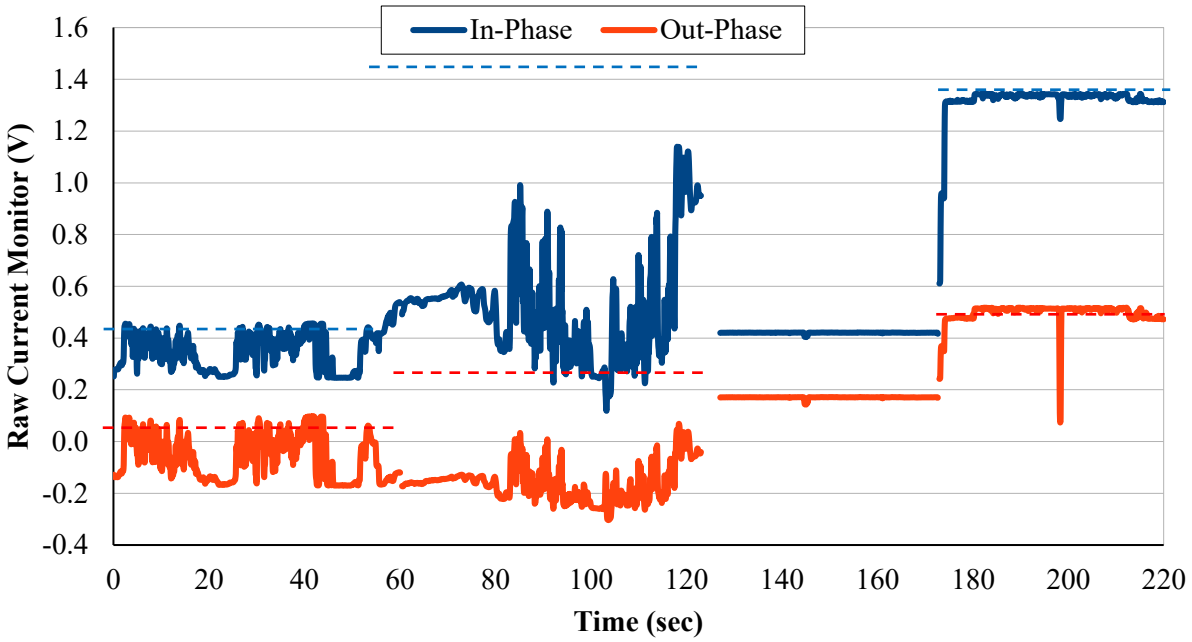


Figure 64: Typical measurements with REA from Line A to Line D at 175 ft

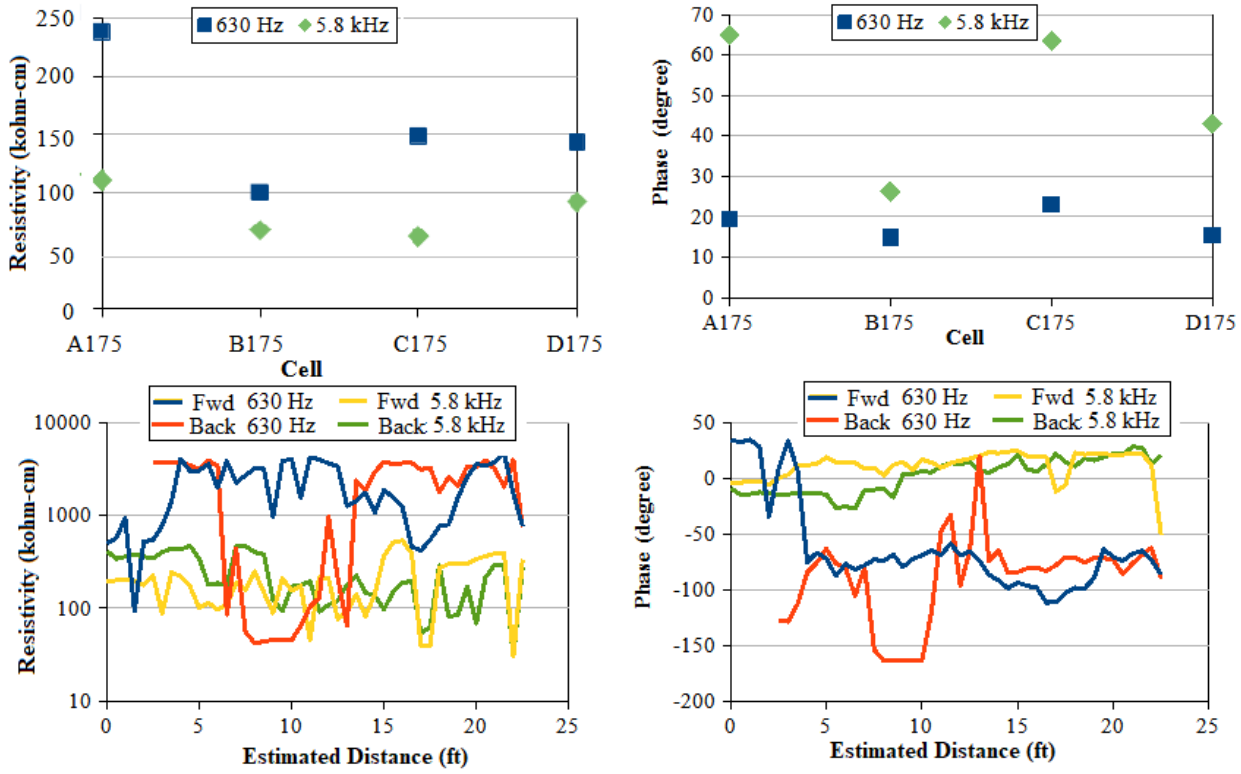


Figure 65: Comparison of Wenner and Rolling Array results along Line A and Line D, Station 175 of Cell 2229

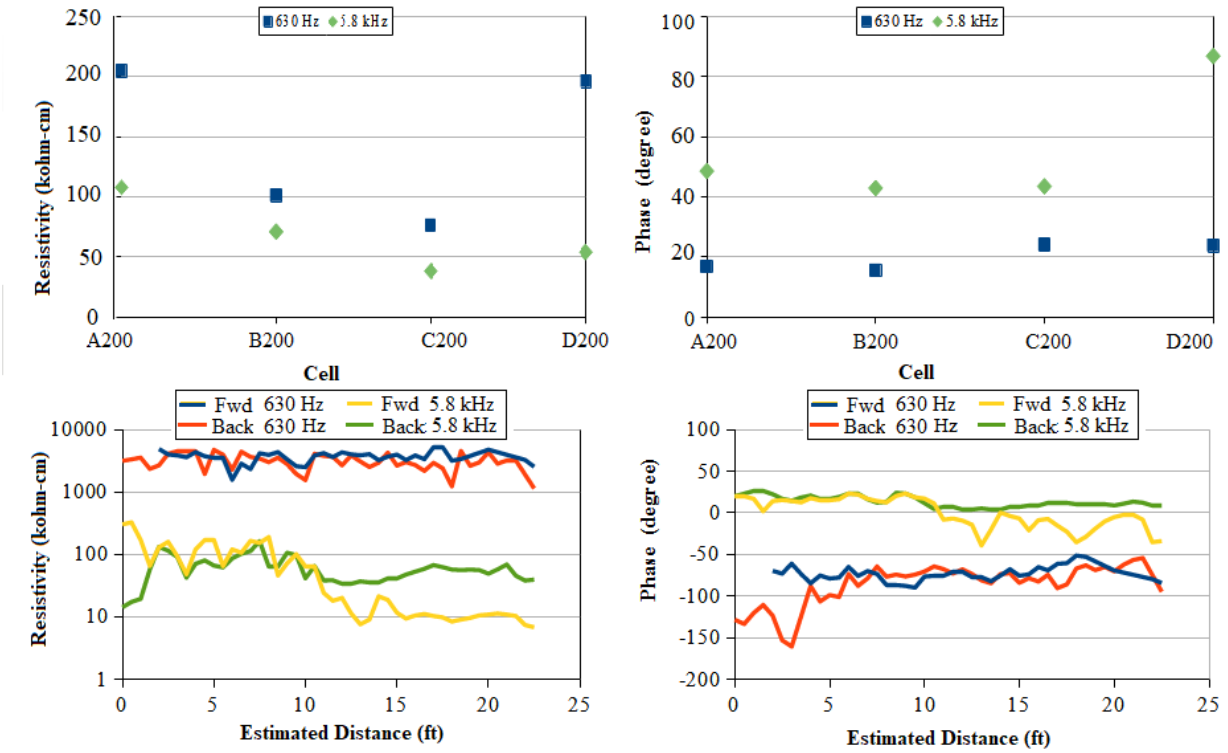


**Figure 66: Comparison of Wenner and rolling array results along Line A and Line D, Station 200 of Cell 2229**

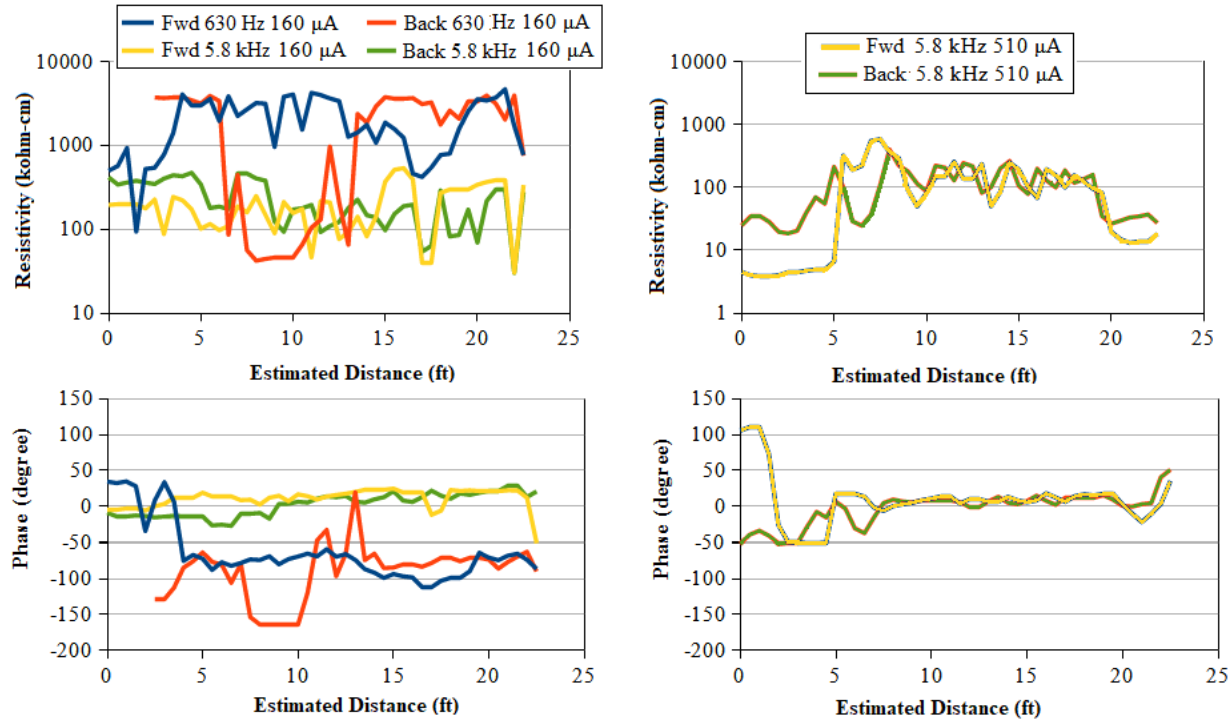


**Figure 67: Rolling Equatorial Array Run between Station A175 to D175 with Frequency 630 Hz and 5.8kHz, Current 160 and 510 µA. Measurements were only possible at 510 µA at the higher frequency.**

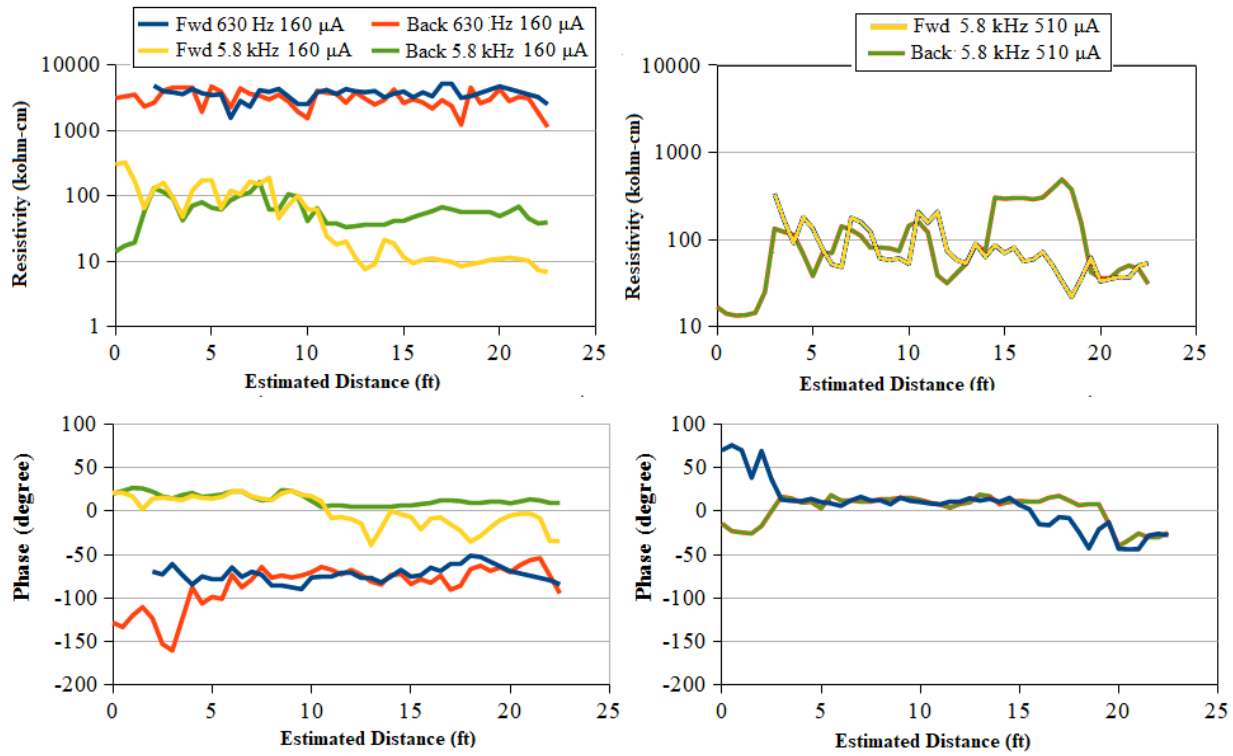


**Figure 68: Rolling Equatorial Array Run Between Station A200 to D200 with Frequency 125 and 5.8k Hz, Current 160 and 510 µA**

The composition, larger scale, and structural construction of Cell 2229 introduce important complexity into the attempt to monitor moisture content using electrical techniques such as dielectric permittivity, conventional resistivity, or complex resistivity (CR). This study's progression from simple mixtures on a small scale to more complex mixtures at larger scales illustrates the relevant variables.

The initial expectation that CR would be sensitive to pore-scale polarization effects in the kHz frequency range was verified in laboratory tests on small-diameter specimens. There was a progression from clays with higher-frequency polarization phenomena that progressed to lower frequency as aggregate size increased. As the scale of the measurement increased to the larger diameter specimens, and 24-in barrels samples, the pore-scale polarization was still evident, but there was a consistent trend in larger polarization components at lower frequencies. This can be attributed to both the sample size and increased difficulty in preparing uniform moisture distribution in larger samples.

Material property variation was observed in the laboratory studies. The CL samples in the early small-scale tests had more erratic responses that were attributed to weaknesses in our sample preparation and lab procedures. The carbonate aggregate showed unstable changes in polarization consistent with precipitation/dissolution reactions and higher resistivities associated with the much lower surface charge density of their surfaces.

The overwhelming influence of the RAP on property measurements became apparent in the field experiment. We interpreted our initial failure to make viable measurements as equipment failure until

the laboratory moisture contents documented the high asphalt content, and differences between WA and REA isolated functional performance issues to the REA. This led to the revised field implementation; laboratory-scale studies on fine-grained materials with the revised REA geometry documented next.

## 5.2 Revised Field Implementation

Following a meeting with the Technical Advisory Panel (TAP), the field implementation was revised to focus on testing continuous resistivity/polarization measurements in fine-grained aggregates (clay and sand) while de-emphasizing measurements on the coarse-grained aggregate base courses. These tests were revised to document making continuous rolling equatorial CR electrode measurements, referenced to static Wenner array CR measurements, on controlled sand, clay, and a sand/clay mixture in the large-scale laboratory specimens.

The Two clayey and the two sandy geomaterials defined in Table 2 were used in this stage of the study. The soil samples were prepared in 33 in. x 21 in. containers to a depth of 4 in. to be consistent with the smallest specimen diameter used by the proctor specimens and keep material usage reasonable, as shown in Figure 69. Specimens were prepared at three moisture contents: OMC, OMC±2% for the two sands, and OMC±OMC×20% for the two clay soils. The soils were mixed by hand and by volume of 2-in. lifts at a total height of 4 in.


**Figure 69: Typical Specimen Prepared for Testing**

Tests with the WA and REA followed the following procedures (see Figure 70):

1. WA at five locations down the centerline of the tub with the array perpendicular to the centerline, using the same seven frequencies and nine current levels that were used to compare with the laboratory specimens and to reference the REA measurements.
2. REA down the centerline of the specimen with the following patterns:
    a. Transit front to back in 3 sec (denoted as F-B 3s), wait one sec, and transit to the front in 3 sec. Repeat at two frequencies and three current levels as discussed below.

b. Transit back to front in 3 sec (denoted as B-F 3s), wait one sec, and transit to back in 3 sec. Repeat at two frequencies and three currents.
c. Repeat steps 2a and 2b using a 10-sec transit time (denoted as F-B 10s and B-F 10s).

REA data was collected on electrode voltage and current at 14 samples/sec. Every physical location on the centerline was measured eight times at each current and frequency with two static measurements at each line end.

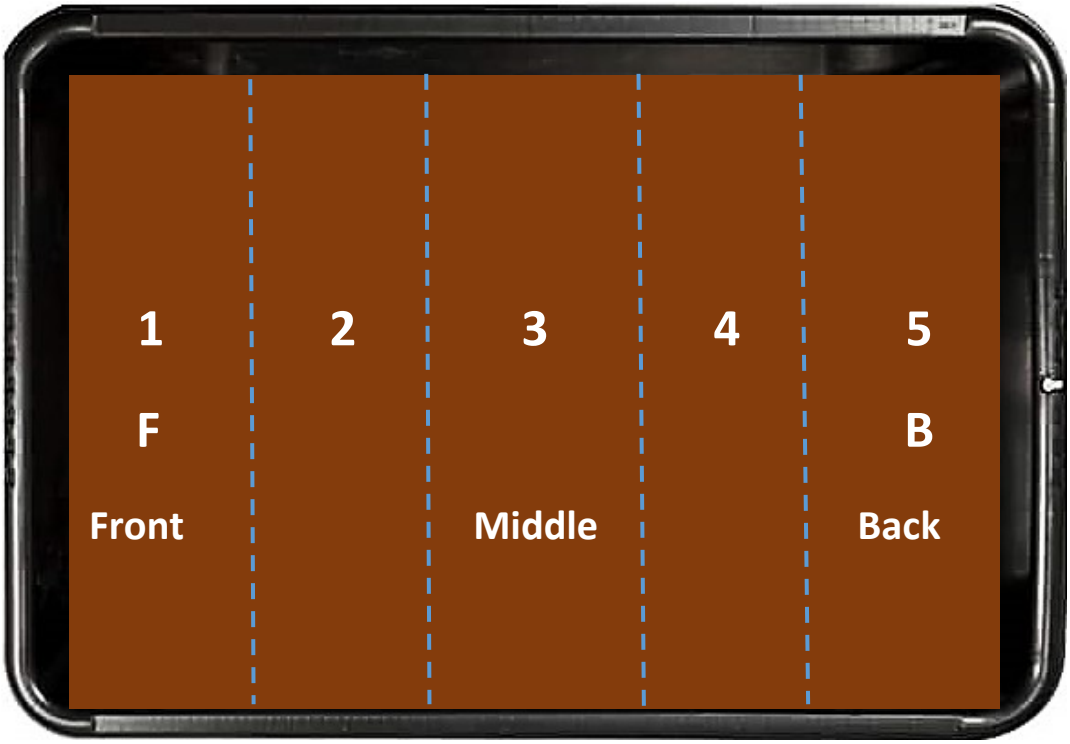


**Figure 70: Schematic of Test Configuration on each Specimen**

For each specimen, the REA system was rolled forward and back down the centerline of the long axis of the container at two operating frequencies of 630 Hz and 5.8 kHz. The frequency of 630 Hz was selected after conducting initial laboratory measurements for the low-frequency reference point as it contained the least effects from electrode and sample scale polarization. The frequency 5.8 kHz was chosen to sample the saturation polarization signal from the larger pore sizes and as the lowest-noise, most reliable measurement at the higher frequencies on all materials. The full spectral frequency range of 60 Hz to 18.3 kHz with amperage currents of 12 μA to 1300 μA per frequency was measured with the Wenner array at five locations along the same centerline: one at each line end, one center, and two intermediates. REA measurements were extracted at 630 Hz to estimate the corresponding resistance, $R_{630}$, and phase, $\Phi_{630}$. The changes in resistivity and phase at 5.8 kHz were used to estimate the phase shift, $\Delta\Phi$ at a current level of 500 μA. This higher drive current was used as it gave reasonable noise estimates and might be more comparable to current densities in the shorter Wenner array.

Figure 71 compares the raw voltage and current signals as a function of time for two experiments with the CL-1 material at OMC+2% moisture content for two consecutive days. In Figure 71a, six sets of measurements are labeled with frequency and current settings. The left half of the graph shows measurements at 630 Hz and the right half measurements at 5.8 kHz. The direction of rolling, with the 1-second stationary period, and then rolling in the opposite direction are also labeled in Figure 71a. The yellow and green curves are the real and imaginary components of the measured current injection. The blue and red curves are the real and imaginary components of voltage measurement. Resistivity is calculated by the ratio of voltage to current, so when the current is constant, changes in voltage are proportional to changes in resistivity. The yellow/green curves' amplitudes increase as the current levels increase from 100 μA to 230 μA to 510 μA, and they are very constant, indicating reliable electrode contact and current injection. The large spikes and significant variation voltage signals were unexpected.

Within each graph in Figure 71, the following four important attributes can be observed:

1. The magnitude of voltage spikes generally scales proportionally to current increase and have similar shapes in repeats at different current levels. This indicates that current density (the amount of electrical charge per unit of time that flows through a cross-sectional area) is not a significant factor, and spikes are a property of the geomaterial. An exception is the data from 630-Hz frequency and 510 μA current in Figure 71a.
2. The direction of rolling gives significantly different and repeatable resistivity measurements. The reasons for this observation, aside from the non-uniform application of pressure, are not known.
3. The one-second stationary measurement is typically the lowest resistivity reading.
4. The measurements at 630 Hz display strong polarization with the negative red curve spikes coincident with the positive blue curve spikes.

A comparison between the two rolling velocities, in Figure 71a to Figure 71b and Figure 71c to Figure 71d, indicates that some noise characteristics change with the speed of movement. In this soil, rolling at a slower rate gave lower noise spikes. Moving slower in the coarser SM and SP specimens gave larger noise spikes, as shown in the appendix. The experiment design was only expecting mechanical noise from brush to wheel relative motion, and this result points towards fluid pressure relaxation in the vicinity of the rolling electrode being a dominant control on polarization.

Finally, comparing the results in Figures 71a and 71b**,** measured on October 16, to those with the far lower noise in Figures 71c and 71d, measured on October 17, points to the effect of remixing and recompacting the specimen. The noise levels and direction sensitivity shown in Figures 71a and 71b were first attributed to a failure of the electrode array or electronics. After repeated tests and further calibration testing, the material was removed from the tray, remixed, and recompacted. The dramatic change in CR measurements directly points to the conclusion that heterogeneity in the texture or moisture at the electrode scale will dominate the smaller, higher frequency signal related to pore-scale saturation. An analogy with the reasons for extended sample preparation protocol for the resilient modulus test point toward sample procedures that might be needed to minimize mixing/compaction heterogeneity.

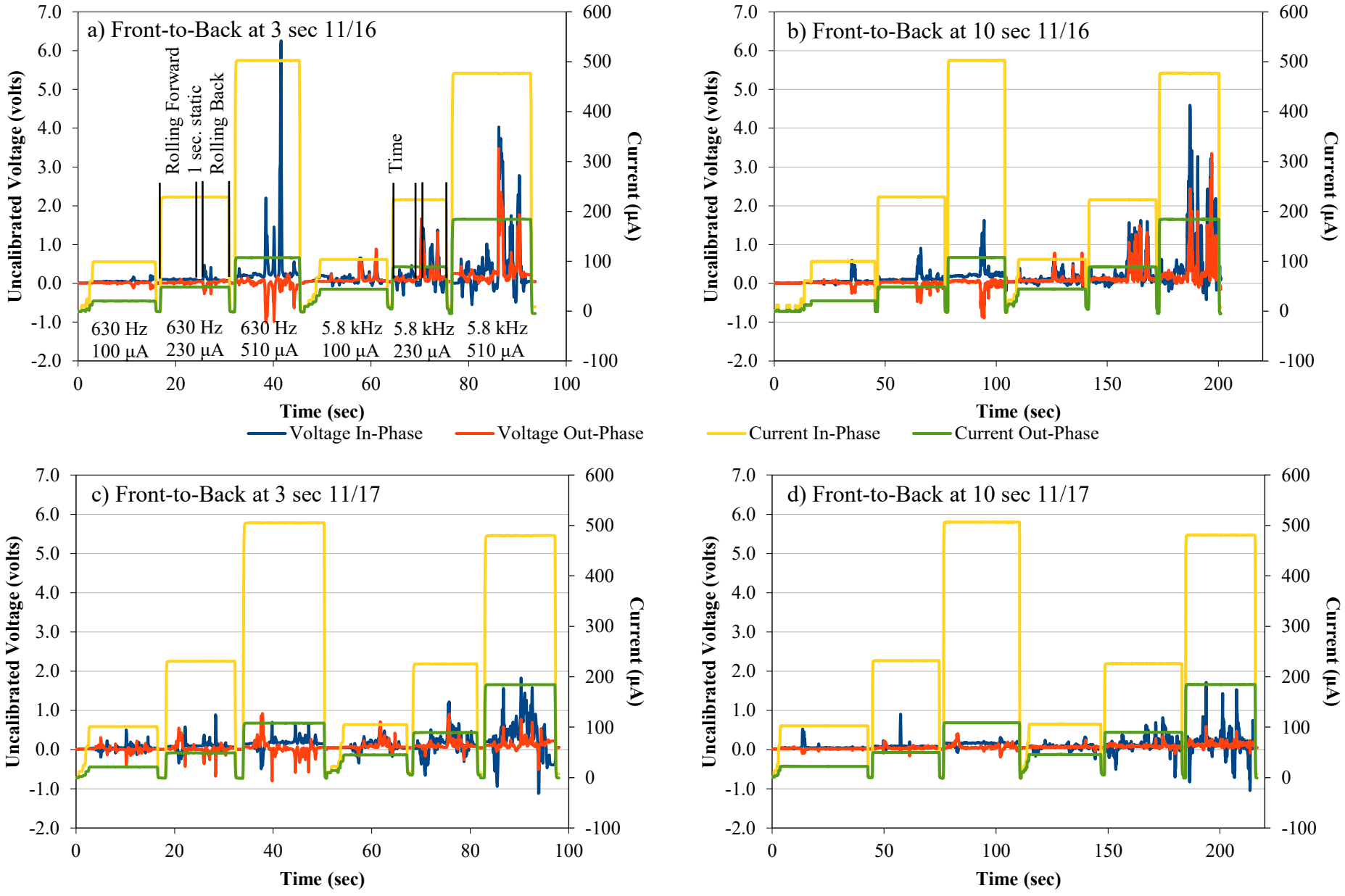


**Figure 71: CL-1 Comparison of 3 and 10-second runs compacted 11/16 (a-b) then remixed and compacted 11/17 (c-d)**

Figure 72 shows a more quantitative analysis of the performance of the current injection portion of the CR hardware. This figure demonstrates the real and imaginary components of current measurement for the specimen/speed of Figure 71b for two frequencies at the high current setting. The red lines show the expected drive current with a 0.1% variation from the expected value. Each point cloud contains over 300 measurements. The current driver and electrode contact function properly in this near-worst-case noise setting.

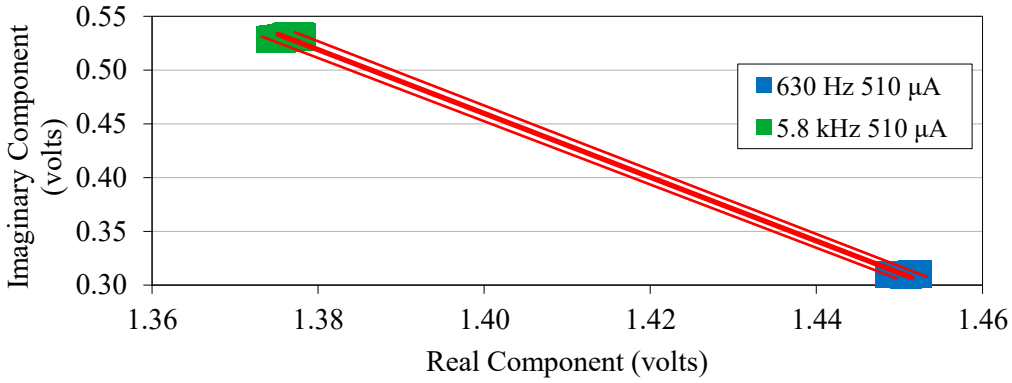


**Figure 72: Quantitative Analysis of Current Injection**

The resistivity values and phase changes from CR tests with the Wenner array at 630 Hz and 5.8 kHz at current levels of 100 µA to 230 µA to 510 µA were extracted for each soil at all three moisture contents. The standard deviations of the resistivity and phase measurements at the two frequencies are given in Table 6 for each material. These uncertainties are at or less than 5% of the measurement magnitude and indicate little sensitivity to the current density in the four materials.

**Table 7: Standard Deviation of Wenner Resistivity and Phase Change**

| Parameter | Standard Deviation | | | |
|---|---|---|---|---|
| | CL-1 | CL-2 | SM | SP |
| **Resistivity at 600 Hz (kohm –cm)** | 0.27 | 0.09 | 0.12 | 1.61 |
| **Resistivity at 5.8 kHz (kohm-cm)** | 0.22 | 0.10 | 0.11 | 0.26 |
| **Phase Change at 600 Hz (degree)** | 0.86 | 0.33 | 0.35 | 0.67 |
| **Phase Change at 5.8 kHz (degree)** | 1.64 | 1.41 | 1.45 | 1.52 |

The Wenner static CR measurements at five locations in each tray are compared to binned REA CR measurements for each of the four materials in Figures 73 and 74 and Appendix B. The Wenner measurements were normalized to the average resistivity and phase values for the five measurements in each OMC specimen. The REA measurements were first binned into five locations rolling in one direction, a 1-second bin while static, and five locations rolling in the reverse direction. These binned resistivities and phases were then normalized to the average of the four 1-second static intervals between changing the REA rolling direction in the OMC specimens

Figures 73 and 74 show the results from the SP specimen, which will be discussed extensively. Graphs and data for the SM, CL-1, and CL-2 materials are included in Appendix B. Figures 73a and 74a represent the data from the OMC-2% specimens. Similarly, Figures 73b and 74b represent the data for specimens prepared at OMC and Figures 73c and 74c correspond to the results from OMC+2% specimens. The static CR Wenner measurements normalized to OMC are shown in blue. Figure 73 shows the results at two rolling speeds for the back-to-front direction, and Figure 74 shows two repeats at two rolling speeds for the front-to-back direction. The SP geomaterials do not show a strong sensitivity to rolling direction as in the other three geomaterials (presented in the appendix). However, the general variability is rather high and repeatability is of concern between measurements repeated within 10 minutes. For instance, comparing the results between Figures 73a and 74a for the yellow curves for normalized resistivity, phase, and phase change for the 3-second traverse does not show similar variations.

In both Figures 73 and 74, the specimens prepared at OMC and wet of OMC generally yield more repeatable results that follow the expected trends predicted from the Proctor specimens. At OMC, normalized resistivities are close to 1, indicating that Wenner and REA estimates are consistent. As anticipated, the normalized resistivities for the specimen prepared at OMC+2% are lower. The more considerable contribution of the bin bottom to the REA measurement is confirmed by resistivities in Figure 74c being roughly two times higher than the Wenner value. The normalized phase at 630 Hz in the central graphs shows a substantial degree of variability at OMC. The normalized phase for the specimen prepared at OMC+2% is near zero, while the OMC sample has a moderately larger phase and is more variable. The phase change between the data collected at 630 Hz and 5.8 kHz shown in the right-hand graphs shows a consistent trend of high phase change values at OMC-2% and low phase change at OMC+2%. The SP specimens yielded a different pattern from the other three geomaterials in that the normalized Wenner resistivity at OMC-2% shows more variation than the REA measurements.

The variability is greater in the SP and SM specimens at the slower rolling speed than at the faster speed. This differs from the results for CL-1 and CL-2 specimens in that variability was higher at the faster-rolling speed.

In all the repeat measurements for all four geomaterials, the current injection and the presumed electrode contacts were similar to the ideal illustrated in Figure 44. There is no indication that electrode contact deteriorated in any measurements. The degree of variability and consistency with rolling direction in all specimens points to our failure to control, or understand, all relevant variables. Both placing the Wenner electrodes and operating the REA modified the soil, leaving divots or ruts, that might have resulted in the dissipation of transient pore pressures and compaction modification with a stronger influence on the REA measurements with larger areas impacted over shorter periods. Finally, the high degree of variability with large-scale moisture heterogeneity observed most strongly with the specimens prepared dry of OMC seems to overwhelm both the resistivity/phase signals arising from specimen size and the average pore saturation. The electrode array-scale heterogeneities overwhelmed the CR measurement of the average pore-scale saturation.

The CR measurements are likely to show measurement variations related to the geomaterial properties, the electrode array's characteristics, and the interaction of the array with the geomaterial during the electrode rolling. A brief discussion of the variables in each of these three topics is provided next.

The geomaterials have been demonstrated to show consistent CR signatures with a grain size distribution and moisture content in the laboratory measurements of the study. There was also evidence that variability increased as the specimen size increased from 4 in. x 8 in. cylinders to the large-scale specimens. As specimen size increases, higher heterogeneity is expected due to non-uniform compaction and mixing in each lift added to the container. Based on earlier experience with large-scale specimen preparation, more difficulty in achieving a uniform moisture distribution in the clay-size specimens was observed. Lateral property variation is anticipated despite our attempt to prepare a uniform specimen.

The electrode array has two primary design parameters. The array spacing controls the measurement depth, while the electrode geometry controls the area of average measurement. The REA has a larger depth and area of average measurement than the Wenner array with 50 mm spacing used on cylinders. We expected and observed that the REA would make a stronger contribution (about 50%) from the bottom of the tub than the static Wenner array (about 20%). We did not expect to compare absolute values but rather relative variations. We expected to have difficulty coupling current into the electrodes during rolling on the course/low moisture content geomaterials, with little difficulty measuring the corresponding voltage response at the same contact resistance. We chose the current levels as a primary quality control measure. We also expect the REA to measure CR values at a lower current density than the Wenner array and can use the variation in Wenner CR measurements with the current level as an additional quality control measure. It also appears probable that the REA will be more responsive to heterogeneity in saturation or compaction textures due to its larger specimen area.

The two primary variables dealt with in the early project phases were the electrode contact area and the electrode polarization. In this phase, we treated the rolling wheel surface with the same solder treatment used on the Wenner and cradle arrays to reduce polarization. We moved the graphite brush contact with the wheel from the outer surface to the curved area near the axle to minimize the accumulation of soil particles on the wheel perimeter. This meant the brush-wheel relative velocity was a fraction of that when contacting the wheel perimeter, both giving lower contact noise. When the brush is on the outside perimeter of the wheel, the brush has to cover three times the distance per revolution of the wheel than when we put the brush closer to the axle at 1/3 of the wheel radius as in the second design. Contact noise is related to the speed difference of the metal against the brush and the outside wheel perimeter picking up dirt, where the wheel/brush closer to the axle stays cleaner. The properties at two speeds were measured to test the REA measurements' consistency. Also, the impact of the wheel contact pressure on the soil was determined after observing significant differences in measured parameters with the rolling direction. The estimated pressure based on the measured force applied to the rolling array was about 3.5 psi per electrode in one direction of rolling and 2 psi in the other. This loading may be sufficient to cause local soil failure, and the consequent water migration under this differential stress plays a role in the CR measurement variations.

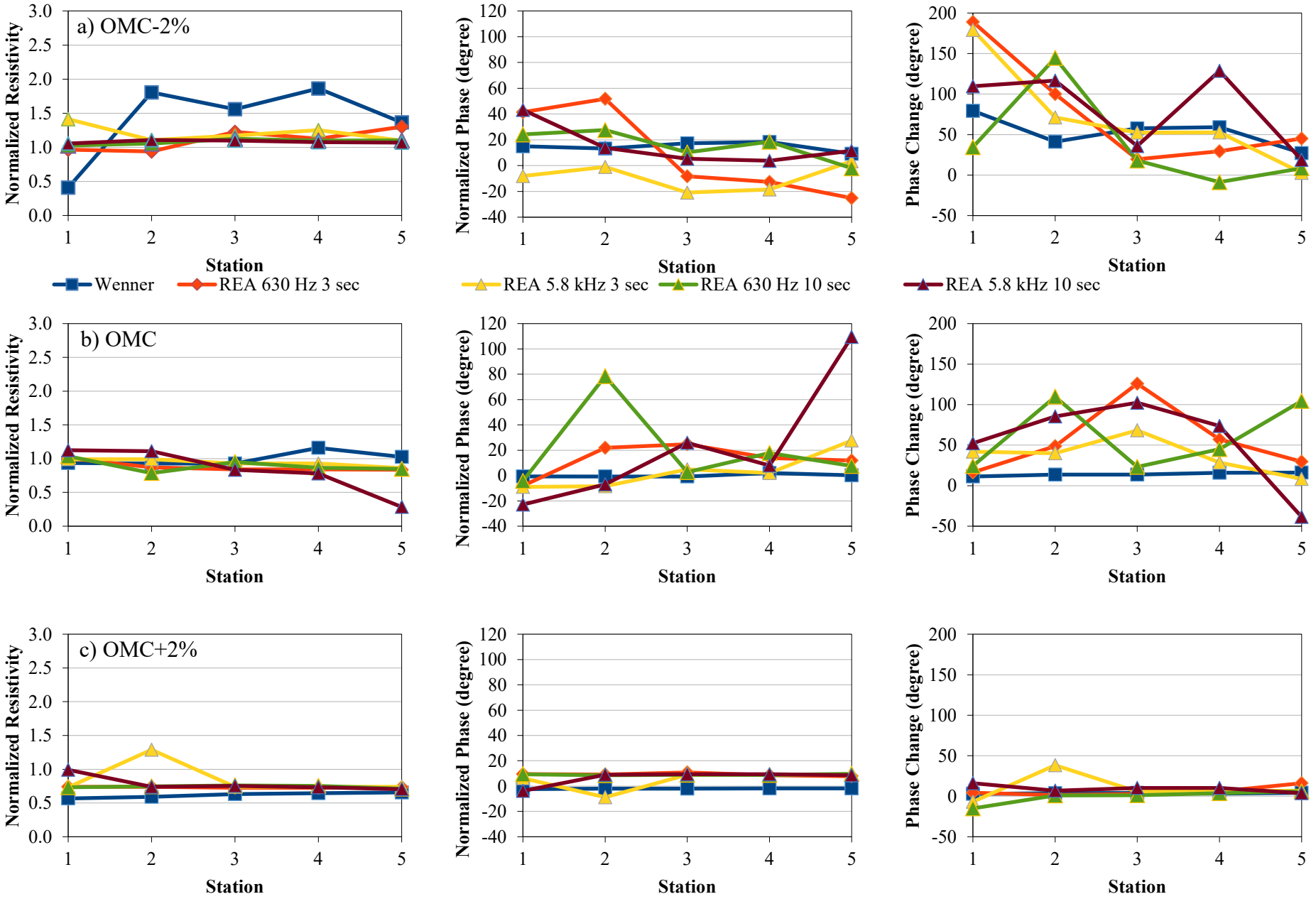


**Figure 73: Comparison of Wenner CR Measurements at 5 Stations with Repeated REA CR Measurements for the SP Specimens, Back-to-Front Direction**

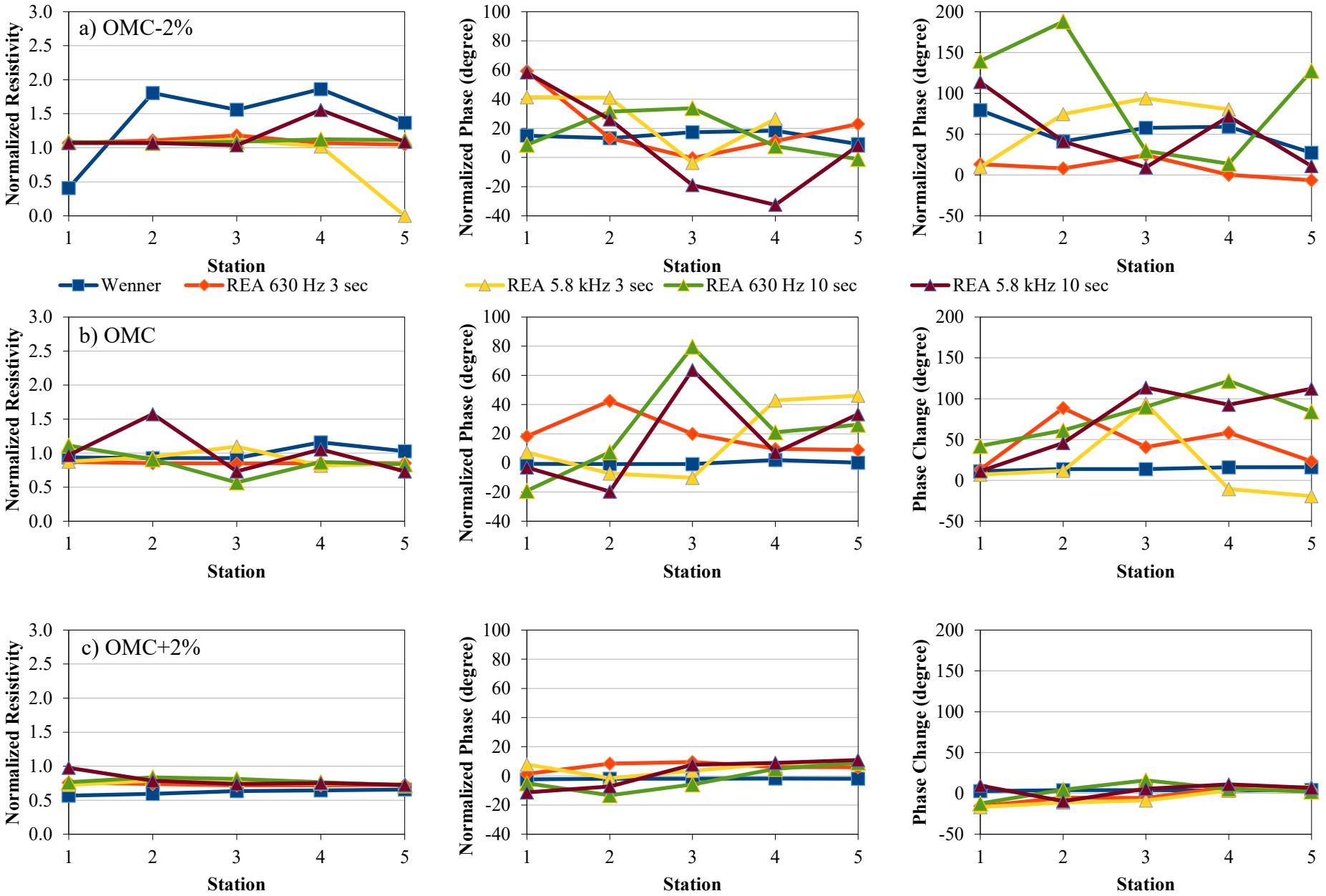


**Figure 74: Comparison of Wenner CR Measurements at 5 Stations with Repeated REA CR Measurements for the SP Specimens, Front-to-Back Direction**

# Chapter 6: Conclusions and Recommendations

In this study, six geomaterials were compacted to standard/modified proctor specifications and subjected to laboratory measurements to study the variations in their electromagnetic and electric properties with moisture content. The relationships between the seismic modulus, unconfined compressive strength, and moisture content for the same geomaterials were also established. Large-scale replicate specimens were also compacted and subjected to numerous measurements. The following lessons were learned from completing the laboratory measurements:

1. The dielectric constants measured with a Percometer were less sensitive and more uncertain about the moisture content variations than the resistivity values measured with a Wenner probe.
2. Traditional resistivity measurements were repeatable and consistent among different types of soils used in this study. Also, a good correlation was observed between the laboratory compacted specimens and corresponding measurements in a large-scale specimen of the same soil.
3. The complex resistivity showed promise in supplementing the information obtained from the traditional resistivity.
4. Aside from moisture content, grain size, and specimen heterogeneity impact the resistivity measurements more than previously expected.
5. The resistivity changes are less pronounced for the materials at moisture contents wet of OMC.
6. The seismic moduli were the most sensitive parameter to the moisture content for all materials.
7. The unconfined compressive strengths also changed significantly with the moisture contents wet of OMC and generally plateaued when the moisture contents were dry of OMC.
8. The lightweight deflectometer modulus showed a weak correlation to moisture content. Significant permanent deformation was observed for many specimens after the initial three drops.
9. The normalization scheme helps collapse the variations of the parameters with moisture content into a narrow band for easier comparison independent of the material type.

The primary conclusion from field study is that resistivity or complex-resistivity measurements with a rolling four-electrode array, with any given geometry, are probably not feasible for the control of moisture content for the following four reasons:

1. The CR polarization signal arising from the pore-scale relaxation is overwhelmed by lower-frequency polarization from moisture and compaction heterogeneity at the electrode spacing scale.
2. The apparent sensitivity of the CR measurement to electrode pressures on different soil types is difficult to predict or compensate for.
3. An incompatible tradeoff between a large electrode contact area and short array spacing is necessary to measure shallow, less dense specimens without deforming the specimen.
4. The CR measurement will become sensitive to larger heterogeneity scales with a larger electrode spacing.

## 6.1 Recommendations

Based on the lessons learned in this study, the following recommendations for future work can be made:

1. Work is required to improve the hardware and improve the technician-friendliness of software.
2. Future work could look into a calibration method that considers changes in grain size distribution.
3. As DOTs continue to use reclaimed asphalt pavements (RAP) and recycled concrete aggregate (RCA) in base and subbase mixes, the high polarizing nature of binder and calcium carbonate must be studied.
4. The grain size of the large base materials exhibited similar complex and traditional resistivity measurements to the finer-grained soils; however, due to the calcium carbonate found in the tested bases, complex resistivity polarization occurred frequently and coated the different arrays. The calcium carbonate coating created anomalies requiring frequent cleaning of the contact electrodes. The hydrophobic nature of the RAP found at the MnROAD facility caused enormous resistivities and strange polarization not expected or measured within the laboratory setting.
5. The configuration of the rolling Wenner array should be carefully optimized parallel and perpendicular to the rolling direction. With the parallel alignment, three electrodes would follow the leading electrode, and only the leading electrode would sample a new heterogeneity and show the least variability. The perpendicular alignment would have all four electrodes sampling heterogeneity independently and offer the most variability.
6. The use of noncontact electromagnetic measurements (EM) for field deployment should be seriously considered for the following reasons:
    - It is easier to couple energy and make measurements in highly resistive drier soils or engineered materials, such as used in recycled asphalt materials, non-hydrophilic materials like carbonates, and large aggregate hydrophilic materials.
    - The coil area can control the volume averaged, while the spacing between sending and receiving coils controls the depth of investigation.
    - The EM system can measure before the soil is modified from pressure from the transport/ suspension mechanism and is more independent of the velocity of motion.

# References


Baltzer, S., Pratt, D., Weligamage, J., Adamsen, J., & Hildebrand, G. (2010). Continuous bearing capacity profile of 18,000 km Australian road network in 5 months. Paper presented at the 24th ARRB Conference, Melbourne, Australia.

Bell, J.P., Dean, T.J., & Hodnett, G.C. (1987). Soil moisture measurement by an improved capacitance technique, Part II. Field techniques, evaluation, and calibration. *J. of Hydrology, 93*(1-2), 79-90

Bogena, H.R., Huisman, J.A., Oberdörster, C., & Vereecken, H. (2007). Evaluation of a low-cost soil water content sensor for wireless network applications. *Journal of Hydrology, 344*(1-2), 32-42.

Brand, A.S., Roesler, J.R., Chavan, H.L., & Evangelista F. (2013). *Effects of a nonuniform subgrade support on the responses of concrete pavement* (Report No. ICT-13-027) Champaign, IL: University of Illinois at Urbana-Champaign.

Campbell, C. (2019). *Improving the outcomes of geomaterial field monitoring campaigns*. Washington, DC: Transportation Research Board.

Chang, G.K., TaghaviGhalesari, A., Gilliland, A., Nazarian, S., Tirado, C., Rocha, S., & Zuniga, I.E. (2023). Evaluation of level 3-4 intelligent compaction measurement values (ICMV) for soils subgrade and aggregate subbase compaction. MnDOT Digital Library. Retrieved from https://mdl.mndot.gov/items/NRRA202304

Cole, S., & Buis, A. (n.d.). NASA soil moisture radar ends operations, mission science continues. SMAP. Retrieved from https://smap.jpl.nasa.gov/news/1247/nasa-soil-moisture-radarends-operations-mission-science-continues/

Emilsson, J., Englund, P., & Friborg, J., (2002). Simple method for estimation of water content of roadbeds using multi-offset GPR. *Ninth International Conference on Ground Penetrating Radar, 4758,* 422-426.

Entekhabi, D., Yueh, S., O'Neill, P.E., Kellogg, K.H., Allen, A., Bindlish, R., & Das, N. (2014). *SMAP handbook–soil moisture active passive: Mapping soil moisture and freeze/thaw from space*. Pasadena, CA: Jet Propulsion Laboratory.

Evett, S.R., Heng, L.K., Moutonnet, P., & Nguyen, M.L. (2008). *Field estimation of soil water content: A practical guide to methods, instrumentation, and sensor technology*. Vienna: IAEA.

Ferne, B.W., Langdale, P., Round, N., & Fairclough, R. (2009). Development of a calibration procedure for the UK highways agency traffic-speed deflectometer. *Transportation Research Record, 2093*(1), 111–117.

Genc, D., Ashlock, J.C., Cetin, B., & Kremer, P. (2019). Development and pilot installation of a scalable environmental sensor monitoring system for freeze-thaw monitoring under granular-surfaced roadways. *Transportation Research Record*, *2673,* 0361198119854076.

Gerhards, H., Wollschläger, U., Yu, Q., Schiwek, P., Pan, X., & Roth, K. (2008). Continuous and simultaneous measurement of reflector depth and average soil-water content with multi-channel ground-penetrating radar. *Geophysics, 73*(4), J15-J23.

Grabe, J., & Mahutka, K.-P. (2005). Long-term evenness of pavements with respect to soil deformations. Paper presented at the Seventh International Conference on the Bearing Capacity of Roads, Railways and Airfields, Trondheim, Norway.

Hansen, B.J., & Nieber, J.L. (2013). *Performance-based measurement of optimum moisture for soil compaction* (Report MN/RC 2013-28). Minneapolis, MN: University of Minnesota.

Jones, S.B., Wraith, J.M., & Or, D. (2002). Time domain reflectometry measurement principles and applications. *Hydrological Processes, 16*(1), 141-153.

Kelley, J., & Moffat, M. (2011). *Review of the Traffic Speed Deflectometer-Final Project Report* (Report AT1613). Melbourne, Australia: ARRB Group.

Kurtz, L. (2019). How to measure moisture content. Wikihow. Retrieved from https://www.wikihow.com/Measure-Soil-Moisture

Liang, R.Y., Al-Akhras, K., & Rabab'ah, S. (2006). Field monitoring of moisture variations under flexible pavement. *Transportation Research Record, 1967*(1), 160-172.

Maser, K.R., & Scullion, T. (1992). Automated pavement subsurface profiling using radar: Case studies of four experimental field sites. Transportation Research Record, 2673, pp. 148-154.

McNairn, H., Jackson, T.J., Powers, J., Bélair, S., Berg, A., Bullock, P., & Pacheco, A. (2016). Experimental plan SMAP validation experiment 2016 in Manitoba, Canada (SMAPVEX16-MB). Available online at https://nsidc.org/sites/default/files/smapvex16_experimentplan_0.pdf.

Mittelbach, H., Casini, F., Lehner, I., Teuling, A.J., & Seneviratne, S. I. (2011). Soil moisture monitoring for climate research: Evaluation of a low-cost sensor in the framework of the Swiss Soil Moisture Experiment (SwissSMEX) campaign. *Journal of Geophysical Research: Atmospheres, 116*(D5), pp. 1-11.

Muller, W. (2017). Characterizing moisture within unbound granular pavements using multi-offset Ground Penetrating Radar. PhD Dissertation, University of Queensland, Australia, 25 pages.

Robinson, D.A., Jones, S.B., Wraith, J.M., Or, D., & Friedman, S.P. (2003). A review of advances in dielectric and electrical conductivity measurement in soils using time domain reflectometry. *Vadose Zone J., 2*, 444–475

Saïd, M.N.A. (2007). Measurement methods of moisture in building envelopes–a literature review. *International Journal of Architectural Heritage, 1*(3), 293-310.

Sebesta, S., Taylor, R., & Lee, S.I. (2013). *Rapid field detection of moisture content for base and subgrade* (No. 0-6676). College Station, TX: Texas. Dept. of Transportation, Research and Technology Implementation Office.

Shaikh, J., Yamsani, S.K., Sekharan, S., & Rakesh, R.R. (2018). Performance evaluation of profile probe for continuous monitoring of volumetric water content in multilayered cover system. *Journal of Environmental Engineering, 144*(9), 04018078.

Singh, J. (2017). Performance assessment of electromagnetic soil water sensors in different soil textural, temperature, and salinity conditions. M.S. thesis, University of Nebraska-Lincoln, Nebraska, 104 pages.

Sotelo, M.J. (2012). Evaluation of non-nuclear devices in measuring moisture content and density of soils. M.S. thesis, The University of Texas at El Paso, Texas, 87 pages

Svensson, J. (1997). *Moisture content in road pavements: state of the art and development of a simple moisture measurement equipment*. Stockholm, Sweden: Swedish National Road and Transport Research Institute, VTI.

Topp, G.C., Davis, J., & Annan, A.P. (1980). Electromagnetic determination of soil water content: Measurements in coaxial transmission lines. *Water Resources Research, 16*(3), 574-582

University of Sherbrooke. (2012). SMAP Validation Experiment (SMAPVEX12). Sherbrooke, Canada: University of Sherbrooke.

UTEST. (2016). *RoadReader nuclear density gauges.* Retrieved from https://www.utest.com.tr/en/23174/RoadReader-Nuclear-Density-Gauges

Viyanant, C., Rathje, E. M., & Rauch, A. F. (2004). Compaction control of crushed concrete and recycled asphalt pavement using nuclear gauge. *Geotechnical Special Publication 126* (pp. 958-966). Reston, VA: ASCE.

White, D.J., Li, S., & Vennapusa, P. (2016). Embankment quality and assessment of moisture control implementation (Report IHRB Project TR-677). Ames, IA: Center for Earthworks Engineering Research, Iowa State University.

White, D.J. (2019). *Optimizing placement cost using material specific compaction energy and moisture content.* Washington, DC: Transportation Research Board presentation.

White, D.J., Vennapusa P., & Cetin B. (2021). *Improving the foundation layers for concrete pavements: Lessons learned and a framework for mechanistic assessment of pavement foundations* (Report 09-352) Ames, IA: Iowa State University.

Wollschläger, U., Gerhards, H., Yu, Q., & Roth, K. (2010). Multi-channel ground-penetrating radar to explore spatial variations in thaw depth and moisture content in active layer of a permafrost site. *The Cryosphere, 4*(3), 269.

Yu, X., & Yu, X. (2009). Time domain reflectometry automatic bridge scour measurement system: principles and potentials. *Structural Health Monitoring, 8*(6), 463-476.

Yueh, S., O'Neill, P.E., Butler, R., Osornia, L.M., Hu, W., Hanna, M., … & Mizukami, M. (n.d.) Mission description SMAP. Retrieved from https://smap.jpl.nasa.gov/news/1247/ nasa-soil-moisture-radar-ends-operations-mission-science-continues/(visited on 09/08/2017)

# APPENDIX A
# Comprehensive Datasets of Laboratory Measurements

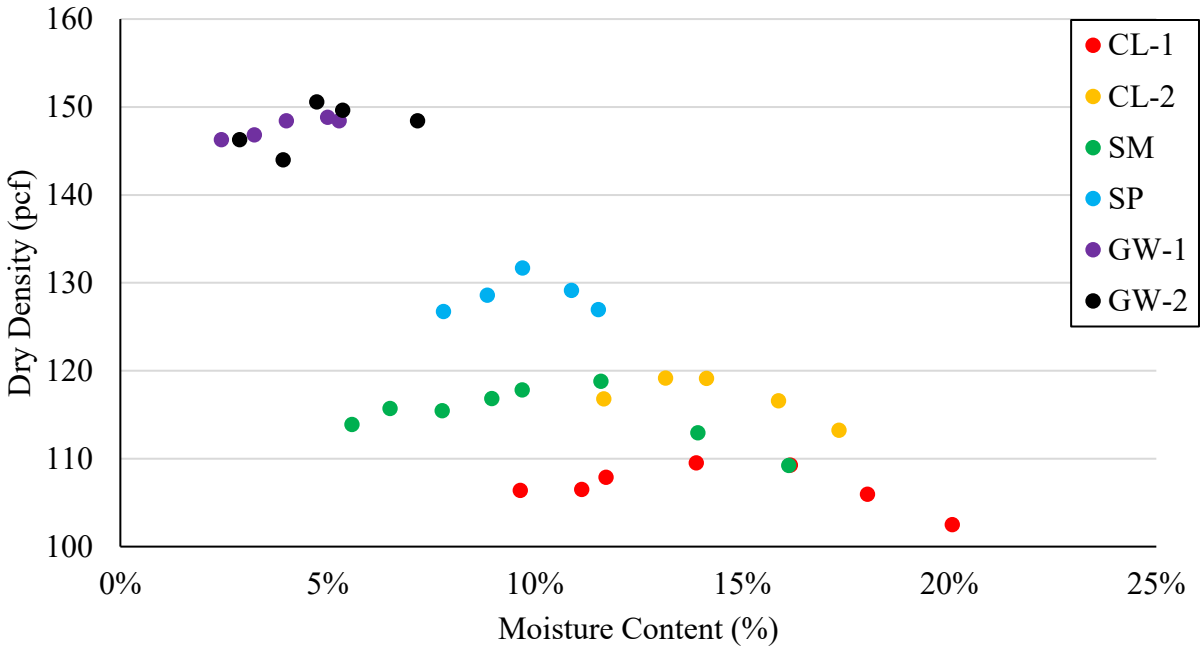


**Figure A- 1: MD Curves of 4 in. Specimens and 6 in. Gravel Specimens**

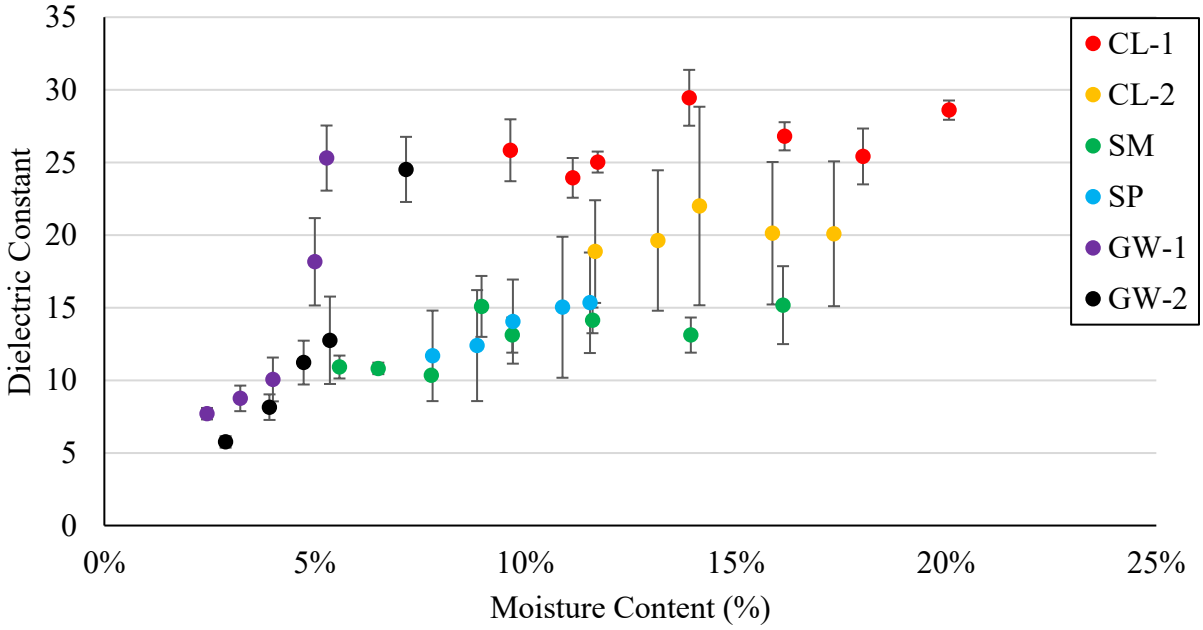


**Figure A- 2: Dielectric Constant of 4 in. Specimens and 6 in. Gravel Specimens**

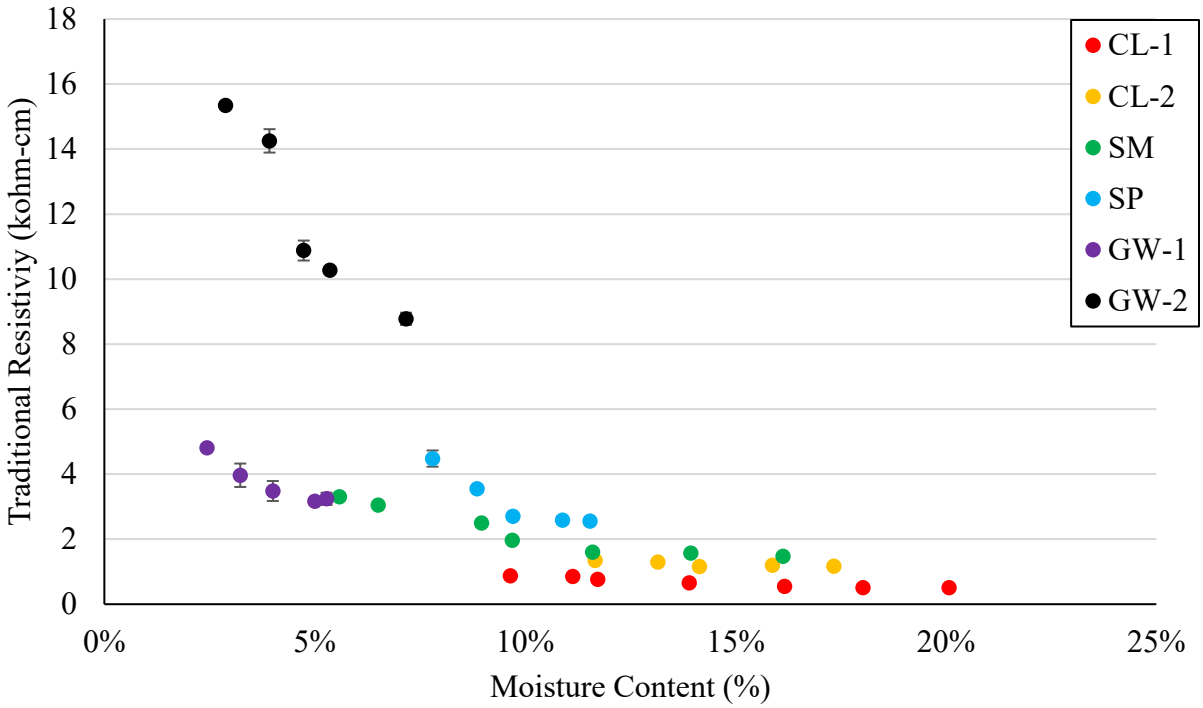


**Figure A- 3: Traditional Resistivity of 4 in. Specimens and 6 in. Gravel Specimens**

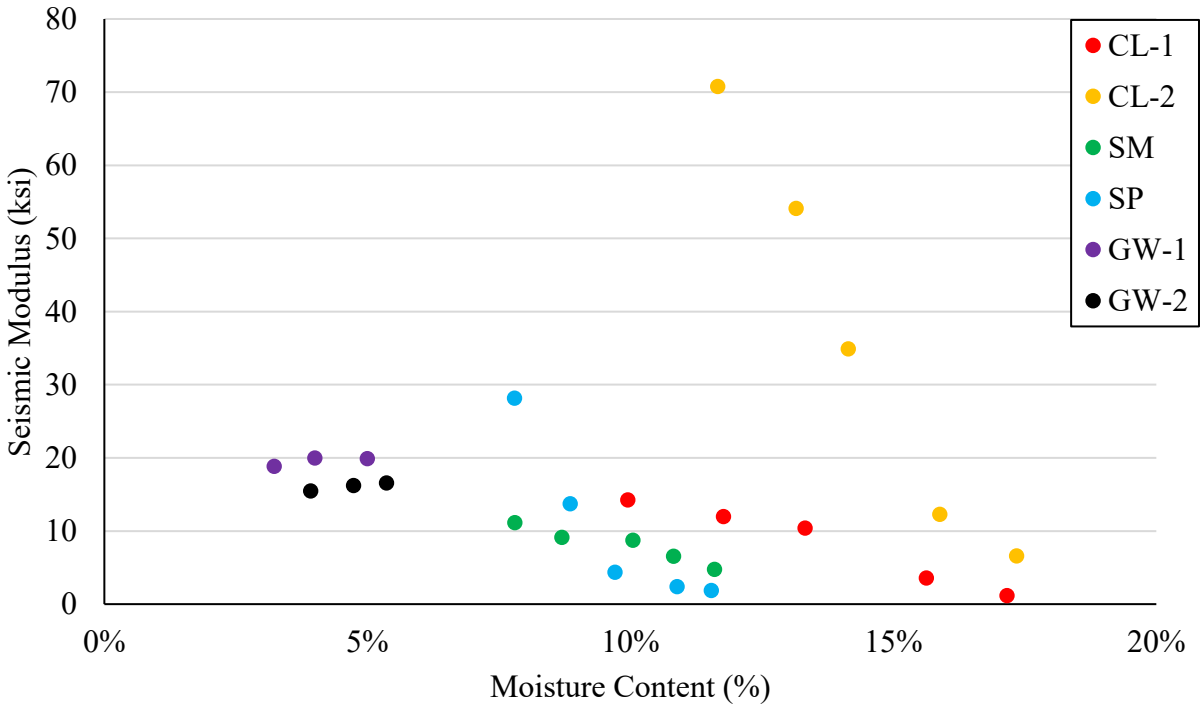


**Figure A- 4: Seismic Modulus of 4 in. Specimens and 6 in. Gravel Specimens**

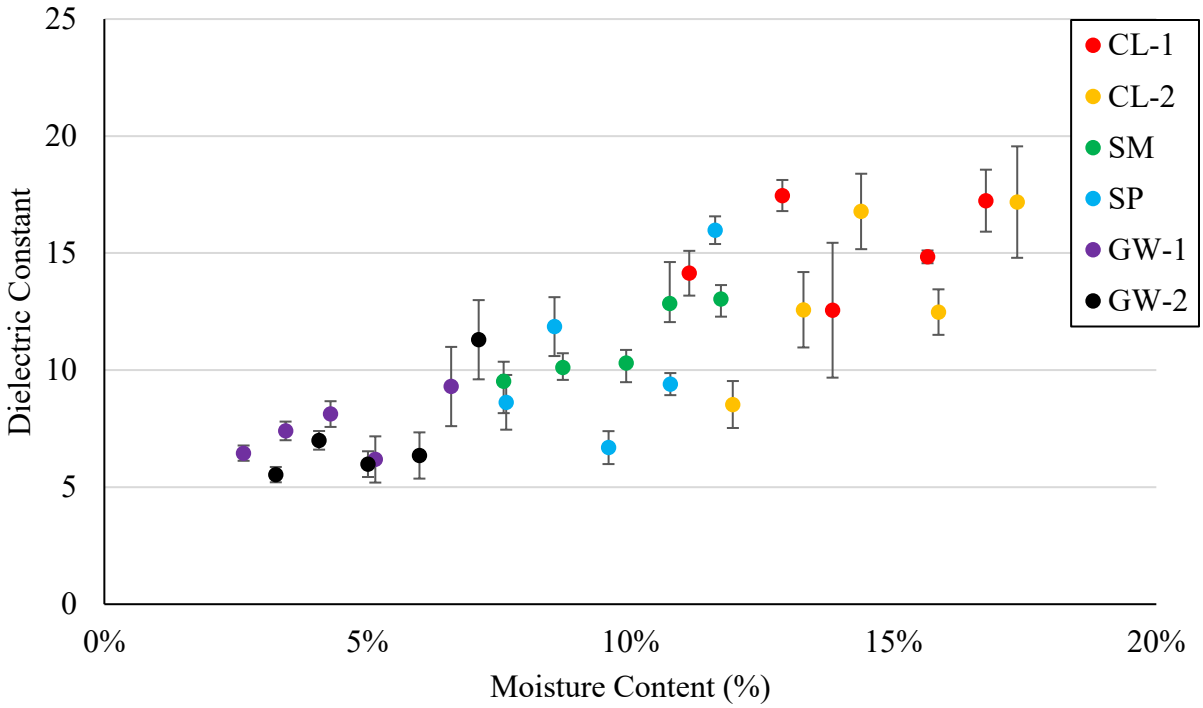


**Figure A- 5: Dielectric Constant Measurement in Large Scale Specimen at 12 in. Height**

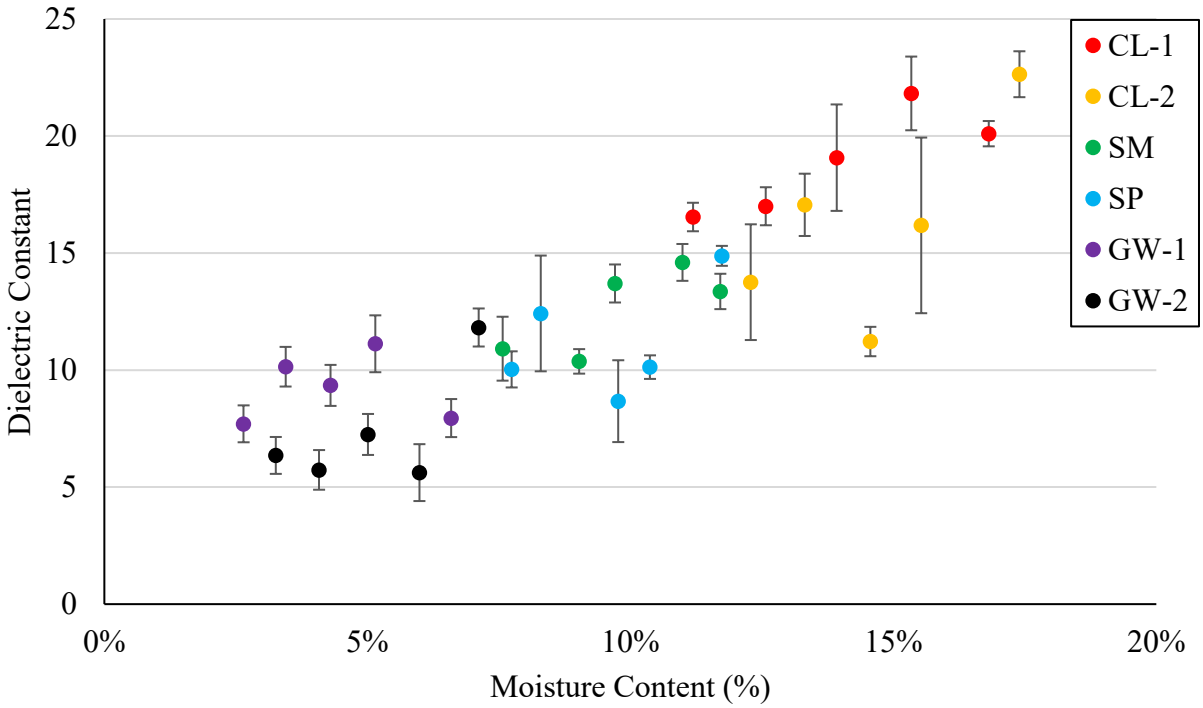


**Figure A- 6: Dielectric Constant Measurement in Large Scale Specimen at 24 in. Height**

**Table A- 1: Coefficients of Variation of Measurements of Lab Specimens**

| Measurement | Soil | Dry | | OMC | | Wet | |
|---|---|---|---|---|---|---|---|
| | | Average | Max | Average | Max | Average | Max |
| Seismic Modulus | CL-1 | 5.4 | 8.5 | 3.5 | 4.0 | 3.9 | 9.1 |
| | SM | 4.0 | 7.6 | 2.8 | 4.7 | 8.1 | 12.9 |
| | GW-1 | Not Tested | | 13.8 | 19.9 | Not Tested | |
| Unconfined Compressive Strength | CL-1 | 7.5 | N/A* | 8.5 | N/A* | 8.1 | N/A* |
| | SM | 25.6 | | 24.9 | | 7.9 | |
| | GW-1 | Not Tested | | 21.0 | | Not Tested | |
| Lightweight Deflectometer | CL-1 | 1.6 | 3.3 | 0.4 | 0.7 | 2.2 | 6.0 |
| | SM | 1.1 | 1.7 | 3.0 | 5.5 | 3.8 | 7.3 |
| | GW-1 | 3.0 | 5.6 | 1.4 | 2.3 | 1.9 | 4.3 |

*** Not applicable since only one test can be done per specimen**

**Table A- 2: Coefficients of Variation for Measurements on Large Scale Specimens at 12 in. Height**

| Measurement | Soil | Dry | | OMC | | Wet | |
|---|---|---|---|---|---|---|---|
| | | Average | Max | Average | Max | Average | Max |
| Lightweight Deflectometer | CL-1 | 6.9 | 14.0 | 6.4 | 14.3 | 4.2 | 6.3 |
| | SM | 9.7 | 10.3 | 9.9 | 16.3 | 10.5 | 16.9 |
| | GW-1 | 7.1 | 12.7 | 5.5 | 13.9 | 7.8 | 10.0 |
| Dielectric Constant | CL-1 | 7.1 | 10.5 | 7.4 | 10.1 | 18.0 | 26.4 |
| | SM | 5.0 | 7.0 | 7.2 | 7.9 | 6.5 | 12.7 |
| | GW-1 | 17.4 | 29.8 | 20.8 | 31.8 | 24.7 | 41.1 |
| Traditional Resistivity | CL-1 | 3.5 | 4.5 | 5.3 | 7.4 | 6.6 | 10.2 |
| | SM | 1.0 | 2.1 | 2.3 | 4.3 | 3.1 | 4.0 |
| | GW-1 | 4.8 | 5.7 | 6.7 | 10.0 | 7.2 | 9.1 |

**Table A- 3: Coefficients of Variation for Measurements on Large Scale Specimens at 24 in. Height**

| Measurement | Soil | Dry | | OMC | | Wet | |
|---|---|---|---|---|---|---|---|
| | | Average | Max | Average | Max | Average | Max |
| Lightweight Deflectometer | CL-1 | 8.6 | 18.8 | 5.1 | 9.2 | 3.4 | 5.5 |
| | SM | 7.3 | 15.9 | 13.7 | 18.6 | 8.2 | 15.0 |
| | GW-1 | 4.4 | 8.3 | 6.8 | 14.0 | 7.4 | 14.6 |
| Dielectric Constant | CL-1 | 4.6 | 8.9 | 11.1 | 14.1 | 4.9 | 10.0 |
| | SM | 7.5 | 7.6 | 6.3 | 8.5 | 4.7 | 6.7 |
| | GW-1 | 7.0 | 10.1 | 17.1 | 19.6 | 29.8 | 43.9 |
| Traditional Resistivity | CL-1 | 3.3 | 3.6 | 3.2 | 6.3 | 5.6 | 8.0 |
| | SM | 0.9 | 1.8 | 1.8 | 3.9 | 2.3 | 2.8 |
| | GW-1 | 4.1 | 5.5 | 4.9 | 7.1 | 8.5 | 10.2 |

# APPENDIX B
# Comprehensive Datasets of Field Evaluation

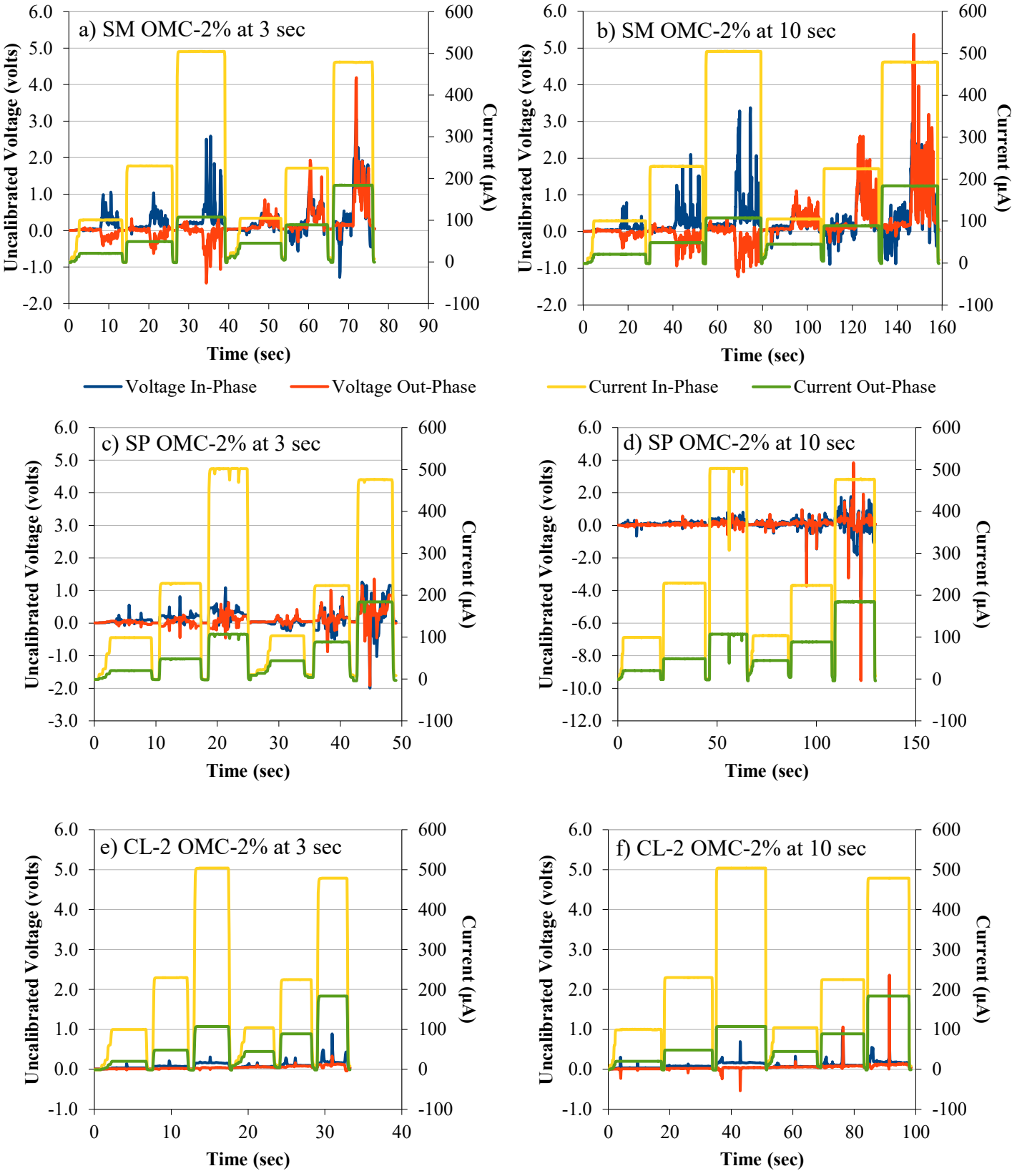


**Figure B-1: Speed Difference between the Dry Specimens at 3 seconds (a,c,e) to 10 sec (b,d,f)**

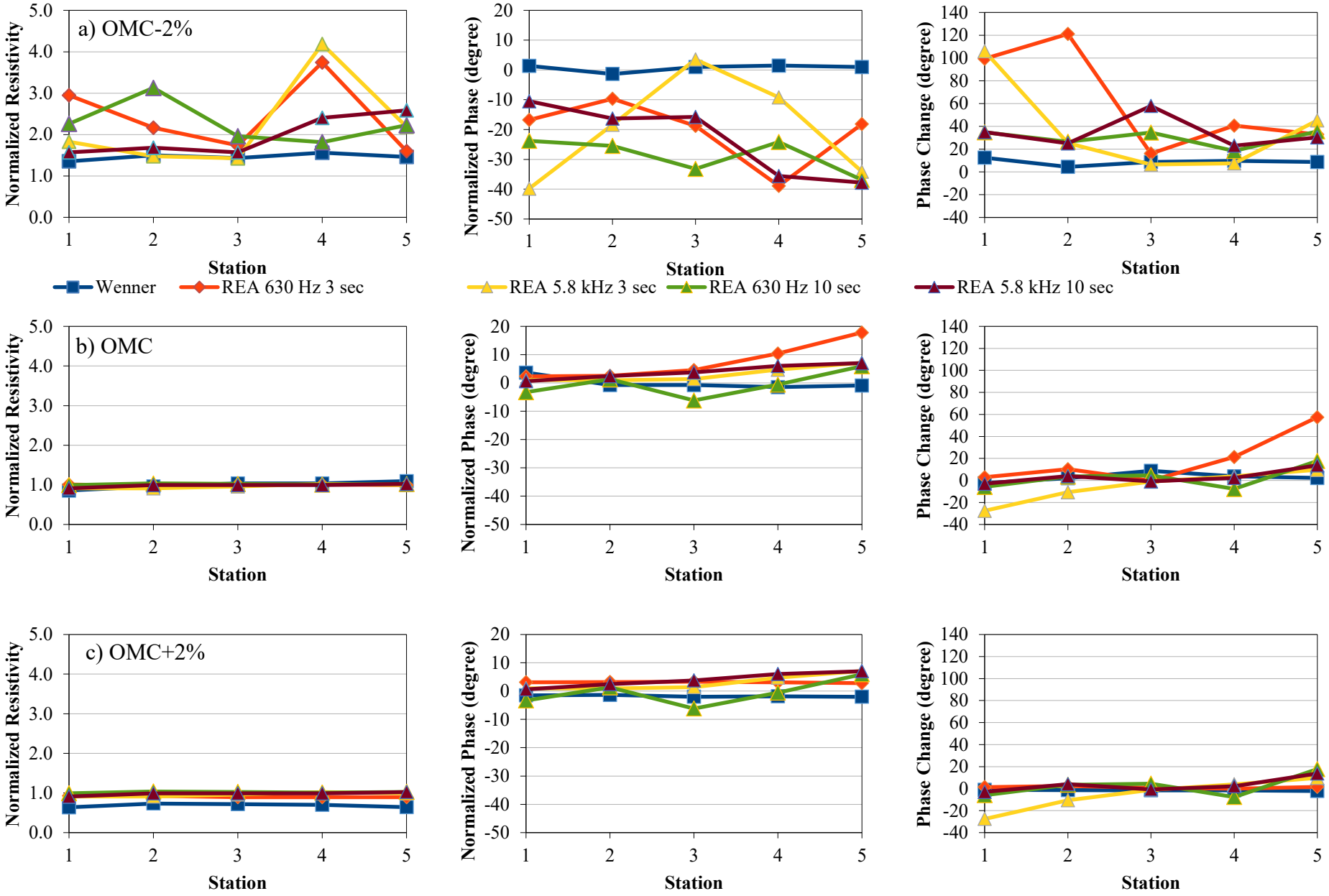


**Figure B-2: Comparison of Wenner CR Measurements at 5 Stations with Repeated REA CR Measurements for the CL-1 Specimens, Back-to-Front Direction**

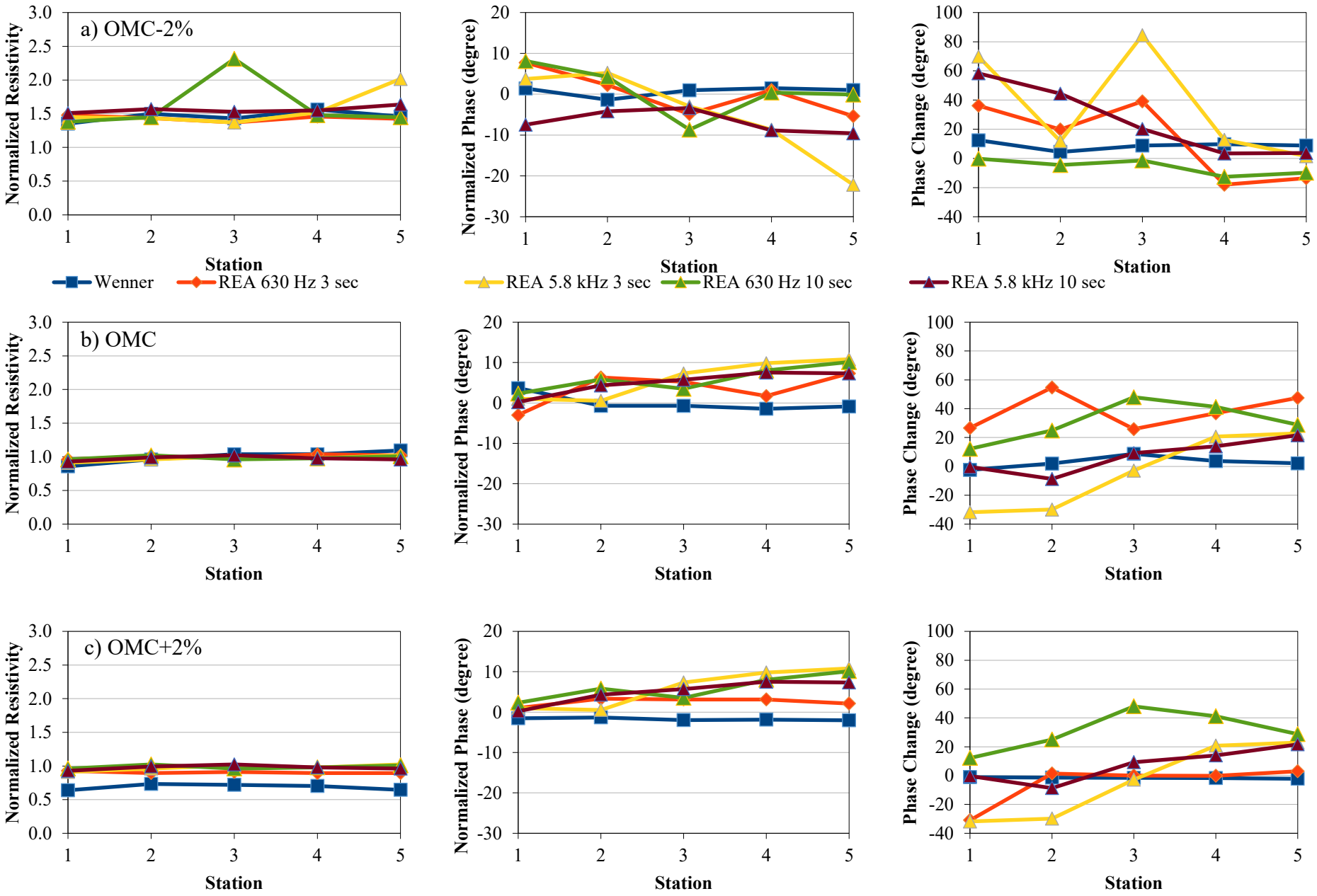


**Figure B-3: Comparison of Wenner CR Measurements at 5 Stations with Repeated REA CR Measurements for the CL-1 Specimens, Front-to-Back Direction**

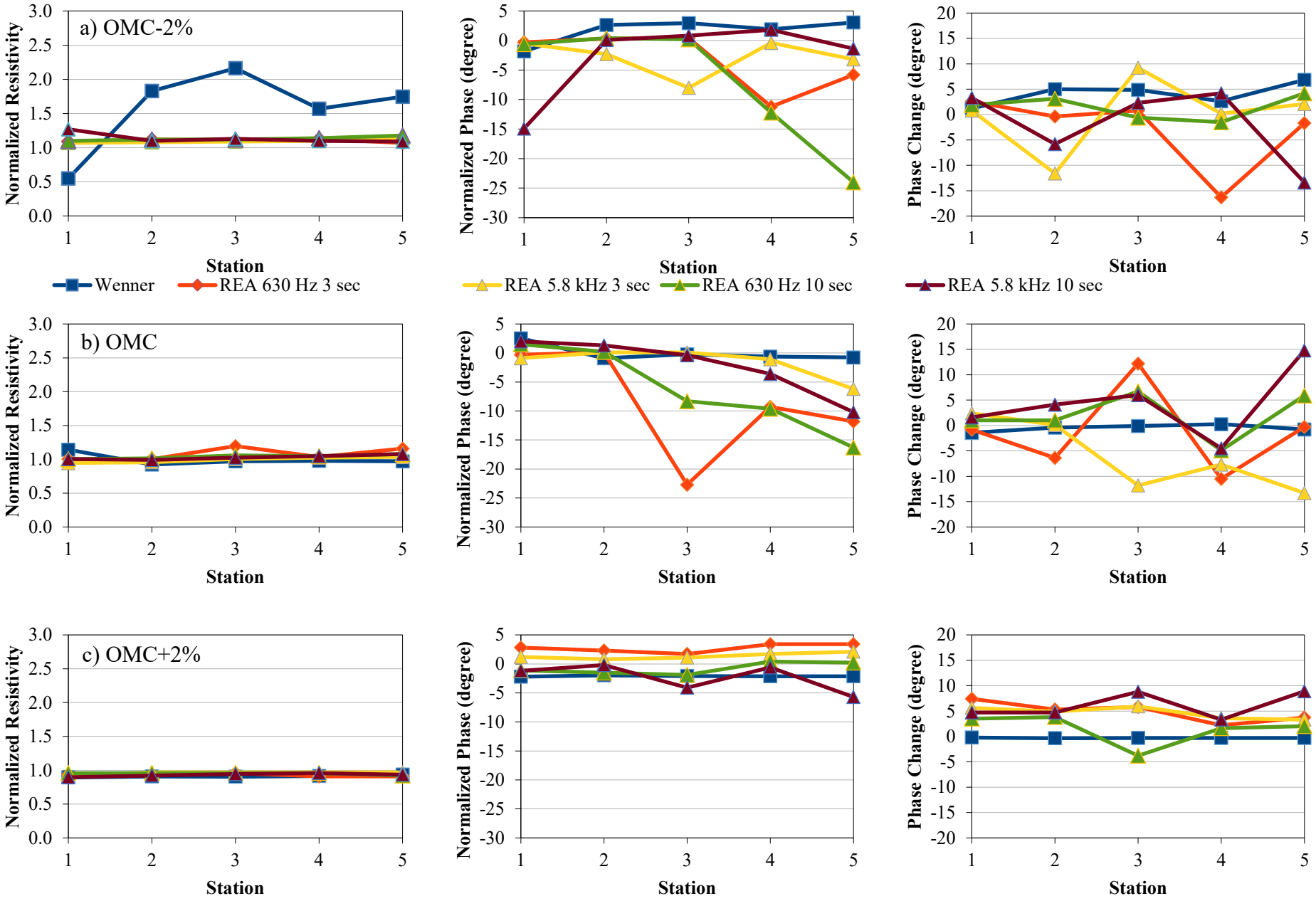


**Figure B-4: Comparison of Wenner CR Measurements at 5 Stations with Repeated REA CR Measurements for the CL-2 Specimens, Back-to-Front Direction**

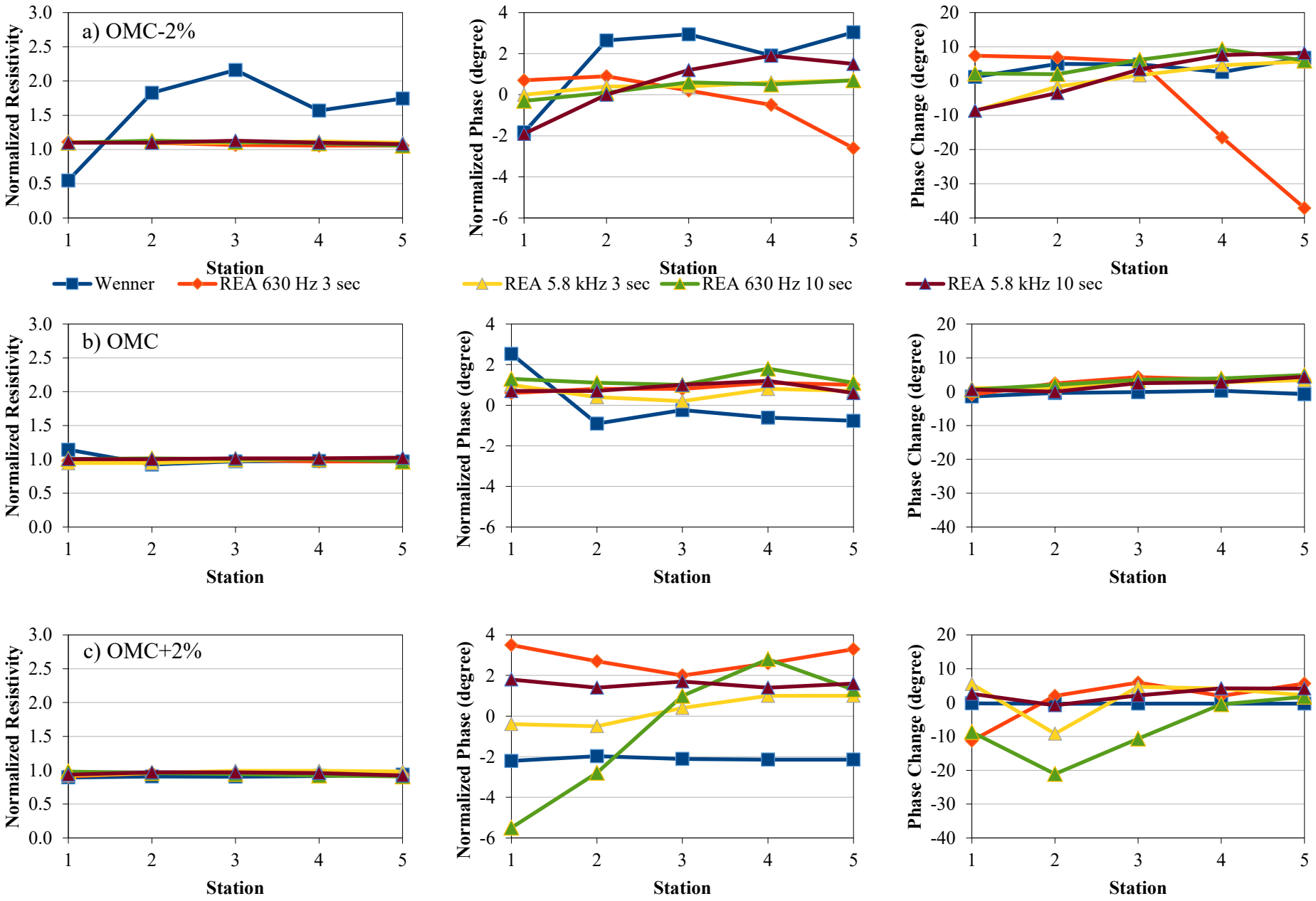


**Figure B-5: Comparison of Wenner CR Measurements at 5 Stations with Repeated REA CR Measurements for the CL-2 Specimens, Front-to-Back Direction**

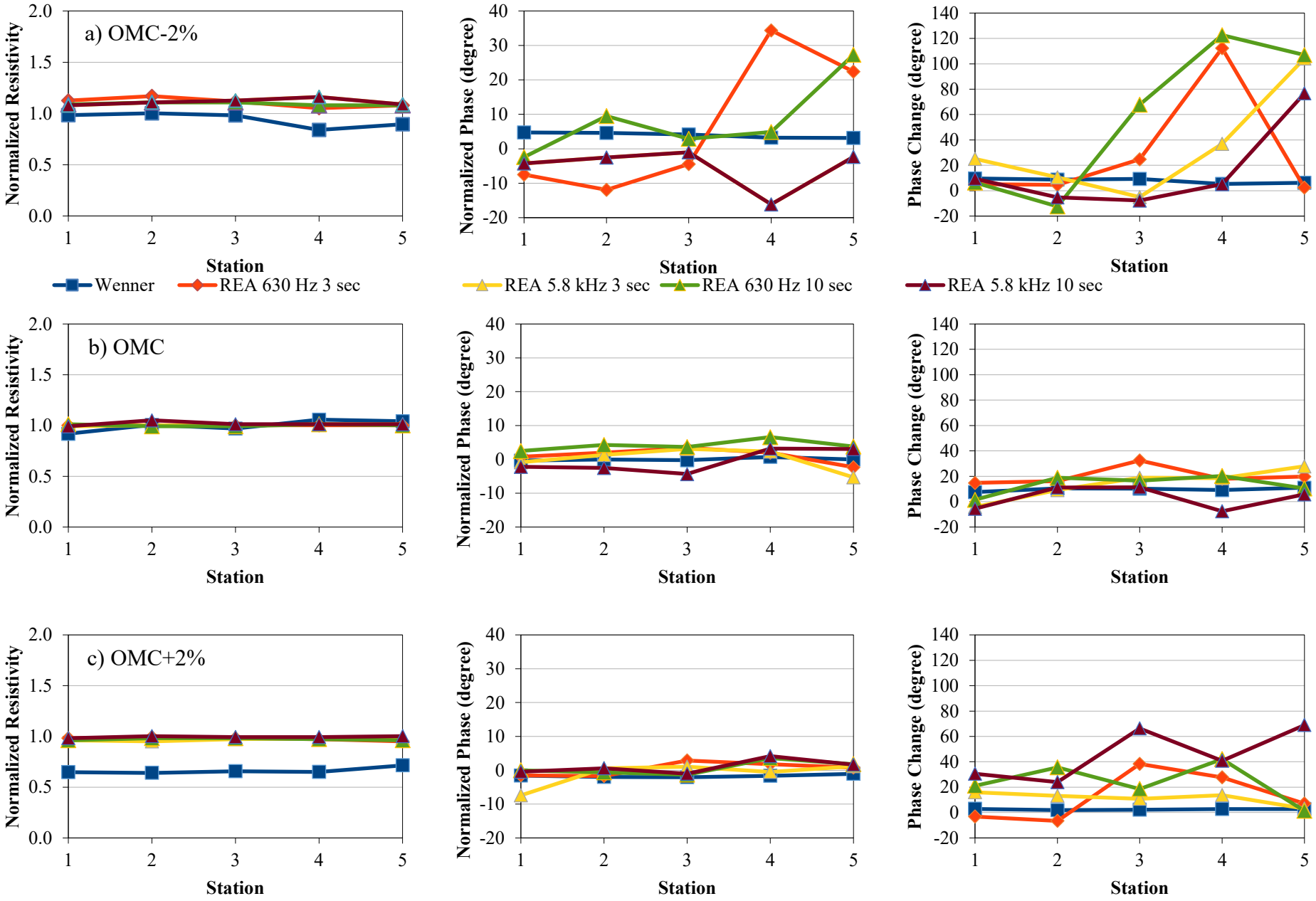


**Figure B-6: Comparison of Wenner CR Measurements at 5 Stations with Repeated REA CR Measurements for the SM Specimens, Back-to-Front Direction**

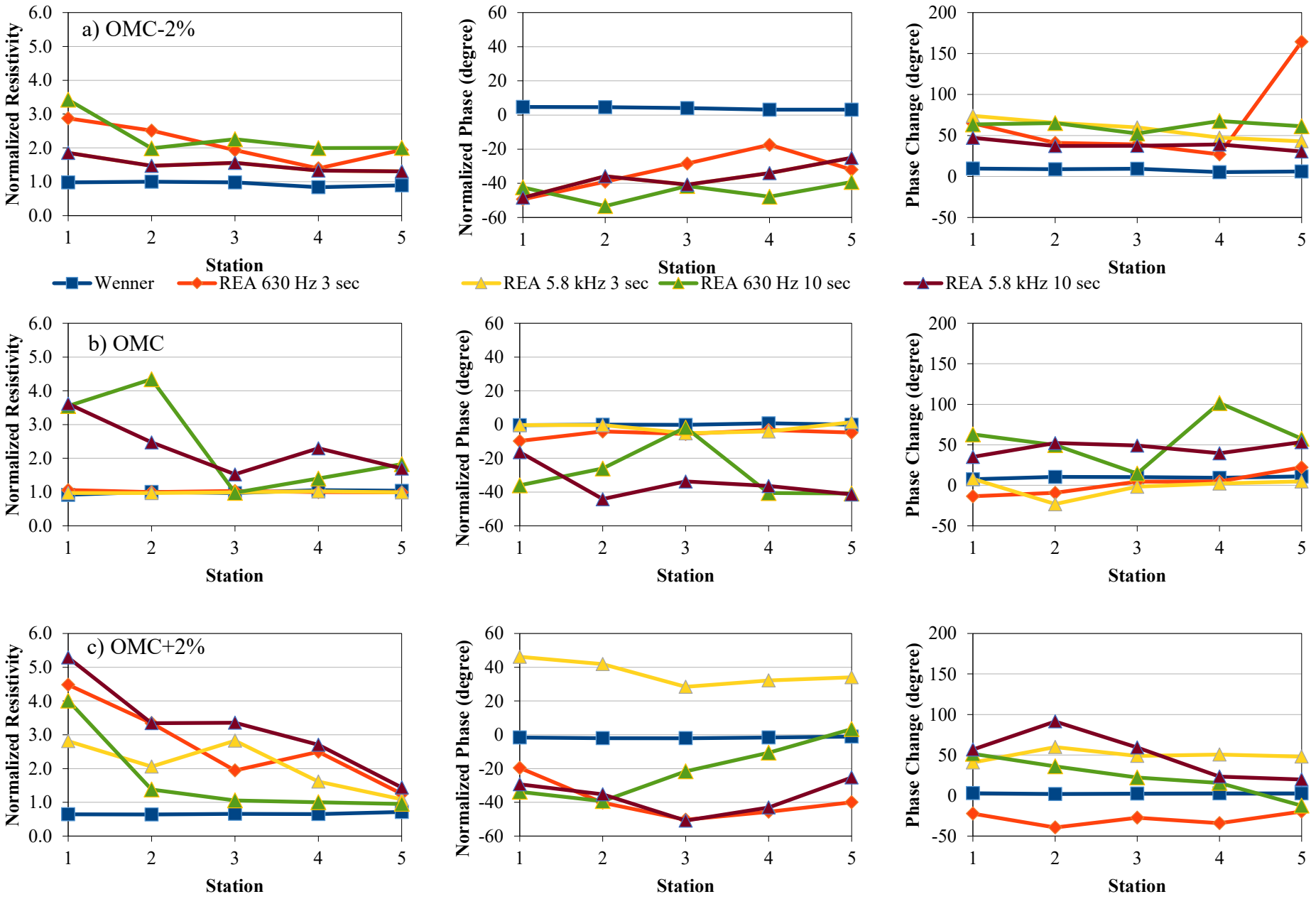


**Figure B-7: Comparison of Wenner CR Measurements at 5 Stations with Repeated REA CR Measurements for the SM Specimens, Front-to-Back Direction**